Fully-Plastic Back-Bend Tests for Low-Triaxiality Plane Strain Crack Growth

by

Fatima Haq

Bachelor of Science in Mechanical Engineering,
Northeastern University, Boston, MA (1999)

Submitted to the Department of Mechanical Engineering
in partial fulfillment of the requirements for the degree of

Master of Science in Mechanical Engineering

at the

MASSACHUSETTS INSTITUTE OF TECHNOLOGY

February 2002

Author .....
Department of Mechanical Engineering
January 18, 2002

Certified by .....
David M. Parks
Professor of Mechanical Engineering
Thesis Supervisor

Accepted by .....
Ain A. Sonin
Chairman, Department Committee on Graduate Students

Fully-Plastic Back-Bend Tests for Low-Triaxiality Plane Strain Crack Growth

by

Fatima Haq

Submitted to the Department of Mechanical Engineering
on January 18, 2002, in partial fulfillment of the
requirements for the degree of
Master of Science in Mechanical Engineering

Abstract

Fully-plastic plane strain crack growth can occur under low stress triaxiality (e.g., through-thickness penetration of a long surface-crack along a pressure vessel wall). A novel back-bend specimen gives a low-triaxiality, plane strain test, while requiring a fraction of the load of direct tension. A572 Gr.50 structural steel was tested under both back-bending and open-bending (low and high-triaxiality, respectively), and analyzed using finite elements and slip line fracture mechanics. The back-bend $CTOD$ at crack initiation was twice that of open-bending with identical geometry. The back-bend $CTOA$ was initially $\sim 30°$, twice that of open-bending.

Thesis Supervisor: David M. Parks
Title: Professor of Mechanical Engineering

Acknowledgments

I want to express my sincere gratitude to my advisor, Prof. Parks, for his constant support, guidance and encouragement. I have learnt a lot while working with him and have enjoyed interacting with him. Next, I would like to thank Prof. McClintock for his insightful guidance into the field of fracture mechanics and technical report writing. I am happy to have had the opportunity to work with him.

A special thanks to Ray Hardin for handling all the administrative matters, and Pierce Hayward for his help in the lab. Thanks to my fellow graduate students, Kevin, Vaibhaw, Tom, Steve, Matt, Dora, Hang Xi, Cheng Su, Jin Yi, Mike, Jeremy, Yin, Nuo, Rajdeep, Yu Qiao, Mats, Sauri, Brian, Prakash, Nikki and others.

Finally, I am thankful to God for giving me the opportunity to attend MIT. To my parents for their belief in me and a lifetime of support and motivation; and to my sister for her unending patience and encouragement.

Support for this research was provided by the D.O.E. under grant number DE-FG02-85ER13331 to MIT.

Contents

List of Figures

List of Tables

Chapter 1

Introduction

1.1 Motivation and Applications

Fully-plastic plane strain cracking in low-triaxiality tension occurs in many engineering structures, such as pressure vessels with long part-through cracks, which should be ductile in accidents. Low stress triaxiality, defined here as the ratio of the normal stress across the dominant active crack-tip slip lines to the plane strain flow strength, increases the ductility and toughness by decreasing rates of void nucleation, growth, and linkage. A good test is needed to quantify low-triaxiality cracking to supplement typical high-triaxiality bending tests.

Many low-triaxiality tests use a "brute force" method by simply pulling on each end of the specimen. Tests performed in this manner require large loads to reach full plasticity, and stability of post-peak deformation and cracking requires a high-stiffness testing system. One way to lower the loads required to achieve fully-plastic tension on a specimen's uncracked ligament is by the use of a bend loading, utilizing long moment arms that are inherent to the specimens. (This may require a longer specimen than that required in a direct tension test, but extensions could be welded on, if necessary.) The length adopted depends on the mechanical advantage required to lower the system load to an acceptable level. Bending has been used in traditional 3-point and 4-point open-bend tests. However, open-bending generates high crack-tip triaxiality, especially with deep cracks ($c/t \geq 0.35$, where c is crack depth and

t is specimen thickness) [1] and [2]. There is a need for a low-triaxiality, low-load specimen to reproduce some of the loading environments that exist in engineering structures.

A "back-bend" specimen meeting these requirements was suggested by McClintock. This specimen, shown in Figure 1-1(a), has been tested, analyzed, and compared to the more familiar open-bend test, shown in Figure 1-1(b). The back-bend specimen provides a useful method for studying the fracture behavior under a low-triaxiality tensile loading. Long part-through cracks or penetrating cracks in a plate of material loaded in tension create a low-triaxiality, plane strain environment. These penetrating cracks can be seen in such structures as pressure vessels, ships, and most anywhere else where substantially long/wide plates are employed. A cross-section of a pressure vessel with a penetrating crack is shown schematically in Figure 1-2. The back-bend test is also useful in studying the conditions that arise in materials under impact or collision environments. Examples of these include ship collisions, structures subject to earthquakes, etc.

1.2 Organization of Present Work

The new low-triaxiality back-bend specimen was tested by Bass [3] and has been analyzed and compared to the high-triaxiality open-bend test. Experimental results, numerical and slip line analyses, and conclusions from these studies are presented in the current work.

Chapter Two describes the mechanics and the general test setup of the back-bend and open-bend test specimens, which includes a demonstration of the mechanical advantage of using the back-bend loading versus a traditional tension test loading. To characterize the behavior of these specimens, a few fracture mechanics methods and parameters are discussed. This includes a discussion of "Slip Line Fracture Mechanics" and its stress fields ahead of the crack tips in back-bending and open-bending.

Chapter Three details the experimental and numerical procedures. This chapter includes geometrical and material specifications of the bend specimens used by Bass.

The numerical procedures discuss the finite element model, including the mesh, material model and boundary conditions. This chapter also includes a discussion of the Gurson-Tvergaard-Needleman model used to simulate crack growth.

Chapter Four discusses the results of the slow-bend testing of the back-bend and open-bend specimens. Load-displacement, sectioning, fractographic, and topographic data were analyzed using slip line fracture mechanics. Values for the crack-tip opening displacement at initiation, $CTOD_i$, and the crack-tip opening angle, $CTOA$, were calculated from the load-displacement curves. The sectioning and fractographic data were used to plot the opening displacement at the initial crack-tip, CT_0OD, versus the change in crack length, Δc. The 3-D topographical maps were averaged to calculate values of the $CTOD_i$ and $CTOA$. The major differences between back-bend and open-bend loadings are discussed.

Chapter Five discusses the results of the 2-D plane strain and 3-D finite element simulations of the back-bend and open-bend tests. The simulation load-displacement curves were compared to the experiments. Values of $CTOD_i$ and $CTOA$ were compared to those obtained from slip line analysis. The stress and strain states of the loadings were examined using contour plots. The fracture surface profiles were compared with experiments.

Chapter Six discusses further issues investigated using the finite element method. This includes a study of contained yielding using stationary cracks and the evaluation of the J-Integral. This chapter also discusses scale-effects by studying a specimen four times as large as the one already considered. A discussion of non-hardening simulations follows.

Chapter Seven summarizes the differences between the back-bend and open-bend loadings due to the difference in triaxiality between the two bend specimens. This chapter also gives suggestions for further work in this area.

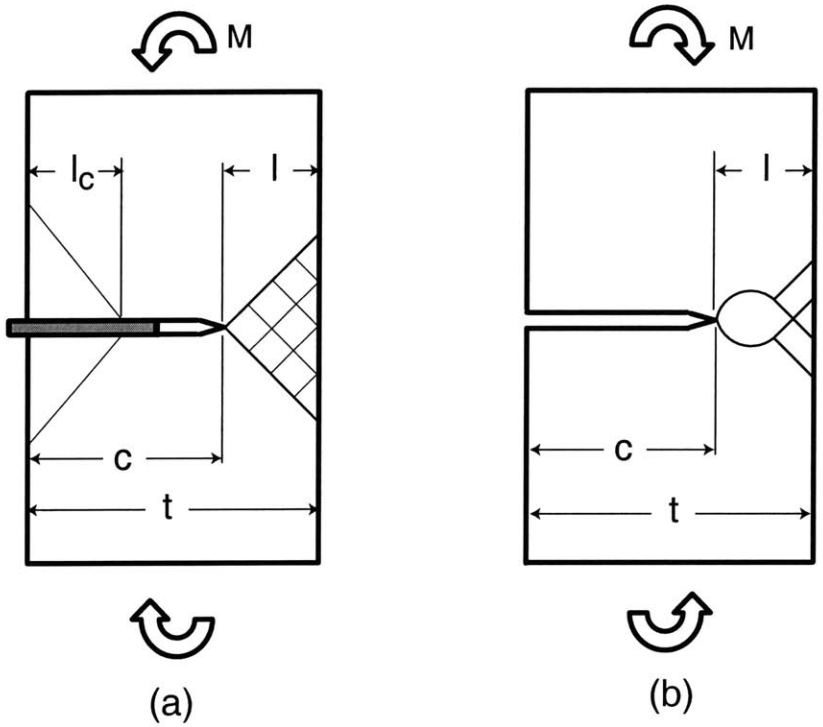

Figure 1-1: Bend loadings with slip lines. (a) Back-bend. (b) Open-bend.

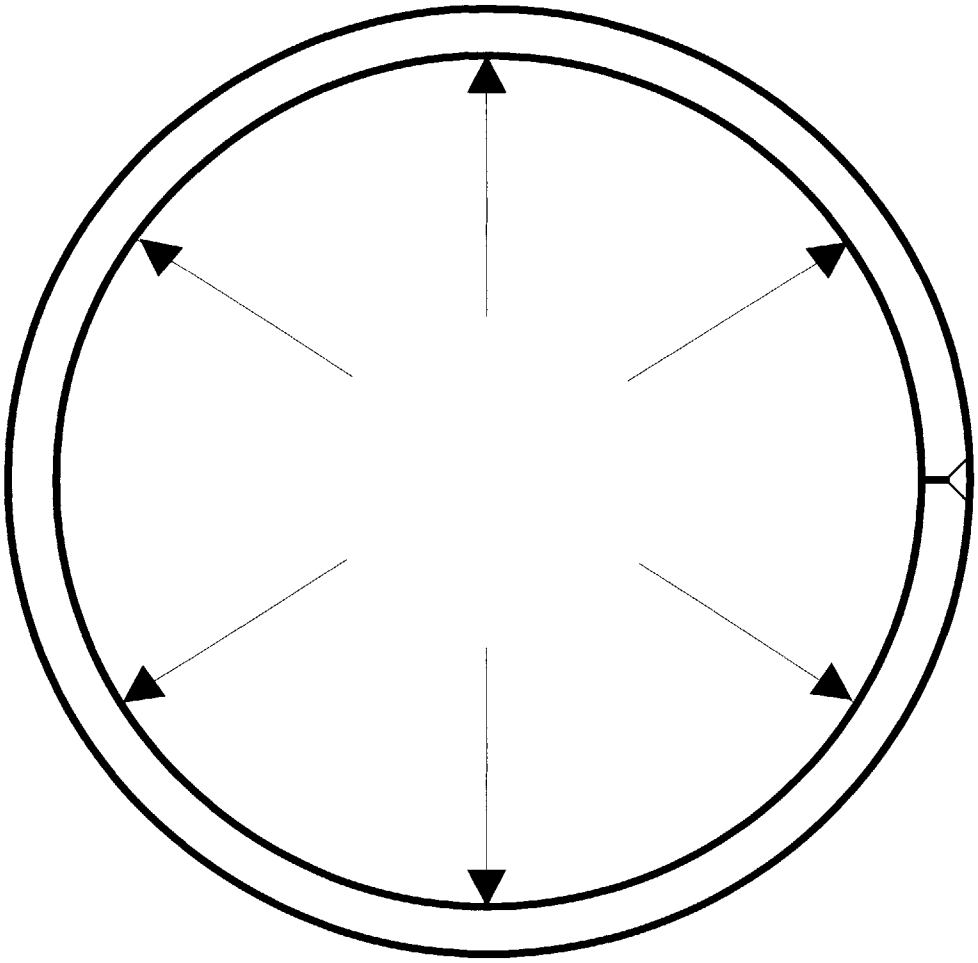

Figure 1-2: Penetrating crack in a pressure vessel (taken from Bass [3]).

Chapter 2

Mechanics of Back-bend and Open-bend Specimens

2.1 Fracture Mechanics Characterization Methods and Parameters

Fracture mechanics methods analyze specimens and engineering structures and develop quantitative characterizations of near-crack-tip stress and strain fields that exist in both a laboratory specimen and an engineering structure. In Linear Elastic Fracture Mechanics (LEFM), the most widely known of these methods, the stress and strain fields in an annular elastic region surrounding the crack-tip are uniquely characterized by the stress intensity factor, K_I. LEFM is valid only when the plastic zone size, r_y, is sufficiently small compared to the specimen ligament, l, or the crack length, c. Furthermore, for plane strain conditions, the breadth, B, must also be large compared to r_y. Two-parameter characterizations of crack-tip fields have been developed using the T-stress (discussed by Parks in [4]). When r_y is larger than the limits of validity of the $K-T$ description, Hutchinson-Rice-Rosengren (HRR) singularity fields, [5] and [6], may describe the stress and strain fields in an annular region surrounding the crack-tip using power-law deformation theory plasticity and the J-integral as the governing parameter. However, these fields are limited to an amount

of crack growth, under a monotonically increasing load, that is small compared to the region dominated by the HRR singularity. The region dominated by finite strain must also be small compared to the HRR field [7]. Two-parameter characterizations, $J - Q$ (Dodds, et al. [8]) and $J - A_2$ (Sharma and Aravas [9] and later Chao and Zhu [10]), have also been considered.

A further regime of fracture mechanics valid for both crack initiation and extended growth is currently being developed by McClintock, et al. [11] and [12]. Slip Line Fracture Mechanics (SLFM) is based on the limiting case of plane strain deformation of rigid-plastic, isotropic non-hardening material. In SLFM, the annular region surrounding the crack-tip is characterized by three crack-tip driving parameters: the slip line direction, θ_s, the normal stress across the slip plane, σ_n, and the increment in relative sliding displacement across the slip plane, du_s. Analogous to K_I and T, or to J and Q, these parameters characterizing the crack-tip field are functions of loading and geometry. The parameters θ_s and σ_n are fixed for a given geometry and loading, so a key quantity for crack initiation is the slip displacement to micro-initiation, u_{si}. An alternative measure for initiation is the critical crack-tip opening displacement, $CTOD_i$. Figure 2-1 shows a schematic of symmetric, Mode I cracking, modeled by two-plane slip line fracture mechanics (SLFM2), which gives the crack-tip response function $CTOD_i$ in terms of u_{si} [11] in a given material under a given crack-tip slip line field:

$$u_{si} = \hat{u}_{si}\left(\theta_s, \frac{\sigma_n}{2k}\right); \tag{2.1}$$

$$CTOD_i = 2\ u_{si} \sin\theta_s. \tag{2.2}$$

Here, $2k$ is the plane strain flow strength. The crack-tip opening angle, $CTOA$, describes continuing crack growth for a given geometry and loading. It is expressed in terms of the ratio of incremental micro-cracking extension per unit slip line displacement increment, dc/du_s, as

$$c_{,u} \equiv \frac{dc}{du_s} = \hat{c}_{,u}\left(\theta_s, \frac{\sigma_n}{2k}\right); \tag{2.3}$$

$$CTOA = 2\tan^{-1}\left[\frac{\sin\theta_s}{\cos\theta_s + c_{,u}}\right]. \tag{2.4}$$

Slip line plasticity determines θ_s, $\sigma_n/2k$ and du_s from the far-field loads, displacements, and rotations.

2.2 Slip Line Fracture Mechanics applied to back-bending

The slip line field for the back-bend test, as obtained from equilibrium, the flow rule, and the yield condition, is shown in Figure 2-2(a). A schematic of this field near the crack-tip is shown in Figure 2-2(c). The slip lines for the back-bend specimen emanate from the crack-tip at $\pm\theta_s$ from the plane of the crack. The stress normal to the slip lines, σ_n, is normalized with respect to the plane strain flow strength, $2k$, where k is the flow strength of the material in shear. For back-bend loading,

$$\theta_s = 45°; \qquad \frac{\sigma_n}{2k} = 0.5. \tag{2.5}$$

The back-bend near-crack-tip slip line field is the same as that of the face-cracked tensile fracture specimen, shown in Figure 2-3(a). This (non-hardening) slip line field is the same as would be seen in a fully-plastic engineering structure under plane strain tensile loading. However, the loads are reduced by using the back-bend specimen; the limit loads for back-bend loading (obtained from equilibrium of the slip line field) and the face-cracked tensile specimen [13] are given in terms of a tensile flow strength σ_{flow}, ligament length l, breadth B, and moment arm s as

$$P_{lim,bb} = \frac{2}{\sqrt{3}}\,\sigma_{flow}\,lB\,\frac{2(t-l)}{s}; \tag{2.6}$$

$$P_{lim,fc} = \frac{2}{\sqrt{3}}\,\sigma_{flow}\,lB. \tag{2.7}$$

Taking the ratio of $P_{lim,bb}$ to $P_{lim,fc}$ results in the following load reduction,

$$\frac{P_{lim,bb}}{P_{lim,fc}} = \frac{2(t-l)}{s}. \tag{2.8}$$

For the geometry used here (see Figure 3-3, below), the limit load for back-bending is only 60% of that for a face-cracked specimen of identical geometry.

The non-hardening slip line field in Figure 2-3(c) for back-bending has two sets of slip lines, similar to a center-cracked specimen, shown in Figure 2-3(b). (The center-crack specimen requires loads twice as large as the face-cracked specimen, when its uncracked ligaments are each equal in size to that of the face-cracked specimen.) However, in back-bending, the slip lines emanating from the right-side crack-tip are in tension, whereas the slip lines emanating from the left-side "crack-tip" are in compression. Both sets of slip lines are oriented at $\pm 45°$ from the crack plane, but the left-side "crack-tip" is more accurately termed a "last point of slot-face contact." The initial crack size, c_0, must be greater than half the thickness of the specimen ($c_0/t > 0.5$) in order to achieve tension on the right and compression on the left, which balance one another in pure bending. When the specimen is loaded in closing bending, the slot faces on the back side will come into contact. Since machined starter notches leave a considerable gap, shim material, as shown in Figure 2-3(c), may be required to help establish contact. Once the specimen has been loaded to full ligament plasticity, equilibrium requires that the length, l_c, over which the slot faces are in contact, should be equal in size to the length, l, of the remaining ligament: this should be a good approximation for low strain-hardening material as well.

Figure 2-3(c) also shows less prominent slip lines in the ligament ahead of the crack growth, which denote the "pre-straining" occurring within that region before the crack-tip advances to a given material point in the ligament. Appendix A.1 discusses details of the pre-straining in back-bend loading, along with further relations for du_s and the crack-tip response functions, $CTOD_i$ and $CTOA$, as obtained from the far-field moments and displacements of back-bend loading using SLFM2.

The slip line field for open-bend loading was given by Green and Hundy (GH) [14]

and is shown in Figure 2-2(b); a near-crack-tip schematic of the GH field is shown in Figure 2-2(d). The slip lines emanate from the crack-tip at $\pm\theta_s$ from the plane of the crack [13], and for open-bend loading,

$$\theta_s = 72°; \qquad \frac{\sigma_n}{2k} = 1.543. \tag{2.9}$$

Appendix A.2 discusses further relations for du_s and the crack-tip response functions, $CTOD_i$ and $CTOA$, as obtained from the far-field moments and displacements of open-bend loading using SLFM2.

The normal stress in Eq. 2.9 for open-bending is more than three times the corresponding value for back-bending in Eq. 2.5, indicating the latter's dramatically lower state of triaxiality. This lower triaxiality can be expected to result in higher measures of local crack-tip ductility, and hence in higher $CTOD_i$, $CTOA$ [15], or both.

Differing levels of triaxiality can become quite important in analyzing structures. If the structure in question has a much lower fully-plastic stress triaxiality than the high-triaxiality laboratory tests used to characterize material cracking resistance, predictions may be excessively conservative, and the actual behavior of the structure could be highly uncertain. Ideally, the triaxiality and flow-field of the laboratory test specimens should be similar to those of the actual structure in order to provide more accurate predictions.

SLFM2 can be used to obtain expressions for the J-Integral at initiation, J_i, and the initial rate of change of J with crack growth, dJ/dc, in terms of $CTOD_i$ and $CTOA$; these were given by McClintock in [12] as:

$$J_i = 2k\ CTOD_i\ \left[\frac{\sigma_n}{2k} + \frac{1}{2\tan\theta_s}\right]; \tag{2.10}$$

$$\frac{dJ}{dc} = \tan\left(CTOA/2\right)\frac{2k\left[2\left(\sigma_n/2k\right)\sin\theta_s + \cos\theta_s\right]}{\sin\theta_s}. \tag{2.11}$$

Values of J at initiation evaluated with these equations are given in Chapter 6, below.

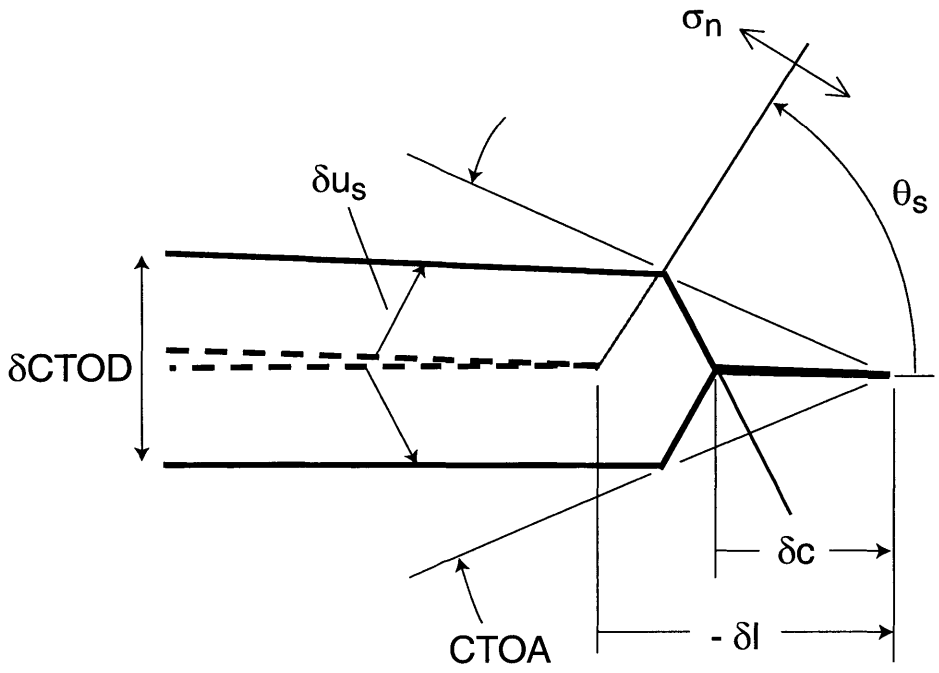

Figure 2-1: Schematic of alternating slip and micro-cracking modeled by SLFM2.

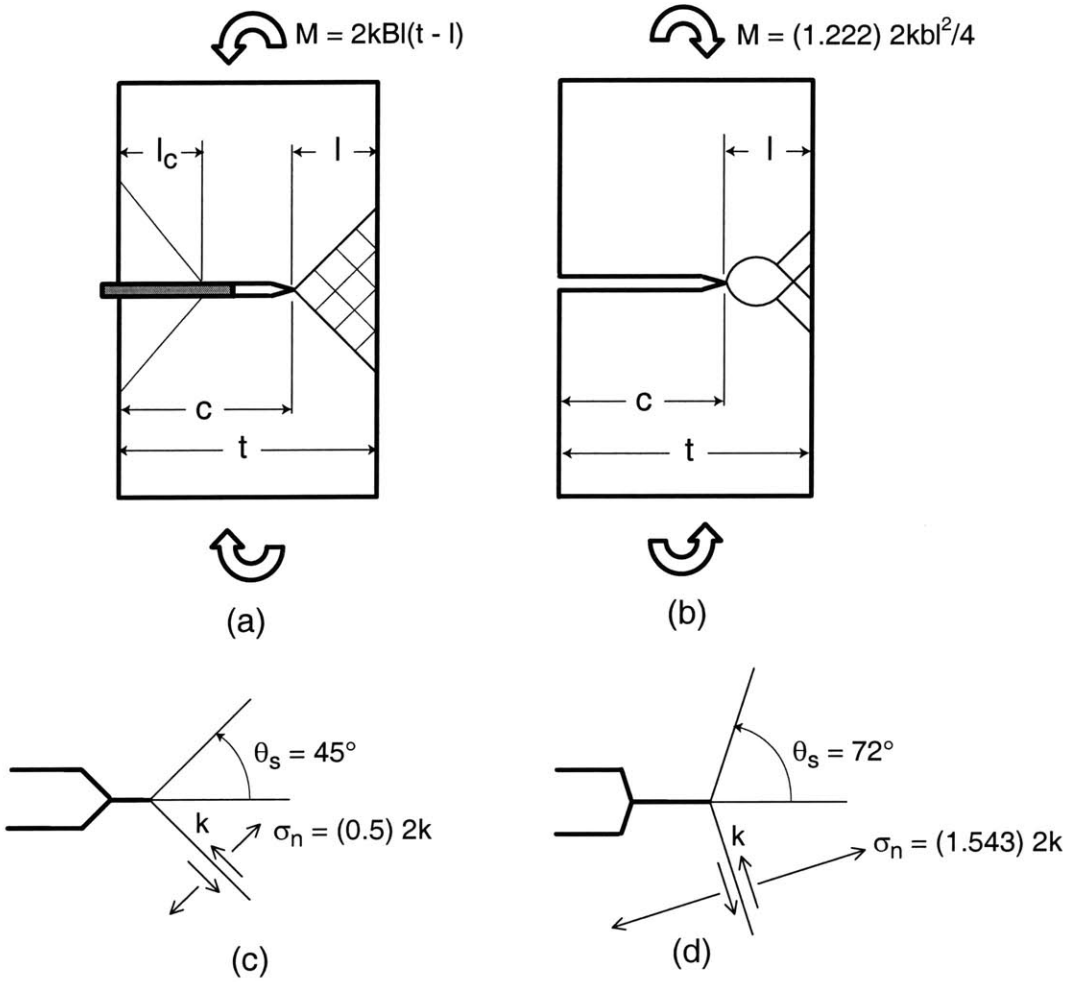

Figure 2-2: Limit load bend loadings with slip lines. (a) Back-bend. (b) Open-bend. (c) Near crack-tip back-bend alternating slip and micro-cracking. (d) Near crack-tip open-bend alternating slip and micro-cracking.

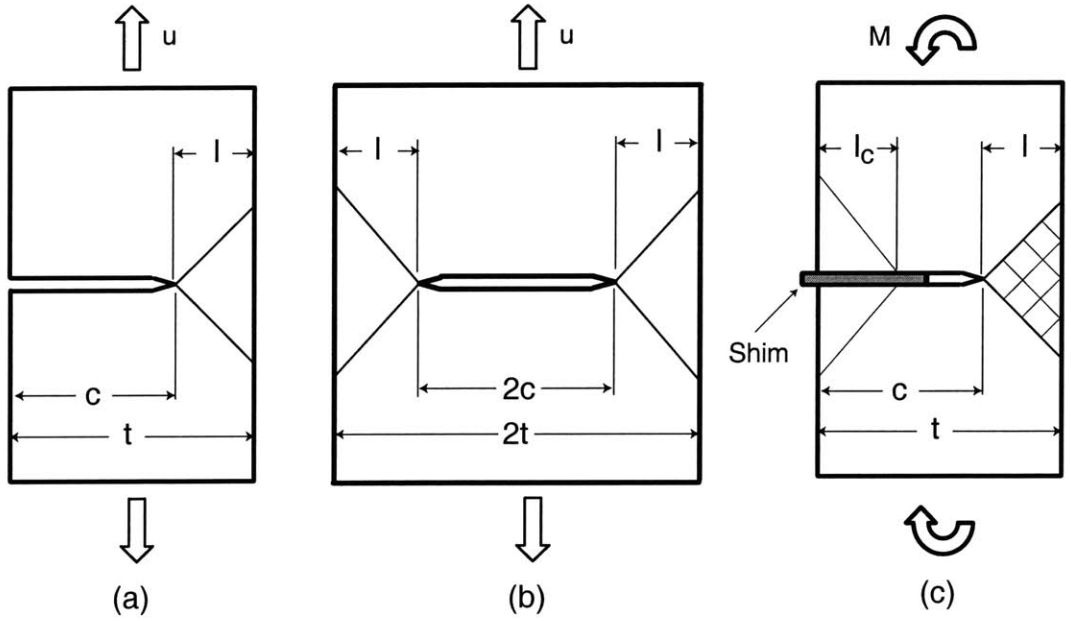

Figure 2-3: Fully-plastic low-triaxiality plane strain specimens. (a) Face-crack under extension. (b) Center-crack. (c) Back-bend. For non-hardening, contact length, l_c, is equal to uncracked ligament, l.

Chapter 3

Experimental and Numerical Procedures

3.1 Experimental Procedure

The material used in the open-bend and back-bend testing was a commercially-obtained structural steel meeting ASTM standard A572 Gr.50. Chemical composition and mechanical properties are shown in Table 3.1. The specimens were machined from rolled plate with a TS crack orientation (crack plane normal to the transverse or width direction, "T," and crack growth in the short-transverse or plate-thickness direction, "S"), as shown in Figure 3-1, for through-thickness penetration of a long surface-crack. As will be noted below, some specimens used in the open-bend tests were incorrectly machined to a TL orientation (crack growth in the longitudinal or rolling direction, "L").

Pictures (825X magnification) of the microstructure of this material are included in Figure 3-2. The steel was apparently not processed according to modern steelmaking practice, for it contained a large number of manganese sulfide (MnS) inclusions [3]. At hot-rolling temperatures, these inclusions are soft and, upon being rolled, flatten into lamellae within planes normal to the S direction. The bonding between the steel and lamellar MnS inclusions is easily broken, creating a crack-like defect along the inclusion surface. Since the inclusions are flattened in the rolling plane, TS cracks

advancing through the thickness of the plate encounter these lamellae normal to the crack plane, thereby causing delaminations normal to the crack plane that create a very uneven fracture surface. Advanced steelmaking techniques have been developed to control such inclusions in steels (see, e.g., Wilson [16]). Since steel of this inferior quality is still currently within the stream of commerce, testing was continued on this material, its lackluster metallurgical pedigree notwithstanding.

The 4-point bending test specimen geometry is shown in Figure 3-3, comprising length, L, moment arm, s, distance between inner rollers, d_1, and breadth, B. The total system displacement u, and the total load P, were recorded in the tests. Here $u = u_m + u_{spec}$ is taken as the sum of the "machine" displacement, u_m, and "specimen" displacement, u_{spec}. The machine stiffness, K_m, and compliance C_m relate load to u_m by

$$u_m = \frac{P}{K_m} = PC_m. \tag{3.1}$$

Specimen displacement $u_{spec} = u^e_{spec} + u^p$ is the sum of an "elastic portion," u^e_{spec}, and a "plastic portion," u^p. Specimen compliance, C_{spec}, which depends on ligament length, l, provides

$$u^e_{spec} = C_{spec}(l) \cdot P. \tag{3.2}$$

Thus, u^p is given by

$$u^p = u - (C_m + C_{spec}) \cdot P. \tag{3.3}$$

Prior to quasi-static testing ($du/dt = 0.5$ mm/min), all specimens were fatigue pre-cracked in open-bending from a 45° chevron starter notch to $c_0/t \approx 0.75$, giving a nominal initial ligament length of $l_0 = 6.35$ mm. The back-bend setup included a 1.57 mm thick stainless steel shim to close the slot. The shim material had a hardness, $H_{RC} = 40$, correlating to a tensile strength of approximately 1250 MPa. The A572 Gr.50 steel had a hardness, $H_{RB} = 83$, correlating to a tensile strength of approximately 552 MPa. Thus, the shim is significantly harder than the steel being tested, and for modeling purposes was treated as rigid.

3.2 Numerical Procedure

3.2.1 Finite Element Analysis

Finite element analysis of both back-bend and open-bend loading was performed, and compared with experimental results. The ductile tearing was modeled by a layer of special interface finite elements abutting the symmetry plane ahead of the crack. These elements used the Gurson-Tvergaard-Needleman (GTN) porous plasticity model for void-containing materials [17] - [20] to represent void nucleation, growth and coalescence. Ductile tearing has been modeled in a similar manner, using the GTN model and interface elements, by Shih, et al. [21] and many others (e.g. [22], [23]). The GTN model has been implemented in ABAQUS/Explicit, Version 5.8 [24], along with element deletion to complete damage, as discussed in Section 3.2.2, below. The Poisson's ratio was taken as $\nu = 0.3$ and the Young's modulus as $E = 207$ GPa. The strain-hardening of the matrix was obtained from the true stress-strain curve, shown in Figure 3-4, obtained from an ASTM standard compression test.

Both 2-D plane strain and fully 3-D simulations were conducted. The 2-D model, shown in Figure 3-5(a), modeled one-half of the specimen. The ligament mesh used elements aligned at 45° to the crack plane, as shown schematically in Figure 3-5(b), to better capture the anticipated slip line field in the back-bend specimen. The 2-D mesh used plane strain, 4-node, reduced-integration elements with hourglass control; near the crack plane element length was $l_{el} = 0.24$ mm, and the layer thickness was $t_{el} = l_{el}/2$. Triangular-shaped elements were used within and adjacent to the layer of interface elements. The 3-D mesh (shown in Figure 3-6) modeled one-quarter of the specimen, and was an extrusion of the 2-D mesh into one-half of the breadth of the specimen, using 8-node, reduced-integration elements with hourglass control. The 3-D mesh had 10 non-uniform-length elements along the breadth, with smaller elements near the traction-free surface.

The machine compliance was modeled in both 2-D and 3-D analyses as a spring in series with the specimen. The machine stiffness ($K_m = 45 \times 10^3$ N/mm in the plane strain simulations and $K_m = 25 \times 10^3$ N/mm in the 3-D simulations) was chosen to

match the initial slopes of finite element analysis and experimental load-displacement curves for both back-bending and open-bending. The GTN model was used throughout the mesh, with the element failure in only one layer of interface elements near the crack-tip. Other distributions of the GTN model were considered, as discussed in Chapter 5, below. The rollers were modeled as frictionless rigid surfaces. The loading was applied through a smoothly ramped-up displacement boundary condition. In all simulations considered, ABAQUS/Explicit automatic time incrementation was used, and mass scaling was used to decrease the run computation time. Mass scaling was done by increasing the mass density from its actual value of $\rho = 7.83 \times 10^3$ kg/m^3; for the 3-D back-bend simulations, ρ was scaled up by a factor of 10, resulting in a run computation time of 50 h on a Compaq AlphaStation XP1000. Since the quasi-static tests were analyzed using explicit dynamics, the computed load-displacement curves show oscillations. However, the ratio of system kinetic energy to the total deformation energy of the model was monitored for all runs, so as to keep it at a suitably small value; for the 3-D back-bend simulations, the kinetic energy was at all times less than 1% of the total deformation energy.

3.2.2 Gurson-Tvergaard-Needleman evolutionary fracture model

The Gurson-Tvergaard-Needleman (GTN) [17] - [20] approach models plastic flow of a void-containing material as a homogenized continuum, with the effects of the voids averaged through the material. The yield condition is

$$\Phi = \left(\frac{\sigma_{eq}}{\sigma_y}\right)^2 + 2q_1 f^* \cosh\left\{q_2 \frac{3\sigma_m}{2\sigma_y}\right\} - \left[1 + (q_1 f^*)^2\right] = 0, \tag{3.4}$$

where σ_y is the matrix flow strength, and σ_{eq} and σ_m are the Mises equivalent stress and the mean hydrostatic stress of the void-containing material, respectively. The material parameters q_1 and q_2 were taken from the literature as $q_1 = 1.5$ and $q_2 = 1.0$. The function $f^*(f)$ models the rapid loss of stress-carrying capacity accompanying void coalescence in terms of constants f_c and f_F, and is given as a function of the

(evolving) void volume fraction f, by

$$f^* = \begin{cases} f & \text{if } f \leq f_c, \\ f_c + \left(\bar{f}_F - f_c\right) \frac{f - f_c}{f_F - f_c} & \text{if } f_c < f \leq f_F. \end{cases} \tag{3.5}$$

Here,

$$\bar{f}_F = \frac{1}{q_1}. \tag{3.6}$$

The constants f_c and f_F denote the range of f over which there is rapid material weakening due to mechanisms such as micro fracture and void coalescence. When f exceeds f_F, total failure at the material point has occurred. In ABAQUS/Explicit an element is removed once its material point fails [24].

After an assumed initial void volume fraction, f_0, the growth and nucleation of voids is modeled by

$$\dot{f} = \dot{f}_{growth} + \dot{f}_{nucleation}, \tag{3.7}$$

where $\dot{f}_{growth}$ is the rate of change in void volume fraction due to growth of existing voids, and $\dot{f}_{nucleation}$ is the change corresponding to nucleation of secondary voids. Growth of voids is based on conservation of mass in a plastically incompressible matrix, and is given by

$$\dot{f}_{growth} = (1 - f)\, \dot{\varepsilon}^p_m, \tag{3.8}$$

where $\dot{\varepsilon}^p_m$ is the volumetric plastic strain increment. The nucleation of voids is assumed to be given by a strain-controlled relation,

$$\dot{f}_{nucleation} = \frac{f_N}{s_N \sqrt{2\pi}} \exp\left\{ -\frac{1}{2} \left(\frac{\varepsilon^p_{eq} - \varepsilon_N}{s_N} \right)^2 \right\} \dot{\varepsilon}^p_{eq}. \tag{3.9}$$

Here $\dot{\varepsilon}^p_{eq}$ is the equivalent plastic strain increment, ε_N is the mean void nucleation strain, s_N is the standard deviation of the void nucleation strain, and f_N is the volume fraction of the nucleated void. Typical numerical values for void nucleation parameters ε_N, s_N and f_N, as well as for the initial void volume fraction f_0, and the material failure parameters, f_c and f_F, were chosen to match the numerical solution

to the experimental curves, and will be discussed later. They are summarized in Table 3.2.

Lastly, the volumetric and equivalent plastic strain increments, $\dot{\varepsilon}^p_m$ and $\dot{\varepsilon}^p_{eq}$, are proportional to the derivatives of the yield function $\Phi = 0$ with respect to σ_m and σ_{eq}, respectively. The Lagrangian strain increments, based on current state as reference, $\dot{\varepsilon}_{ij}$, are the sum of an elastic part, $\dot{\varepsilon}^e_{ij}$, and a plastic part $\dot{\varepsilon}^p_{ij}$,

$$\dot{\varepsilon}_{ij} = \dot{\varepsilon}^e_{ij} + \dot{\varepsilon}^p_{ij}; \tag{3.10}$$

where the plastic part follows from the normality rule:

$$\dot{\varepsilon}^p_{ij} = \Lambda \frac{\partial \Phi}{\partial \sigma_{ij}}. \tag{3.11}$$

Here σ_{ij} are the Cauchy stress tensor components. The parameter Λ is obtained from the consistency condition $\dot{\Phi} = 0$. Further discussion is given by Tvergaard in [18].

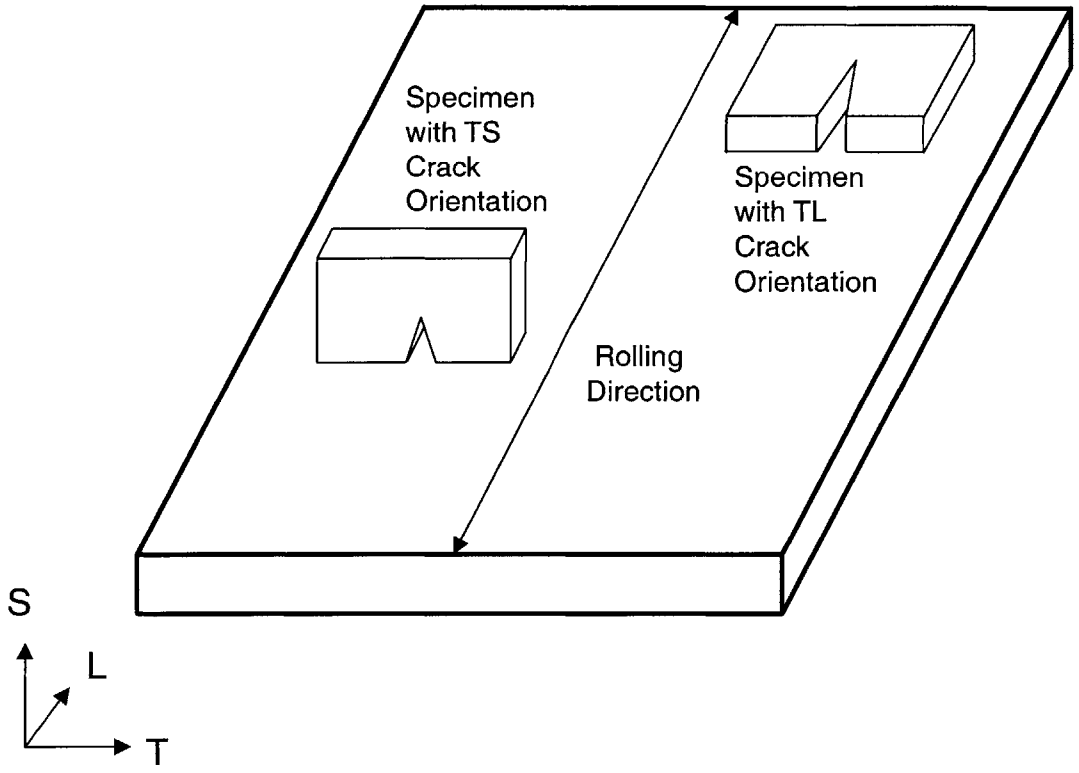

Figure 3-1: Nomenclature for crack orientations in a rolled plate.

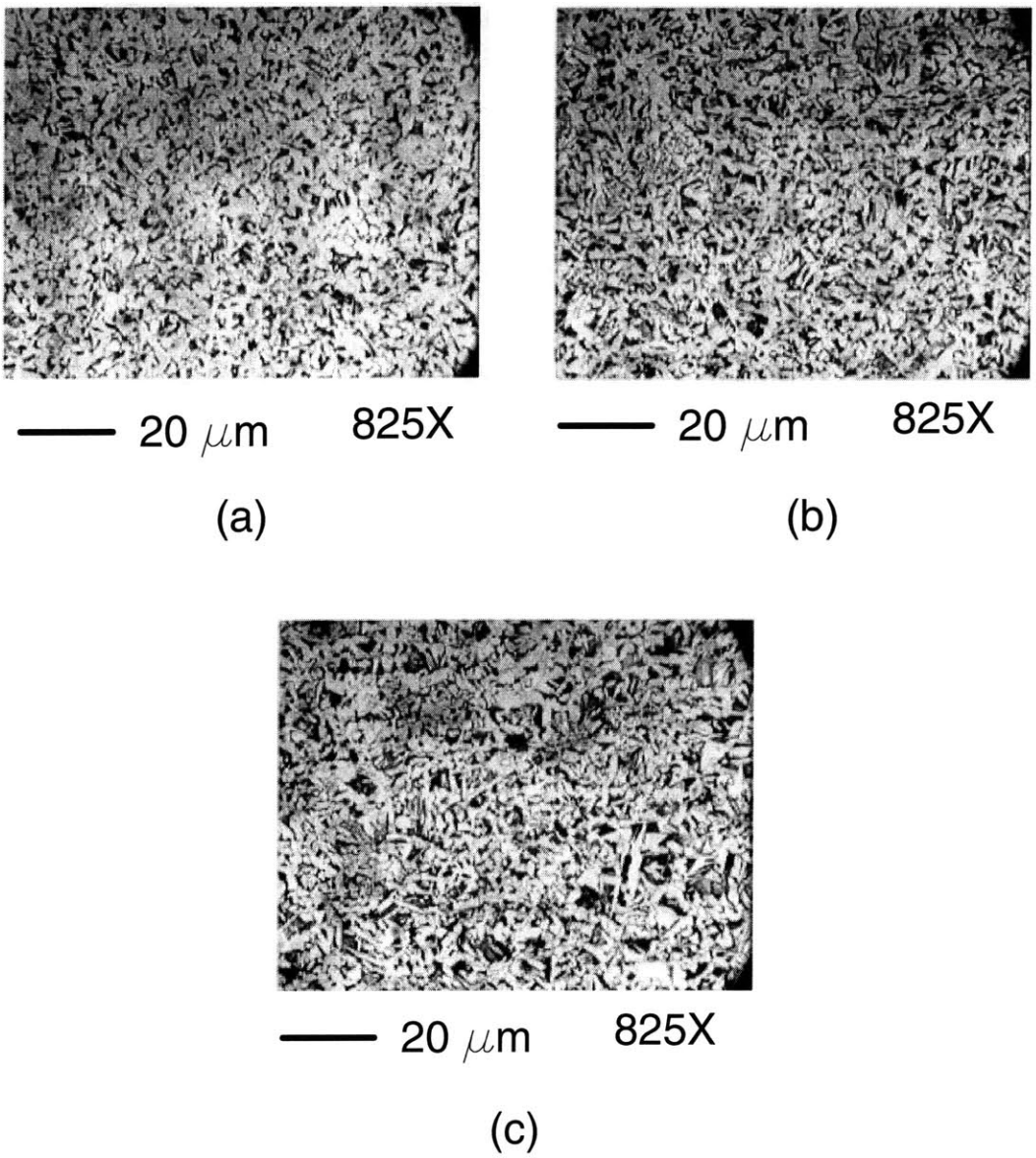

Figure 3-2: Pictures of material microstructure from Bass [3]. (a) Plane normal to S, short transverse direction. (b) Plane normal to L, rolling direction. (c) Plane normal to T, long transverse direction.

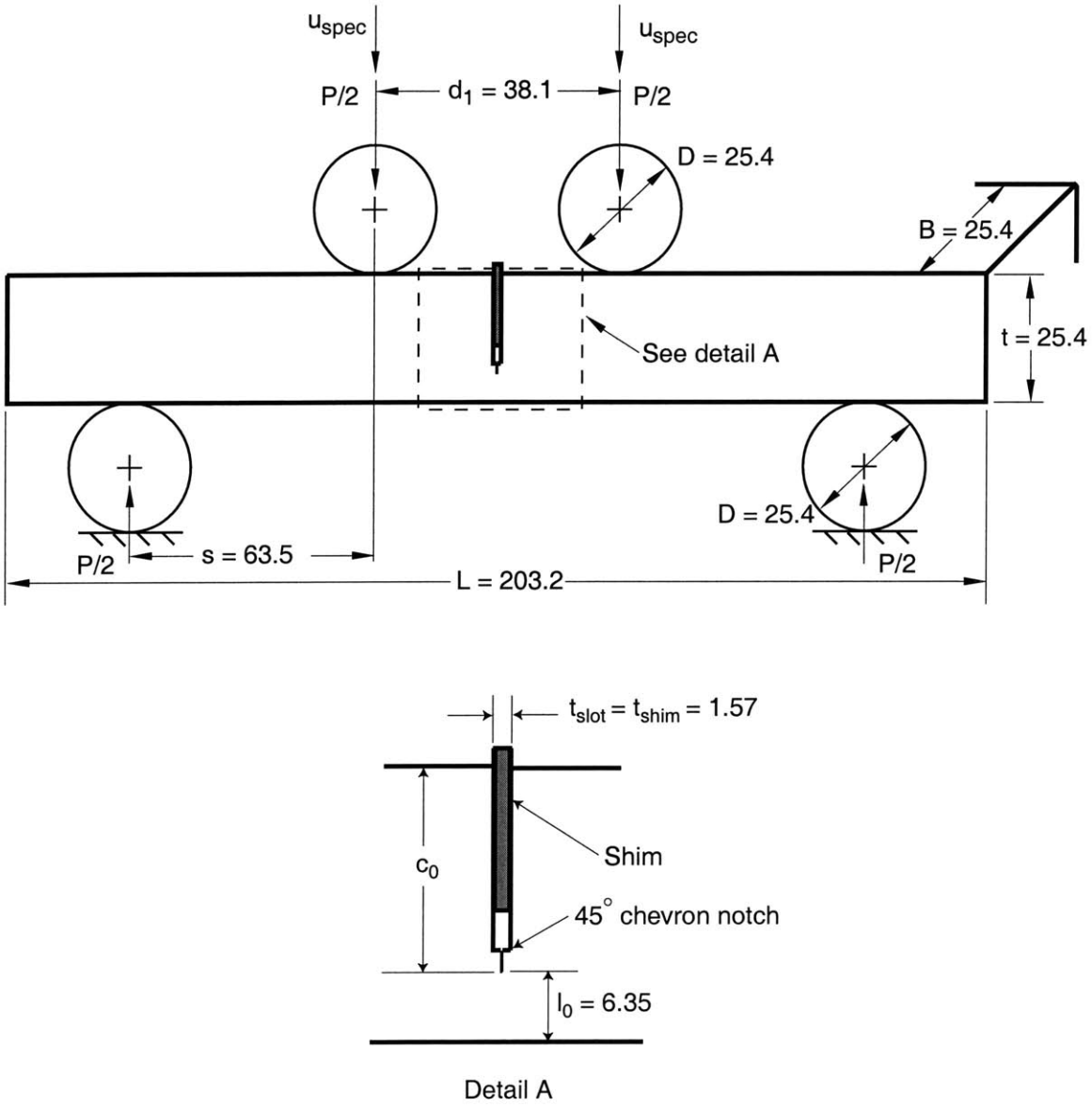

Figure 3-3: Back-bend test specimen geometry. All dimensions in mm.

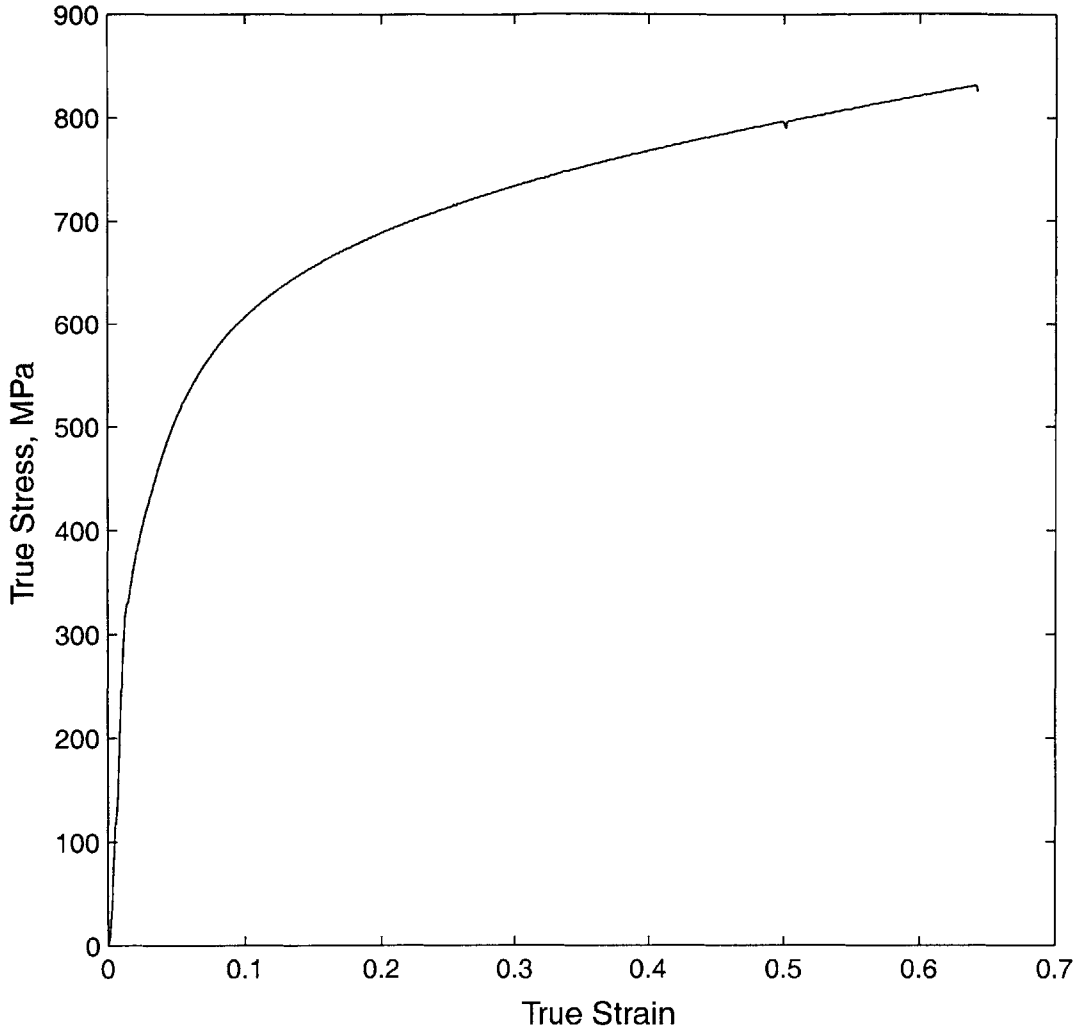

Figure 3-4: True stress-strain curve from ASTM standard compression test on A572 Gr.50 steel, from Bass [3].

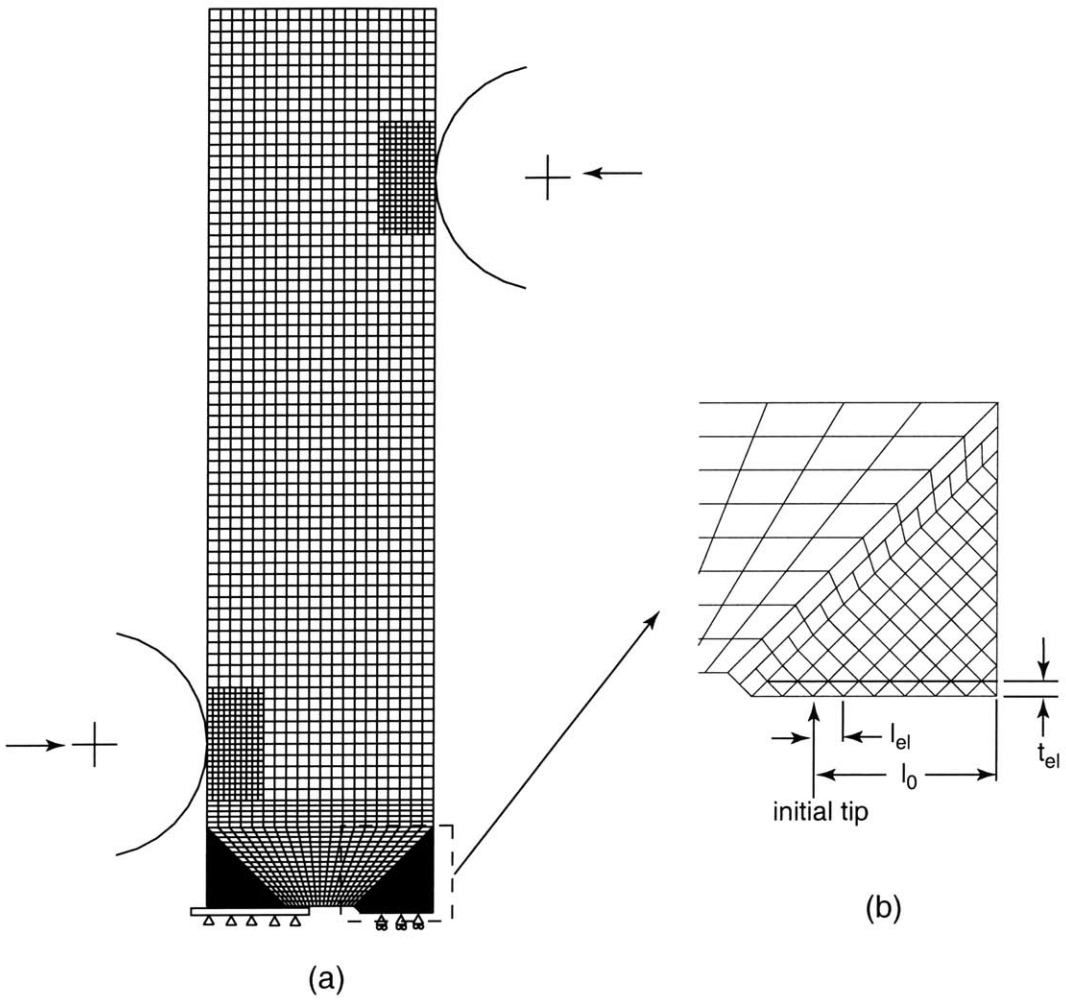

Figure 3-5: Finite element model. (a) 2-D back-bend finite element model. (b) Schematic of 2-D finite element mesh.

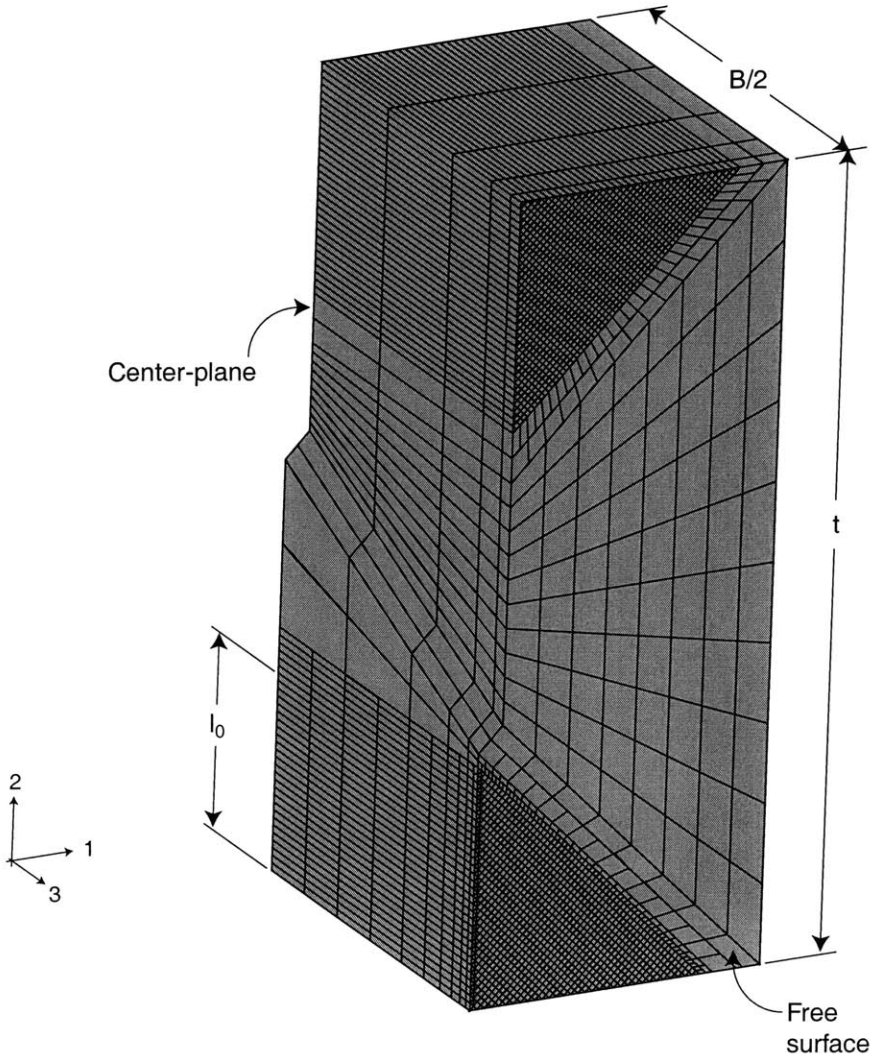

Figure 3-6: 3-D finite element mesh of one-quarter specimen.

Chemical Composition (weight %)						σ_y	σ_{TS}
C	Fe	Mn	P	S	Si	(MPa)	(MPa)
0.19	98.39	1.04	0.024	0.026	0.33	353	558

Table 3.1: Chemical composition and mechanical properties of the A572 Gr.50 steel tested.

f_0	ε_N	s_N	f_N	f_c	f_F
0.002	0.30	0.10	0.04	0.15	0.25

Table 3.2: Parameters used in Gurson-Tvergaard-Needleman model.

Chapter 4

Experimental Results

The load, P, was measured as a function of the total system displacement, u. Many forensic techniques were also used by Bass [3], including sectioning the specimen, fractographs, and topographs. These experimental results are interpreted here in terms of SLFM2.

4.1 Load-displacement

Back-bend tests were stopped post-peak at 10%, 20%, 40%, 60% and 100% load-drop, to allow sectioning, as shown in the load-displacement curves in Figure 4-1. The upward curvature for the first fraction of a mm displacement appears to be due to the seating of the rollers and establishment of contact between the slot faces and the shim. The curves show differences in the maximum observed load, P_{max}. These differences are partially explained by variations in initial ligament length, l_0. Table 4.1 lists l_0-values of each specimen (as measured from fractographs, discussed below), as well as the ratio $P_{max}/P_{lim}(l_0)$ as calculated from the limit load relation of Eq. 2.6 using $\sigma_{flow} = \sigma_{TS}$, where σ_{TS} is the tensile strength. The values show the maximum observed loads are within 11% of the calculated limit loads. An alternate comparison of curves is obtained by calculating the flow strengths, σ_{flow}, from Eq. 2.6. Table 4.1 shows σ_{flow} calculated at peak using Eq. 2.6 is is 601 MPa $\pm$5%.

The plastic specimen displacement at peak load, $u^p_{(P_{max})}$, is listed in Table 4.1.

Cross-plotting with l_0, as shown in Figure 4-2, shows a 10% increase in l_0 gives a $\sim 70\%$ increase in $u^p_{(P_{max})}$. Similar results are seen in the finite element runs; the plane strain simulations show that a 10% increase in l_0 causes a $\sim 20\%$ increase in $u^p_{(P_{max})}$. Assuming initiation occurs at peak load, $CTOD_i$ in terms of the plastic specimen displacement at maximum load, $u^p_{(P_{max})}$ is given by Eq. A.4 of the Appendix A.1 as

$$CTOD_i = 2(t - 2l_0)\frac{u^p_{(P_{max})}}{s}. \tag{4.1}$$

For the specimen of Fig 3-3, Eq. 4.1 with $CTOD_i$ taken as a constant, indicates a 10% increase in l_0 gives 11% increase in $u^p_{(P_{max})}$.

The $CTOD_i$ calculated using l_0-values and Eq. 4.1 is between 1.2 mm and 2.8 mm for the back-bend specimen, as listed in Table 4.1. Since these values are calculated from plane strain, rigid-plastic, non-hardening approximations, and since from Figure 4-1, the "initiation" of tearing is perhaps at displacements 10% less than peak-load displacement, the $CTOD_i$ inferred from the present procedure will be higher than the values obtained from topographs and finite element runs, below. Since the steel had substantial strain-hardening, neglecting extra deformation in the shoulders causes the above-calculated $CTOD_i$-values to overestimate the actual values.

The $CTOA$ can also be calculated from the load-displacement curves using SLFM2. For back-bending the $CTOA$ can be calculated from the load-drop dP/du^p by Eq. A.12 of the Appendix

$$c_{,u} = \left(\frac{-\left(dP/du^p\right)/\left(P_{max}/s\right)}{\sqrt{2}\left(1/\left[\lambda_0(1-\lambda_0)\right] - 4\mu\right)}\right) - 2\cos\theta_s, \tag{4.2}$$

along with $\theta_s = 45°$ from SLFM2 and Eq. 2.4 for $CTOA$. Here, $\lambda_0 \equiv (l_0/t)$, $\mu \equiv P/P_{max}$ and dP/du^p is obtained from the post-peak slope dP/du of the load-displacement curve using Eq. A.13. This procedure gives a $CTOA$ that decreases from 30°, as the crack grows, to $23° - 26°$ as seen in Figure 4-3 and listed in Table 4.2; $CTOA$-values are discussed further below.

Open-bend tests were stopped post-peak at 10%, 20%, 40%, 60% and 100% load-

drop as shown in the load-displacement curves in Figure 4-4. The open-bend limit load, $P_{lim,ob}$, is (e.g. [13])

$$P_{lim,ob} = (1.222)\ \frac{2}{\sqrt{3}}\ \sigma_{flow}\ 2B\ \frac{l^2}{4s}. \tag{4.3}$$

There is a second-power dependence of the limit load, $P_{lim,ob}$, on the ligament size, l. Table 4.1 lists the l_0-values of each specimen as well as the ratio $P_{max}/P_{lim}(l_0)$ as calculated using Eq. 4.3 with $\sigma_{flow} = (\sigma_y + \sigma_{TS})/2$, where σ_y is the 0.2% offset yield strength. The observed peak loads are within 11% of the calculated limit loads. This includes differences due to the fact that different crack orientations were tested in the 20% and the 60% load-drop cases, which were incorrectly machined to a TL crack orientation. Table 4.1 shows the flow strengths calculated at peak yield using Eq. 4.3 are 484 MPa ±5%.

For open-bending, the $CTOD_i$ from peak load displacement and Eq. A.24 of the Appendix A.2 using SLFM2 is

$$CTOD_i = (0.338)\, 2l_0 \frac{u^p_{(P_{max})}}{s} \sin\theta_s. \tag{4.4}$$

The $CTOD_i$ calculated using l_0-values and Eq. 4.4 is between 0.07 mm and 0.27 mm for the open-bend specimens, as listed in Table 4.1. These values show that the $CTOD_i$ for the low-triaxiality back-bend test, calculated above as 1.2 mm to 2.8 mm, indeed exceeds that of the high-triaxiality open-bend test.

For open-bending the $CTOA$ can be calculated from the load-drop dP/P_{max} by Eq. A.27 of the Appendix:

$$c_{,u} = \frac{-1}{2(0.388)} \frac{(dP/du^p)}{(P/s)}, \tag{4.5}$$

along with $\theta_s = 72°$ from SLFM2 and Eq. 2.4 for $CTOA$. The post-peak slope of the open-bend load-displacement curves gives $CTOA$-values of 9° to 11° as seen in Figure 4-5 and listed in Table 4.3. These values show that the $CTOA$ for the low-triaxiality back-bend test, calculated above as 30° to 23° – 26°, exceeds that of the

high-triaxiality open-bend test, as expected. From McClintock, et al. [11], the total fracture shear strain in the band γ_f is given in terms of the $CTOA$ as:

$$\gamma_f = \left(\sin\theta_s \left[\frac{\sin\theta_s}{\tan\left(CTOA/2\right)} + \cos\theta_s \right] \right)^{-1}. \tag{4.6}$$

For back-bend, $CTOA = 30°$ gives $\gamma_f = .42$ and equivalent strain, $\epsilon_{eq} = \gamma_f/\sqrt{3} = .24$. For open-bend, $CTOA = 11°$ gives $\gamma_f = .10$ and $\epsilon_{eq} = .06$. These values show the local strains are much lower in the high-triaxiality open-bend loading when compared to the low-triaxiality back-bend loading. This can be expanded to conclude that the average strain in the ligament in open-bending is smaller than that in back-bending. This is consistent with the use of a lower value of $\sigma_{flow} = (\sigma_y + \sigma_{TS})/2$ in Eq. 4.3 for the open-bend limit load, as opposed to $\sigma_{flow} = \sigma_{TS}$ in Eq. 2.6 for the back-bend limit load.

4.2 Sectioning and Fractography

All unloaded specimens were sectioned by Bass [3] to obtain mid-plane crack profiles, as shown in Figures 4-6 and 4-7 for back-bending and open-bending, respectively. These profiles were used to measure the opening displacement of the initial crack-tip, CT_0OD, at an amount of crack growth, Δc. The sections showed prominent delaminations normal to the fracture surface. These inclusion-generated delaminations were more evident in the open-bend specimens than in back-bend specimens, due to the higher triaxiality in open-bending, which lead to more delaminations of the MnS inclusions. Such delaminations were not observed in sectioning of the open-bend specimens loaded to 20% and 60% load-drop, as they were incorrectly machined with a TL crack orientation.

In order to view the fracture surfaces, the unloaded and sectioned specimens were thermally equilibrated in liquid nitrogen and bent in an opening mode with an impact, to mark the pre-existing crack front by cleavage. The resulting fractographs of approximately one-half of the back-bend and open-bend fracture surfaces are shown

in Figures 4-8 and 4-9, respectively. From bottom to top in each image, the figures show the chevron starter notch, the fatigue pre-crack region, the stable ductile tearing, the final cleavage, and the drawn-in back surface. These fractographs were used to obtain an averaged initial ligament length, l_0, and ductile crack growth, Δc, of each specimen. These values are listed in Table 4.4 along with a calculated Δc based on limit loads using Eqs 2.6 and 4.3.

Figures 4-9(b) and (d) from the 20% and 60% load-drop open-bend tests show vertical delaminations or "slits" parallel to the crack extension direction. Higher magnification SEM fractographs show similar features [3]. These delaminations are consistent with these specimens being in the incorrect TL orientation, where the rolling plane containing the delaminations is normal to the crack front. The high-triaxiality and local plane strain of the open-bend slip line field generates a stress component sufficiently large to open planar delaminations normal to the crack front. These prominent delaminations are caused by the presence of a large number of MnS inclusions in the current steel, as was discussed in Chapter 3.

The values of the opening displacement at the initial crack-tip, CT_0OD, measured from the mid-plane sections, and the crack growth, Δc, measured from the fractographs, are plotted in Figure 4-10 for both loadings. Open-bend data points for the 20% and 60% load drops had the incorrect TL crack orientation, and thus they do not agree with the rest of the open-bend data. While large delaminations in the open-bend loading rendered accurate measurement of the CT_0OD from the mid-plane sections problematic, the plot nonetheless shows that the lower-constraint back-bend crack-tip displays higher crack initiation toughness, than does the higher-constraint open-bend crack-tip. The back-bend data deviates from a blunting line at a higher value of CT_0OD than does the open-bend data. The blunting line denotes the alternating sliding which takes place before crack initiation [13], and determines the shape of the blunting crack. The deviation from the blunting line can be used to represent crack initiation. It is given by the following equation, for $\theta_s = 45°$ corresponding to the back-bend loading, as

$$\Delta c_{bl} = \frac{1}{2} CT_0OD. \tag{4.7}$$

The slope of the data points in the stable tearing range of Figure 4-10 can be used to compare qualitatively the respective $CTOA$-values of the back-bend and open-bend specimens, but with an important caveat, as noted below. The "slopes" in Figure 4-10 for the back-bend versus the open-bend are not considerably different. One contributing factor is that, as the crack grows in back-bend loading, the end-to-end rotation of the specimen tends to reduce the opening between any matching pair of points on the crack faces. In the open-bend case, the opposite is true: as the crack grows, the end-to-end rotation of the specimen adds to the separation. Since CT_0OD is the separation of points on the fracture surfaces marking initial fatigue pre-crack-tip, these tendencies apply to Figure 4-10. Thus the schematic insert, which shows the horizontal (non-rotated) pre-crack fracture surfaces become increasingly misleading with increasing Δc (and rotation).

4.3 Topographs

A CyberOptics Model DRS-2000 laser profilometer was used by W. R. Lloyd of INEEL to acquire height measurements on the broken halves of both specimen types. The heights z are plotted as 3-D topographical maps of the fracture surface at 0.25 mm x and y intervals in Figures 4-11(a) and (b), and Figures 4-12(a) and (b), for back-bend and open-bend, respectively. The z-axis on all four topographic plots was exaggerated by a factor of six to help show height differences. The maximum height difference, between the lowest point on the fracture surface and the highest point, is larger for the back-bend specimen than for the open-bend specimen, as expected from higher crack-growth ductility in the back-bend specimen resulting from its lower triaxiality.

The $CTOD_i$ can be found from the topographs. Since the fracture surfaces were rough, data from the central 10 mm of the fracture surface was used to obtain the averaged profile plots of Figures 4-11(c) and 4-12(c) for back-bending and open-bending, respectively. From the crack-tip blunting in these profile plots, $CTOD_i$ can be measured. The back-bend profile gives $CTOD_i = 0.4$ mm and the open-bend profile gives $CTOD_i = 0.1 - 0.2$ mm.

The $CTOA$ for back-bending was found from the profile plot in Figure 4-11(c). The instantaneous contact length between the slot faces and the shim, l_c, equals (to the first order) the current length of the remaining ligament, l, as noted in Chapter 2. Reference lines were drawn from the instantaneous crack-tip of ligament length l, to the (contact) pivot point at $l_c = l$ and the current center-line of the shim thickness as shown in Figure 4-13(a). Note that the curvatures of the contact face profiles in Figure 4-11(c) emphasize the plastic deformation occurring under contact with the shim. The crack-tip opening angle, $CTOA$, is the sum of angles

$$CTOA = \Theta^p_{top} + \Theta^p_{bot}, \tag{4.8}$$

where Θ^p_{top} is the angle between the "top" reference line and corresponding local crack face, and Θ^p_{bot} is the same for the "bottom" reference line, as illustrated in Figure 4-13(a). Using Eq. 4.8, the $CTOA$ for the back-bend decreases from 35° to 20° with increasing crack growth as seen in Figure 4-13(b).

The $CTOA$ for open-bending was derived from from the profile plot in Figure 4-12(c) as follows. Reference lines were drawn from the instantaneous crack-tip of ligament length l, at an angle θ^p, one-half of the end-to-end plastic rotation, as shown in Figure 4-14. The angles between the local crack faces and the corresponding reference lines, Θ^p_{top} and Θ^p_{bot}, gave the $CTOA$ using Eq. 4.8. The θ^p for the open-bend specimen at a remaining ligament length l was calculated using the load-displacement curves, and the equations,

$$\mu = \frac{P}{P_{max}} = \left(\frac{l}{l_0}\right)^2, \tag{4.9}$$

$$\tan\left(\theta^p\right) = \frac{u^p(\mu)}{s}. \tag{4.10}$$

The resulting open-bend $CTOA$-values increase from 13° to 17° with increasing crack growth, perhaps due to delamination discussed in Section 4.2. These $CTOA$-values, which are consistent with prior estimates made based on dP/du^p, are again lower than the back-bend values obtained from the topographs.

Table 5.1 summarizes the experimental results for the $CTOD_i$ and $CTOA$, and

indicates higher values in back-bending, as expected from the lower normal stresses. The $CTOD_i$ was calculated from the load-displacement curves, but from the curvature in these plots, taking peak load as initiation may give an overestimate. Such values can, however, be used qualitatively and show a higher $CTOD_i$ for back-bending. The $CTOA$ obtained from both load-displacement curves and topographs using SLFM2 is $\sim 30^\circ$ for the back-bend, compared to $\sim 13^\circ$ for the open-bend.

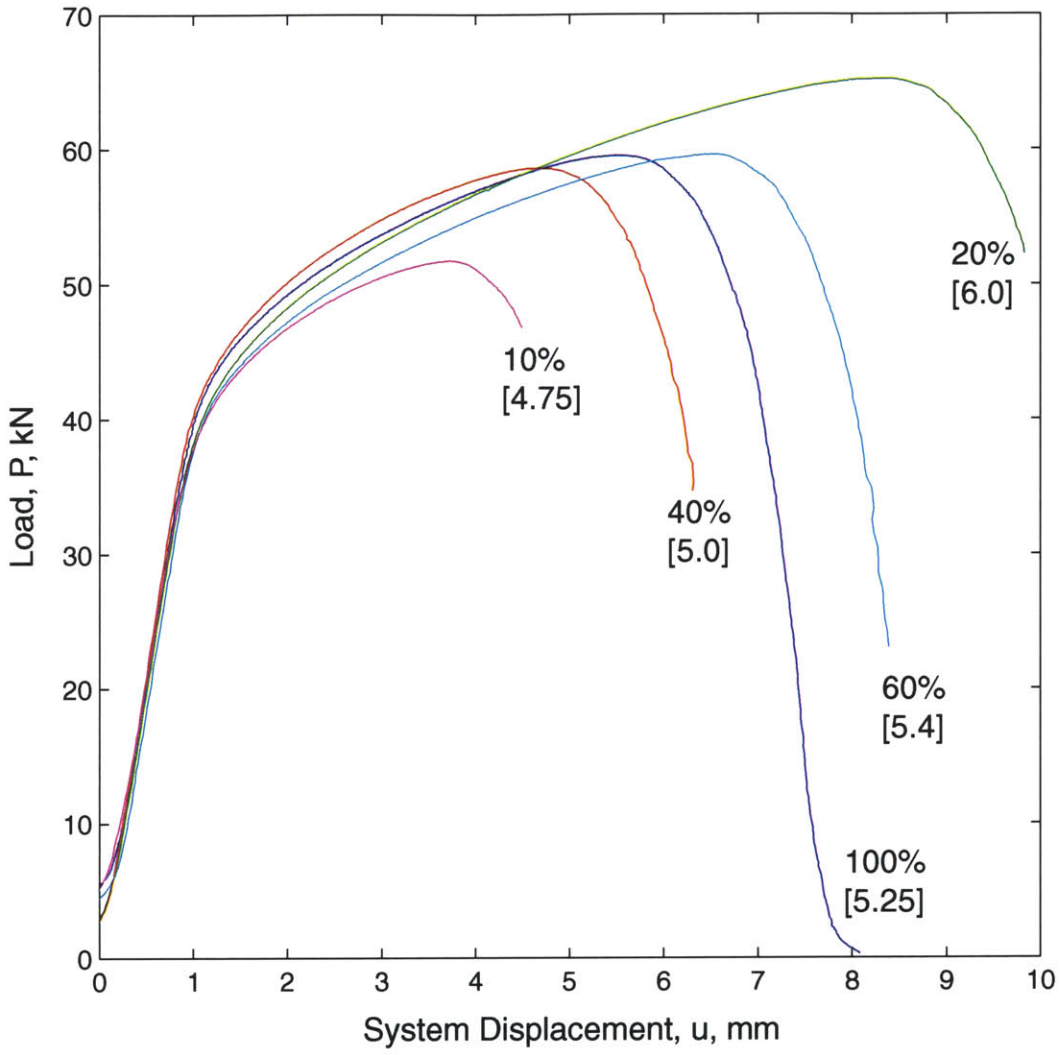

Figure 4-1: Back-bend experimental load-displacement curves. Percentages are post-peak load-drops. Values in square brackets are the initial ligament length, l_0, in mm.

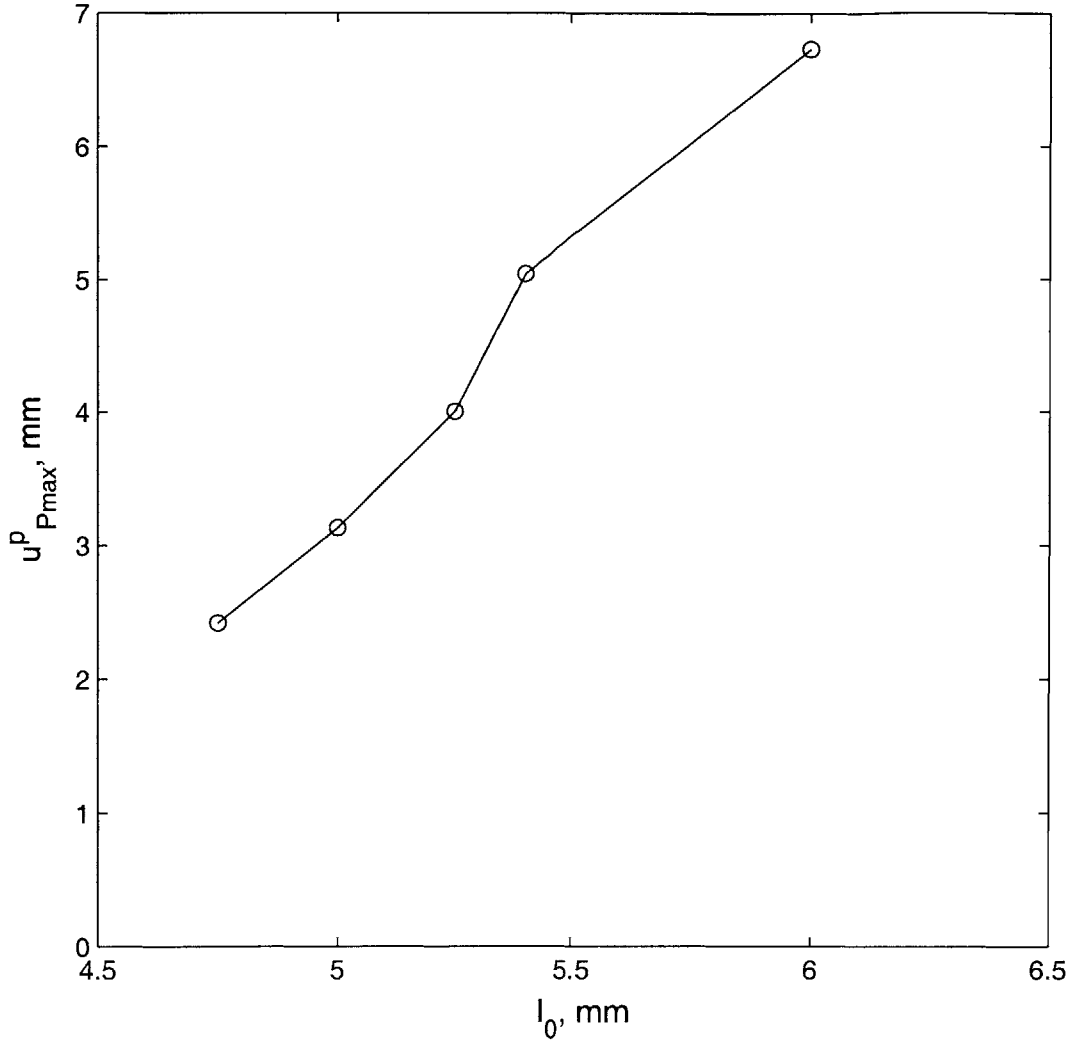

Figure 4-2: Cross-plot of plastic displacement at peak-load, $u^p_{P_{max}}$, vs. initial ligament length, l_0, using values listed in Table 4.1, for back-bend experimental data.

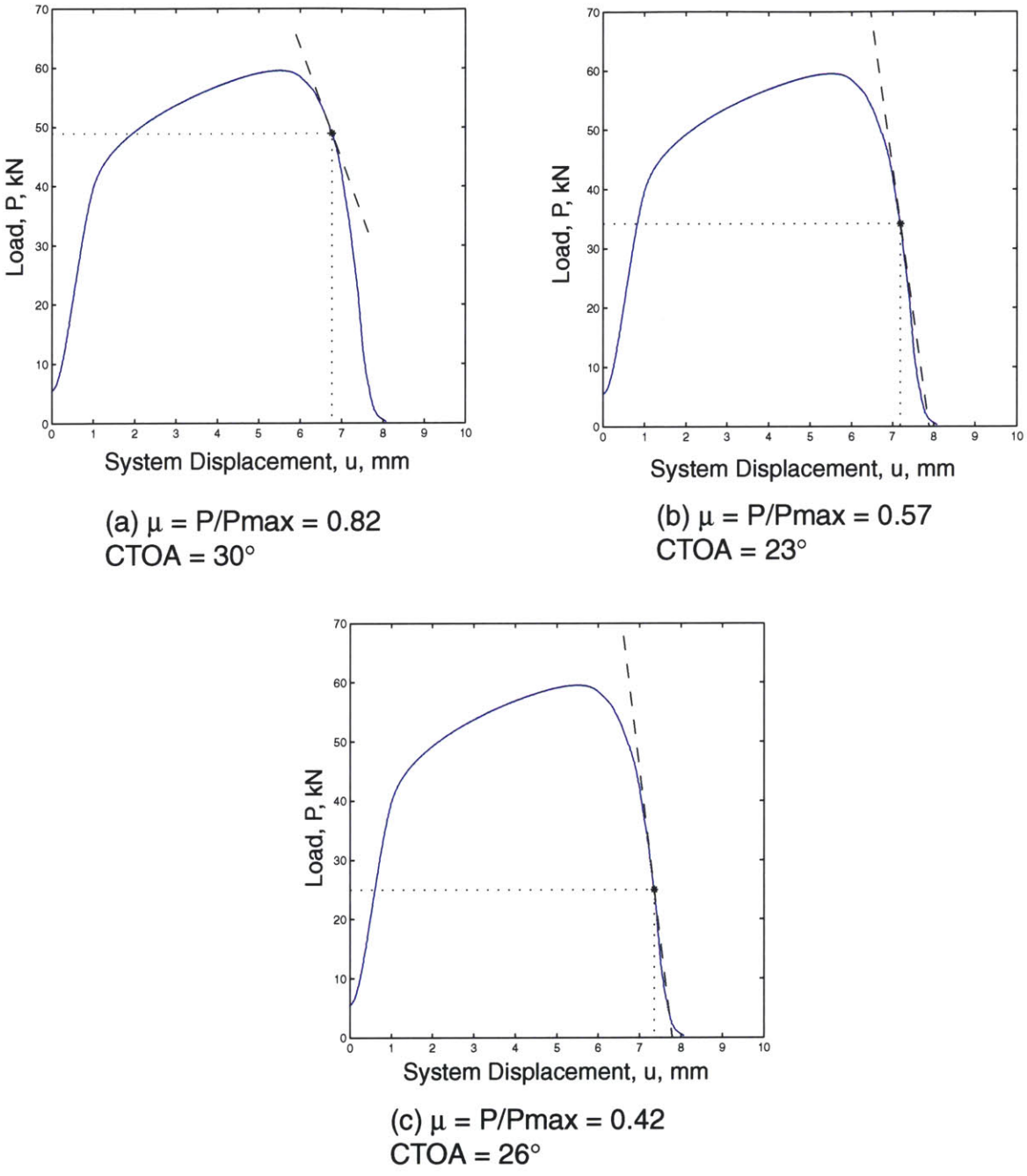

Figure 4-3: Back-bend $CTOA$ calculation from experimental load-displacement curves.

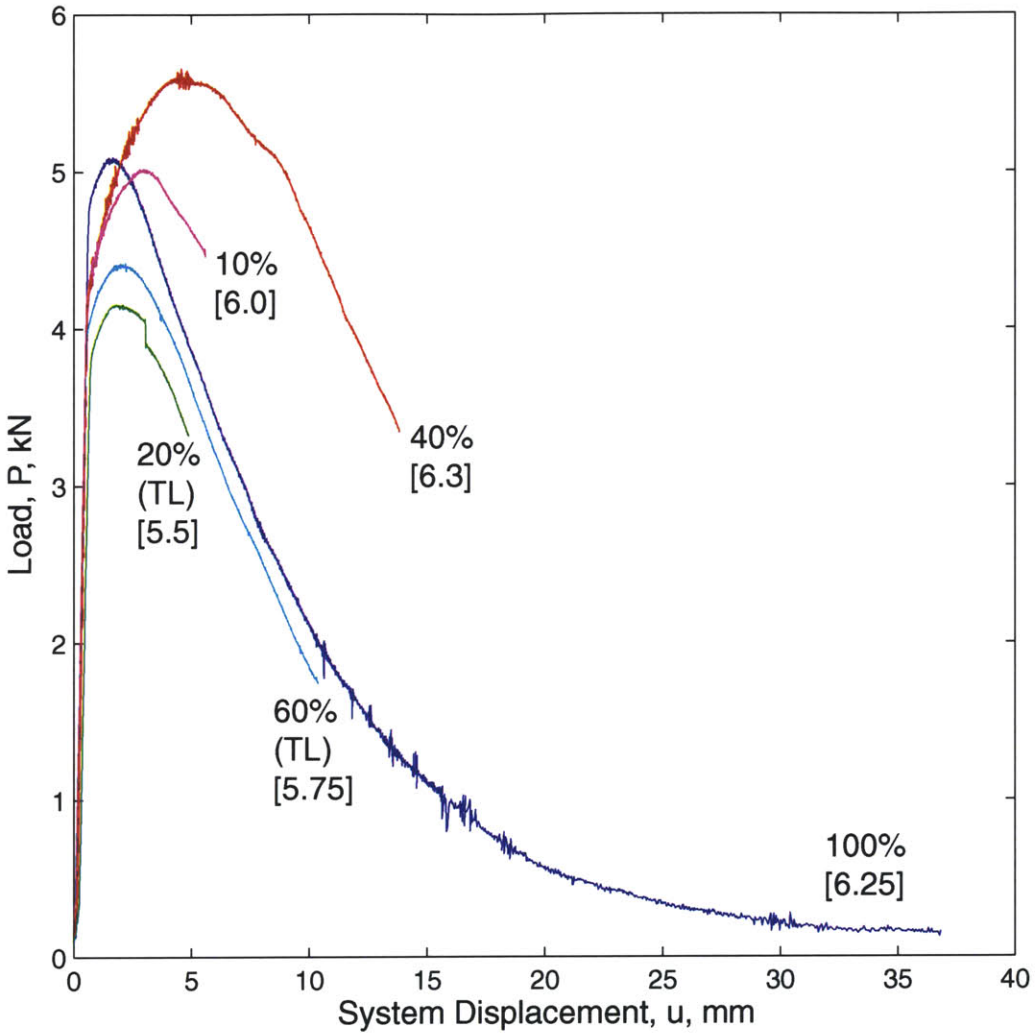

Figure 4-4: Open-bend experimental load-displacement curves. Percentages are post-peak load-drops. Values in square brackets are the initial ligament length, l_0, in mm. TS orientation except as noted.

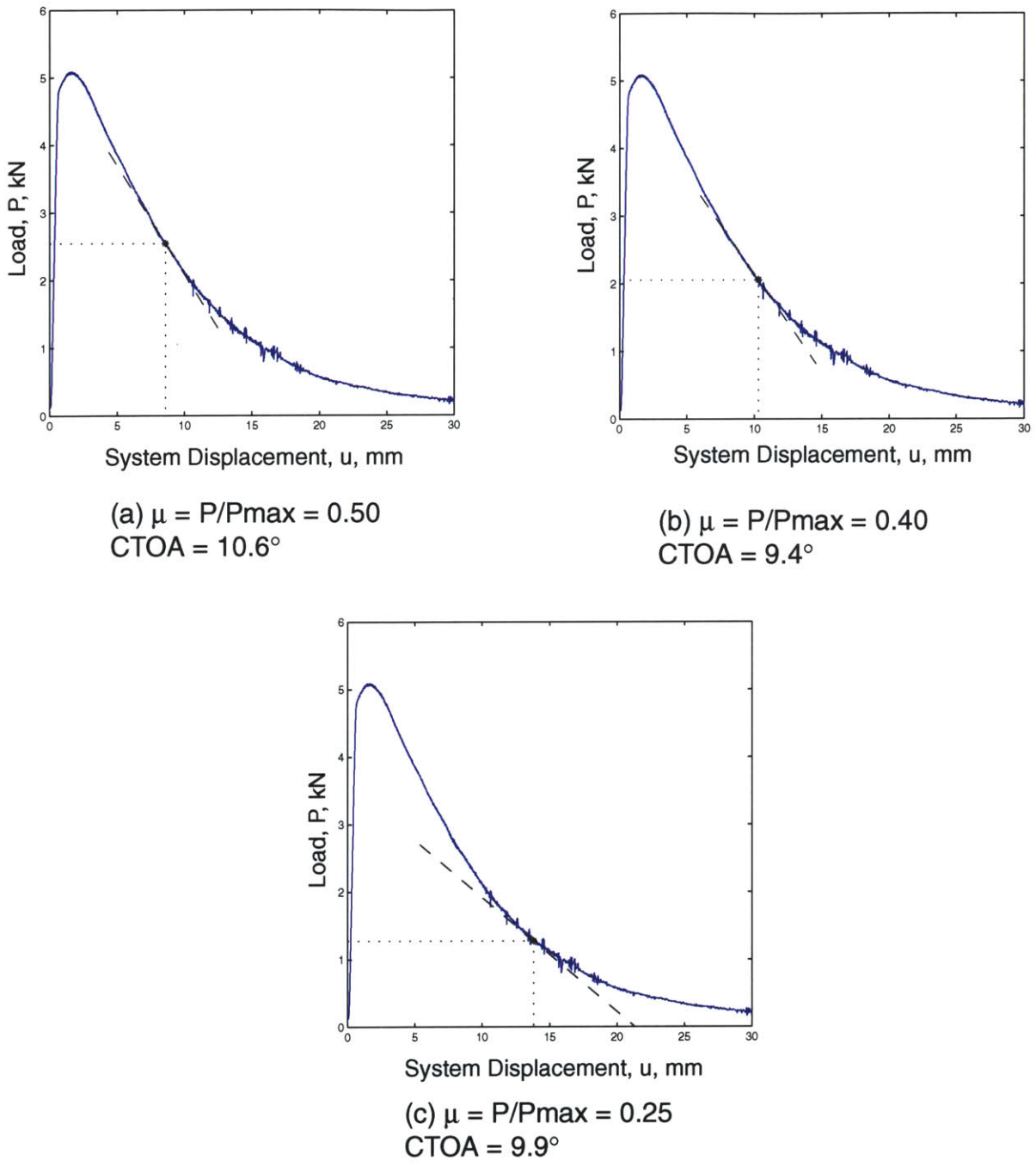

Figure 4-5: Open-bend $CTOA$ calculation from experimental load-displacement curves.

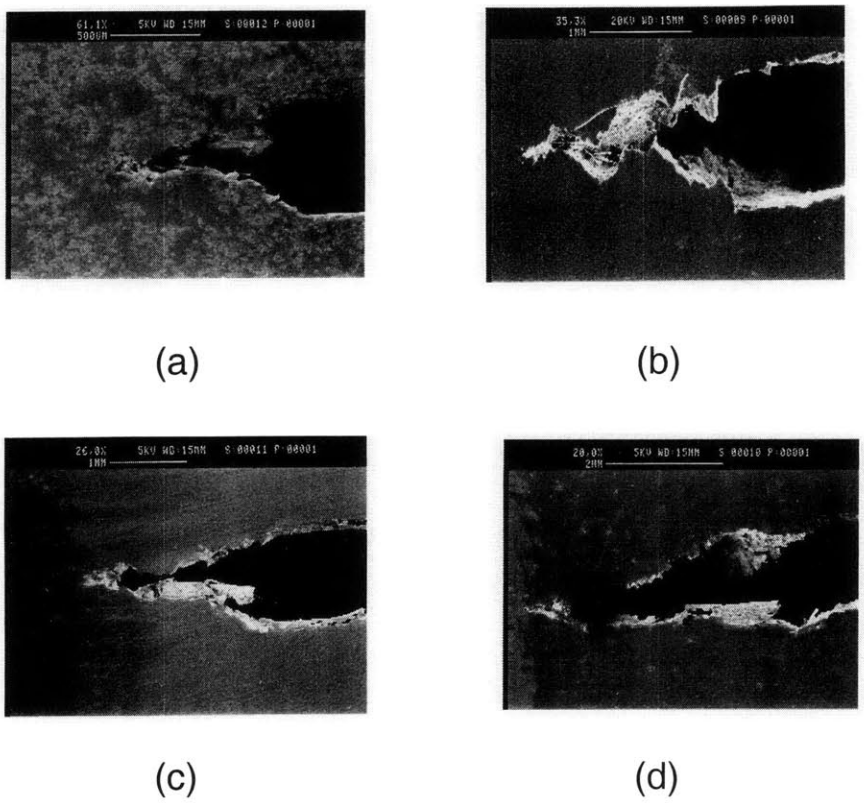

Figure 4-6: Mid-plane crack profiles of unloaded back-bend specimens from Bass [3]. (a) 10% load-drop. (b) 20% load-drop. (c) 40% load-drop. (d) 60% load-drop.

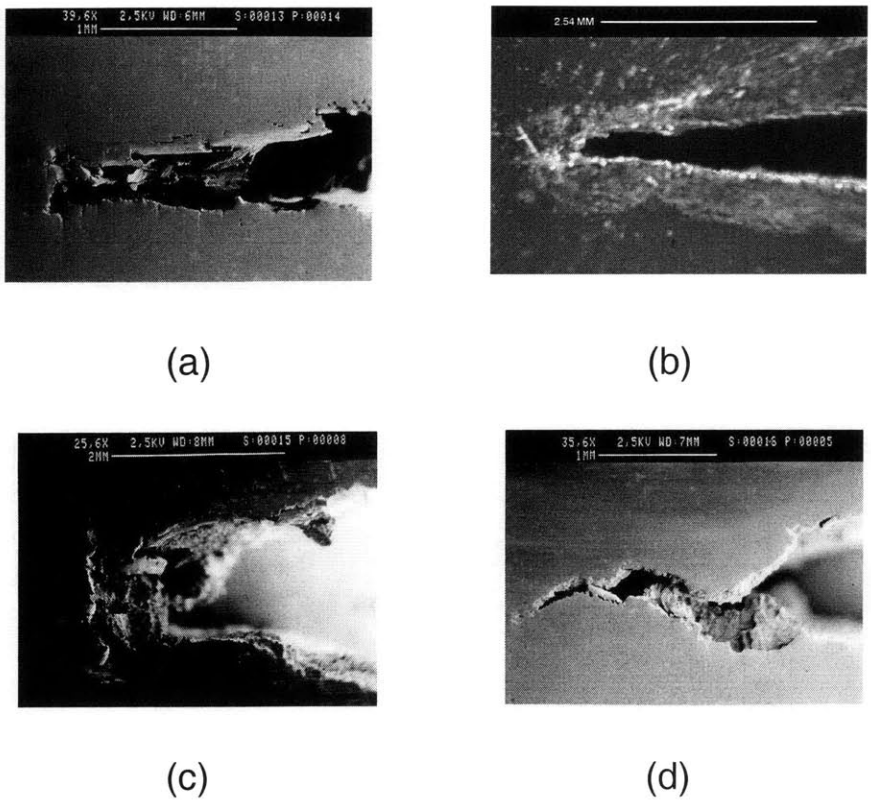

Figure 4-7: Mid-plane crack profiles of unloaded open-bend specimens from Bass [3]. (a) 10% load-drop. (b) 20% load-drop. (c) 40% load-drop. (d) 60% load-drop.

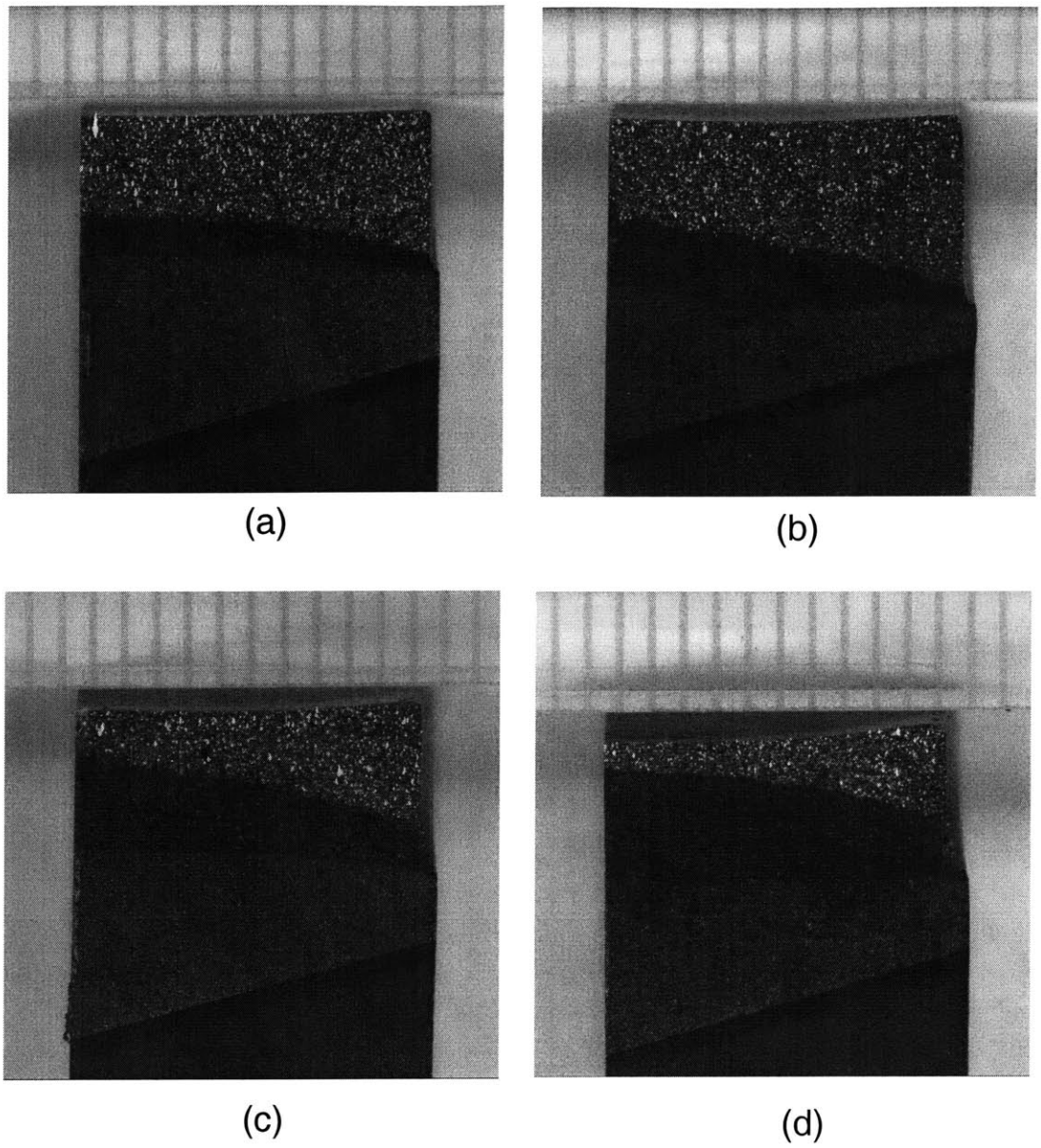

Figure 4-8: Fractographs of approximately one-half of back-bend fracture surfaces from Bass [3]. Left side of each specimen is mid-specimen section plane. Right side is free surface. Each figure shows, from bottom to top, the chevron notch, the fatigue pre-crack, the stable ductile tearing, the final cleavage after cooling in liquid nitrogen, and the drawn-in back surface. Scale divisions at top are 1 mm. (a) 10% load-drop. (b) 20% load-drop. (c) 40% load-drop. (d) 60% load-drop.

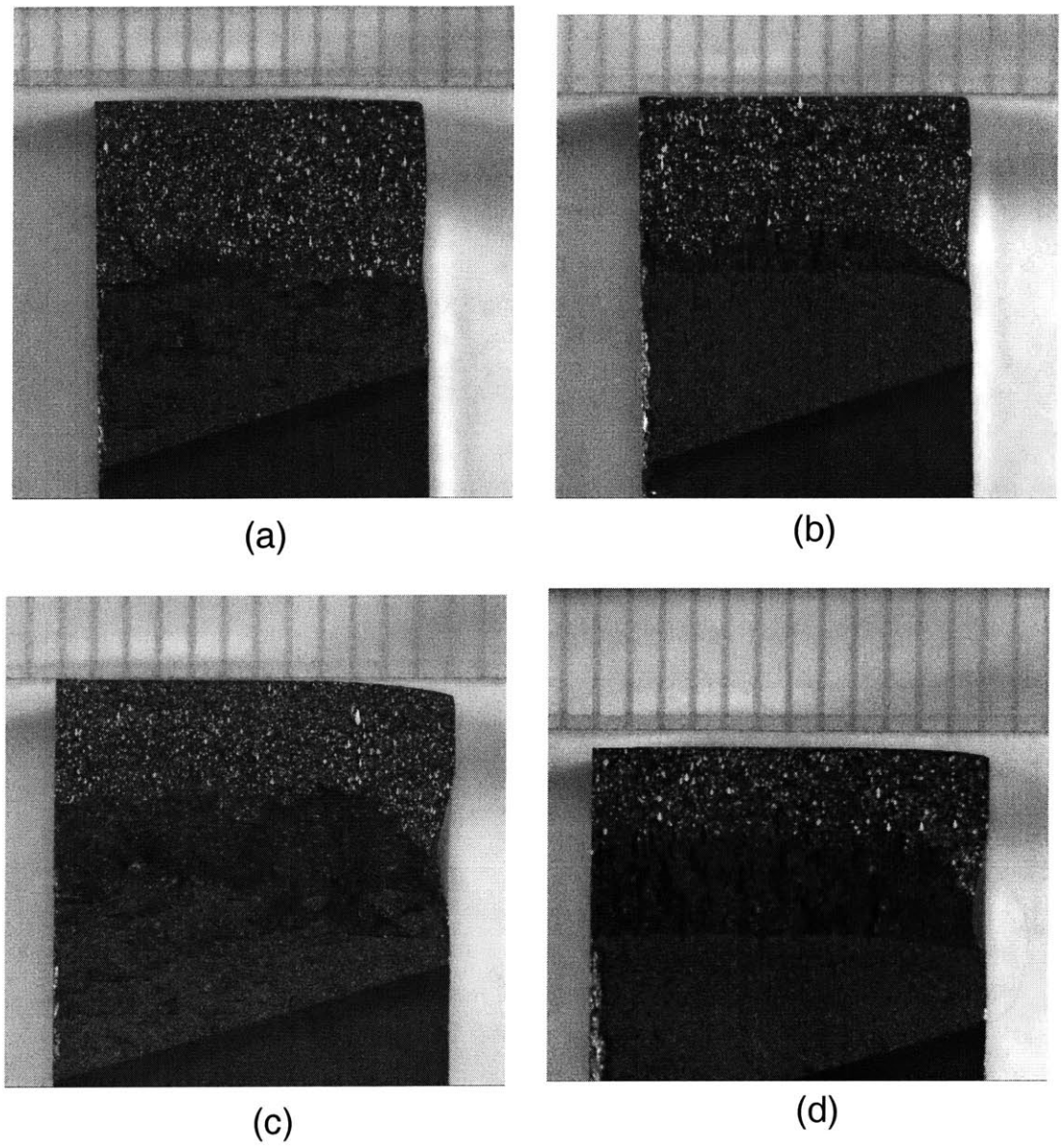

Figure 4-9: Fractographs of approximately one-half of open-bend fracture surfaces from Bass [3]. (Refer to caption of Figure 4-8 for details.) (a) 10% load-drop. (b) 20% load-drop (TL Orientation). (c) 40% load-drop. (d) 60% load-drop (TL Orientation).

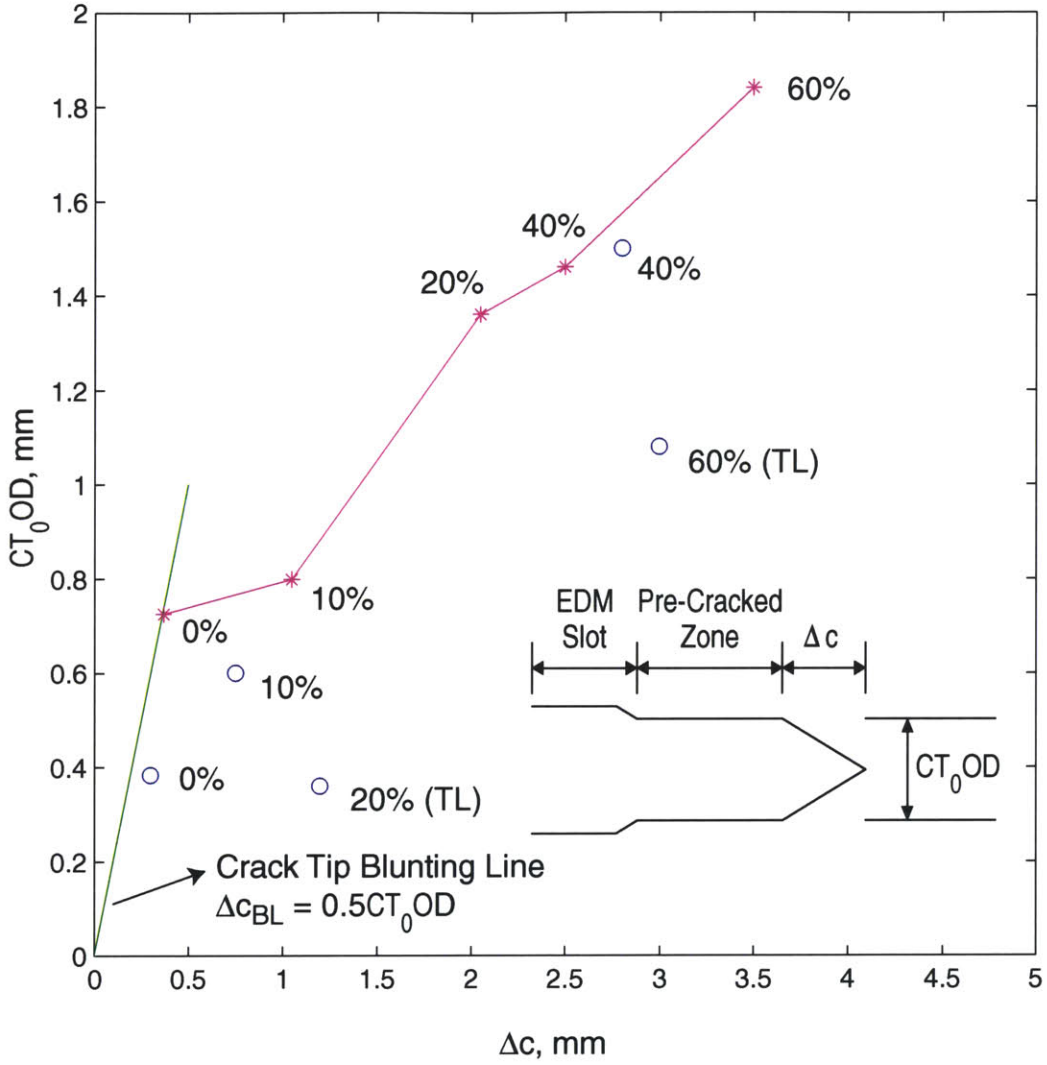

Figure 4-10: Opening displacement of the initial crack-tip, CT_0OD, vs. Δc for back-bend and open-bend specimens. Back-bend data is shown with asterisks, and open-bend data is denoted by circles.

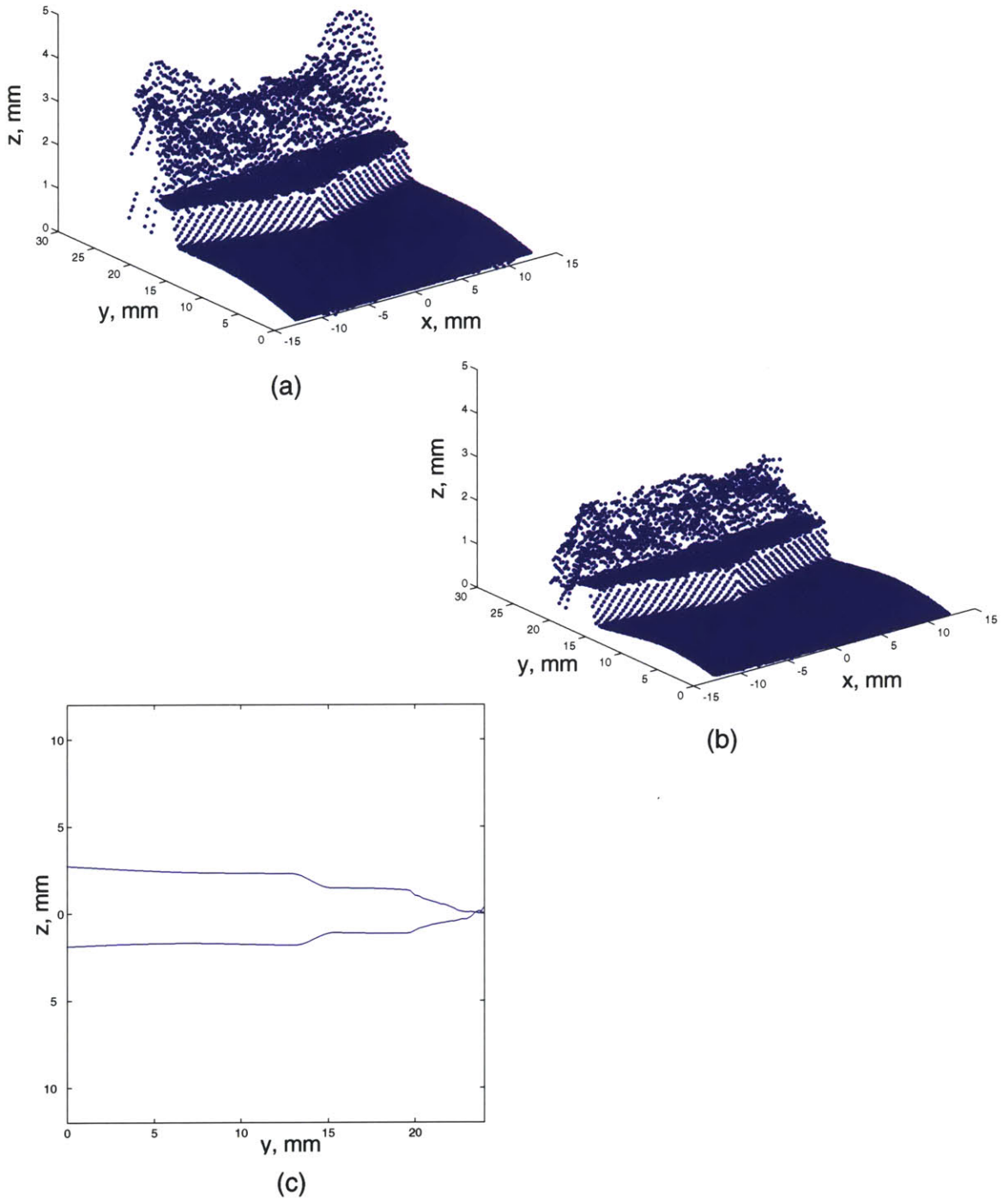

Figure 4-11: (a) and (b) Back-bend fracture surface topographs, 100% load-drop, from Bass [3]. (c) Crack surface profile calculated by averaging over central 10 mm. Z-axis exaggerated by factor of six in (a) and (b).

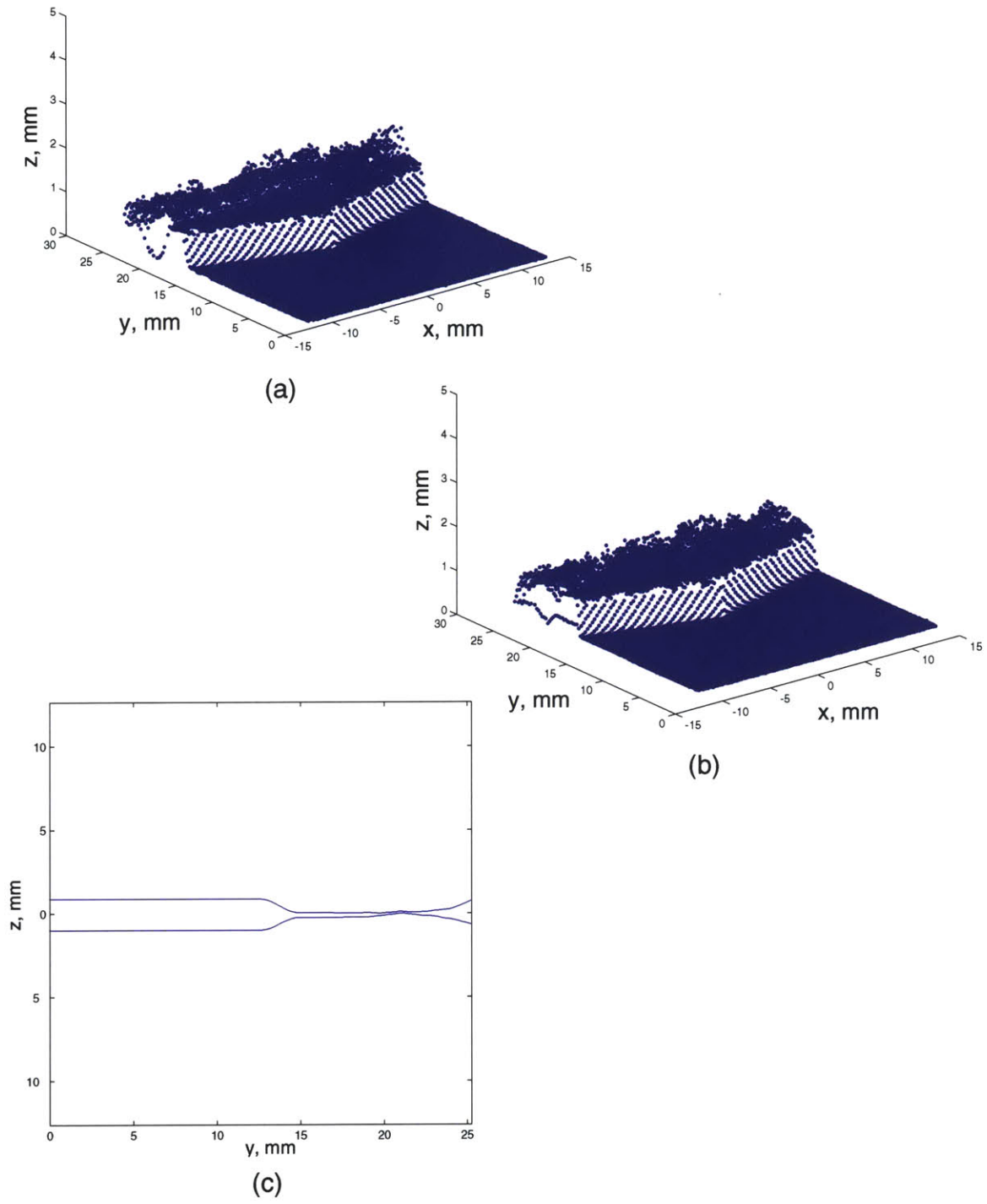

Figure 4-12: (a) and (b) Open-bend fracture surface topographs, 100% load-drop, from Bass [3]. (c) Crack surface profile calculated by averaging over central 10 mm. Z-axis exaggerated by factor of six in (a) and (b).

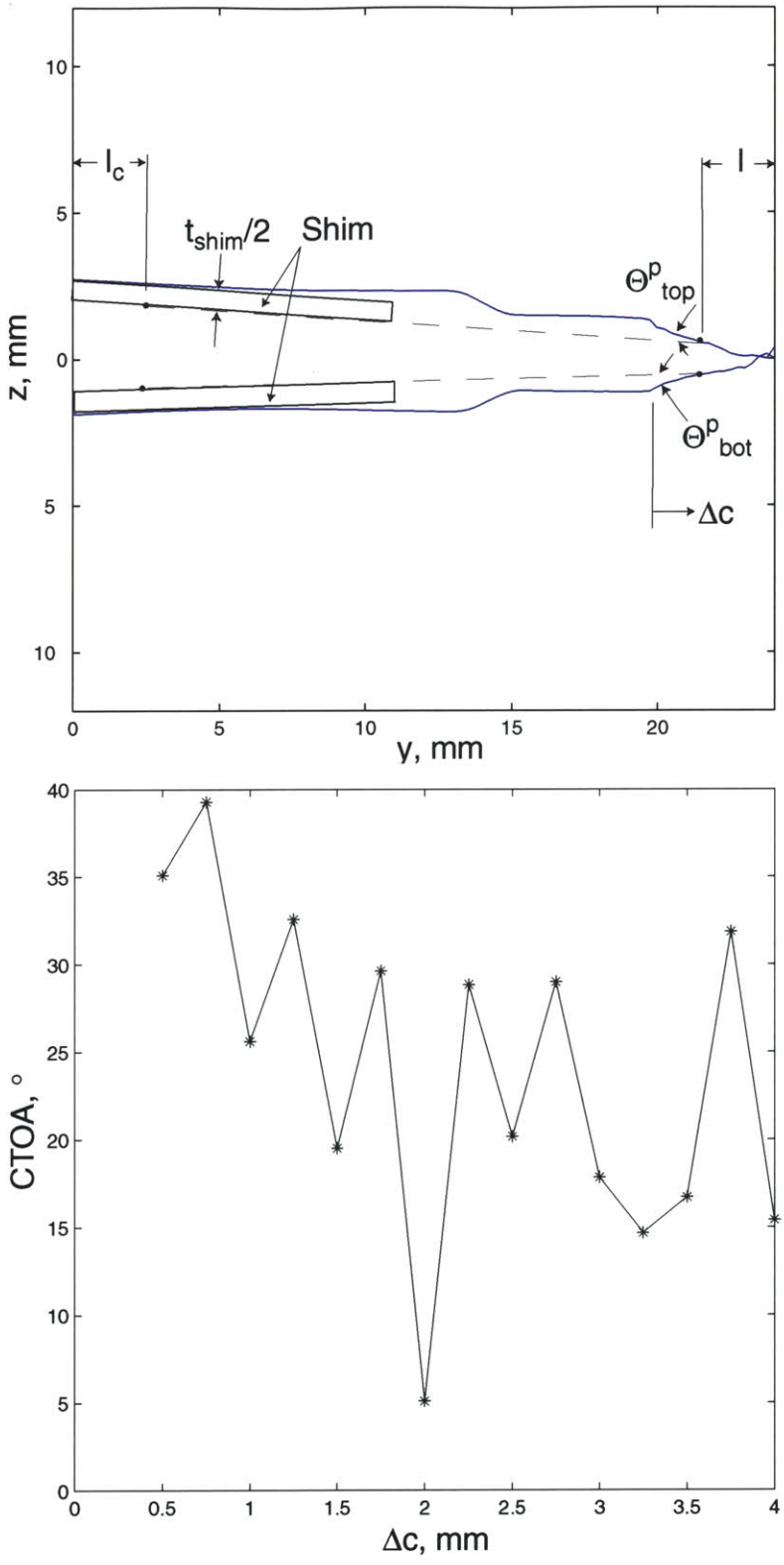

Figure 4-13: (a) Back-bend $CTOA$ calculation from crack surface profile. For illustration purposes only, the shim thickness has been split along its mid-plane to identify the pivot point. (b) Back-bend $CTOA$ vs. Δc from crack surface profile.

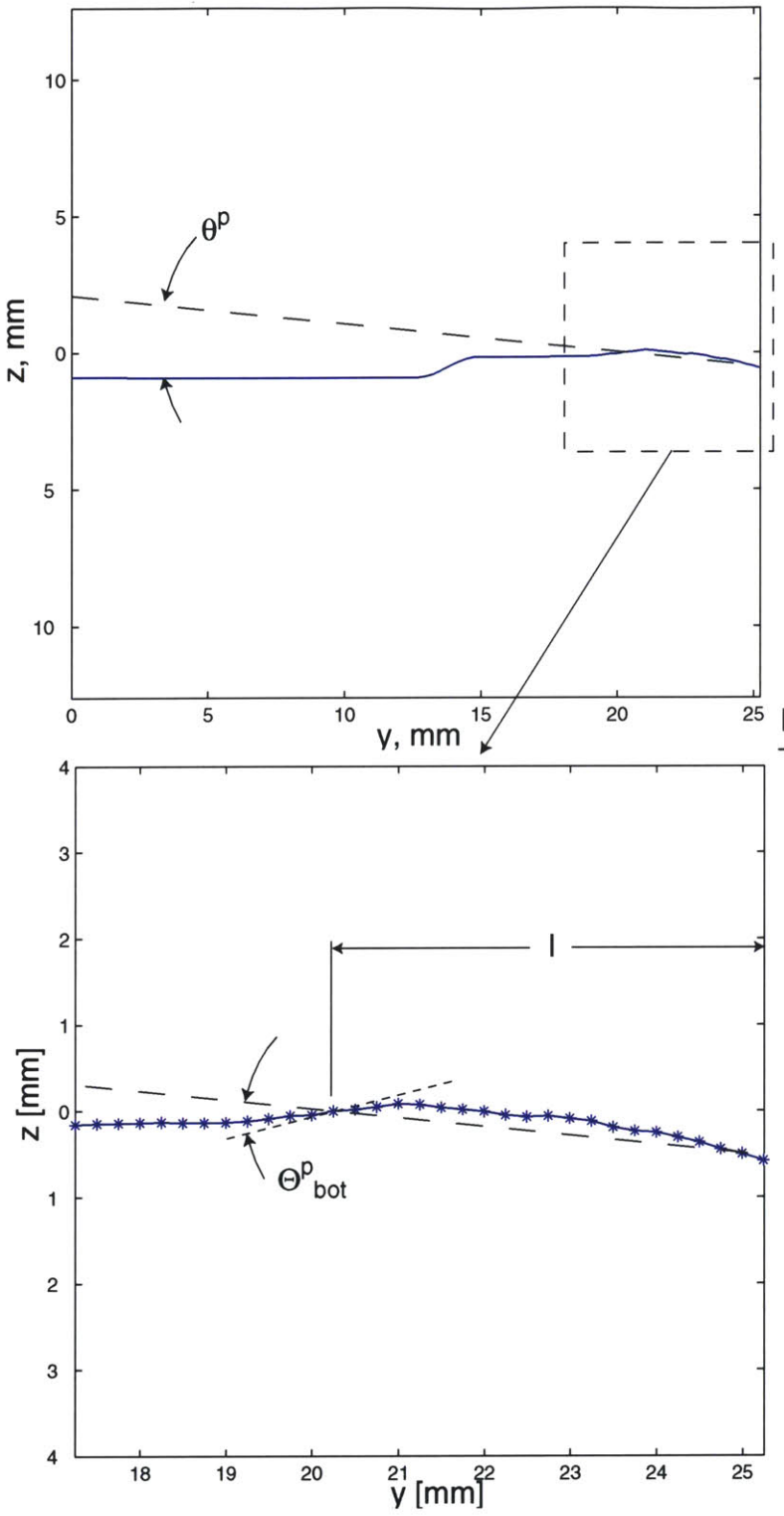

l (mm)	P/P_{max}	θ^p(°)	CTOA (°)
5.0	0.64	5.9	13
4.0	0.41	9.1	15
3.0	0.23	13.1	17

Figure 4-14: Open-bend $CTOA$ calculation from crack surface profile. Local ligament length l defines post-peak load, which then provides half the relative rotation, θ^p. The contribution to $CTOA$ of the lower surface is indicated as Θ^p_{bot}; an analogous procedure is applied to the other profile to determine the remaining contribution, Θ^p_{top}.

Post-peak load-drop (%)	l_0 (mm)	$P_{max}/P_{lim}(l_0)$ [2.6] & [4.3]	σ_{flow} at peak [2.6] & [4.3] (MPa)	$u^p_{(P_{max})}$ (mm)	$CTOD_i$ [4.1] & [4.4] (mm)
Back-bend					
10	4.75	1.02	571	2.42	1.2
20	6.0	1.09	607	6.73	2.8
40	5.0	1.11	622	3.13	1.5
60	5.4	1.07	598	5.04	2.3
100	5.25	1.09	610	4.00	1.9
Open-bend					
10	6.0	1.08	494	2.29	0.16
20*	5.5	1.07	487	1.26	0.08
40	6.3	1.11	505	3.82	0.28
60*	5.75	1.04	474	1.63	0.11
100	6.25	1.01	462	0.98	0.07

Table 4.1: Experimental load-displacement results for back-bend and open-bend tests. * indicates incorrect TL crack orientation. Numbers in brackets refer to equation numbers used in calculations.

	$\mu = P/P_{max}$	$c(\mu)$ [2.6] (mm)	dP/du (kN/mm)	dP/du^p [A.13] (kN/mm)	$c_{,u}$ [4.2]	$CTOA$ [2.4] (°)
Figure 4-3(a)	0.82	21.3	-19.1	-12.6	1.95	29.8
Figure 4-3(b)	0.57	22.7	-49.4	-21.4	2.82	22.6
Figure 4-3(c)	0.42	23.5	-57.4	-22.5	2.41	25.5

Table 4.2: Calculation of $CTOA$ from experimental load-displacement results for back-bend tests. Numbers in brackets refer to equation numbers used in calculations. With $\lambda_0 = l_0/t$, $l_0 = 5.25$ mm, $t = 25.4$ mm, $s = 63.5$ mm, $\theta_s = 45°$, $P_{max} = 59.57$ kN, and $(C_m + C_{spec}) = 0.025$ mm/kN.

	$\mu = P/P_{max}$	dP/du (kN/mm)	dP/du^p [A.13] (kN/mm)	$c_{,u}$ [4.5]	$CTOA$ [2.4] (°)
Figure 4-5(a)	0.50	-0.321	-0.310	9.94	10.6
Figure 4-5(b)	0.40	-0.291	-0.281	11.2	9.4
Figure 4-5(c)	0.25	-0.169	-0.166	10.7	9.9

Table 4.3: Calculation of $CTOA$ from experimental load-displacement results for open-bend tests. Numbers in brackets refer to equation numbers used in calculations. With $s = 63.5$ mm, $\theta_s = 72°$, $P_{max} = 5.093$ kN, and and $(C_m + C_{spec}) = 0.12$ mm/kN.

Post-peak load-drop (%)	l_0 (mm)	Δc_{cal} [2.6] & [4.3] (mm)	Δc_{obs} (mm)
Back-bend			
10	4.75	0.6	1.0
20	6.0	1.6	2.0
40	5.0	2.3	2.5
60	5.4	3.6	3.5
100	5.25	-	-
Open-bend			
10	6.0	0.3	0.8
20*	5.5	0.6	1.2
40	6.3	1.4	2.8
60*	5.75	2.1	3.0
100	6.25	-	-

Table 4.4: Experimental fractographic results for back-bend and open-bend tests. * indicates incorrect TL crack orientation. Numbers in brackets refer to equation numbers used in calculations.

Chapter 5

Finite Element Results

5.1 2-D Plane Strain

Finite element analysis was first done in the 2-D plane strain idealization, as shown in Figure 3-5, with the isotropic matrix strain-hardening of Figure 3-4. ABAQUS/Explicit was used, so as to model crack growth via element deletion, a capability not available in ABAQUS/Standard [24]. Three different ways of using the GTN model with the current given mesh size were considered. The first case restricted the GTN model with element failure to a single layer of interface elements next to the specimen mid-plane, while all other elements were assigned a material model of classical (non-porous, non-dilating), strain-hardening, metal plasticity as shown in Figure 5-1(a). This type of model has been previously used by Shih, et al. [21] for crack growth in compact tensile (bend) specimens. Here, the calculated load-displacement curves showed an overly steep drop-off as shown in Figure 5-2, as the crack started to grow, for the adopted GTN parameters and mesh size. Modifications to the model parameters and mesh (as demonstrated in Figures 5-3 and 5-4) did not significantly change this result, and therefore this modeling approach was deemed unsatisfactory. In the second case, the GTN porous plasticity model was assigned throughout the mesh. Again, in only one layer of interface elements next to the center-plane was the GTN model augmented with element failure and deletion; in the remainder of the mesh, no element failure/deletion was implemented as shown in Figure 5-1(b). The load-displacement

curve for this distribution shows a more gradual load-drop, when compared to the previous case as shown in Figure 5-2. Finally, the GTN plasticity with element deletion was used throughout the mesh to verify the localization of the crack growth, as shown in Figure 5-1(c). The load-displacement for this case showed no change from the previous case; although the elements were free to fail anywhere in the mesh, they failed only in the first layer of interface elements next to the center-plane. Based on these simulations, the modeling assumptions of the second case (Figure 5-1(b))were adopted for all subsequent runs.

Figure 5-5 shows calculated plane strain load-displacement curves of back-bend loading, for initial ligament lengths, $l_0 = 5.0$, 5.5 and 6.0 mm. As seen experimentally, small changes in initial ligament length produce large changes in both peak load and displacement to peak. Figure 5-6 shows the calculated plane strain load-displacement curves of open-bending, for initial ligament lengths, $l_0 = 5.0$ and 6.0 mm. The large difference in the peak load is due to the second-order dependence of the limit load on the ligament size.

The deformed crack profiles at initiation give the $CTOD_i$ from the finite element results as $\sim$ 0.4 mm for the back-bend as opposed to $\sim$ 0.2 mm for the open-bend. Figures 5-7(a) and (b) show the crack profiles for the back-bend and open-bend tests, at equivalent points in their respective ductile tearing regimes ($\Delta l/l_0 = -0.25$). The contour plots of the equivalent plastic strains in the figures bear strong likeness to the respective slip line fields, although they differ slightly due to material strain-hardening. The deformed crack profiles also show a (larger) $CTOA$ of $\sim$ 34° for back-bending, compared to a (smaller) $CTOA$ of $\sim$ 17° for open-bending. Crack initiation in the plane strain simulations occurs at displacements $\sim$ 10% less than peak load displacement, which is consistent with the assumption made in Chapter 4.

Figures 5-8 and 5-9 show the equivalent plastic strain and normal stress contour plots at four stages of crack-growth in the back-bend simulations. As noted in Chapter 2 and detailed in Appendix A.1, the back-bend loading causes pre-strain in the ligament ahead of the crack growth. This is verified in Figure 5-10, which plots plane strain calculations of the distributions of ε^p_{eq}, along the center-planes of the back-bend

and extension-loaded face-crack specimens, at three levels of cracking. The plots indicate substantially higher pre-strains in the ligament ahead of the crack growth in back-bending than in the face-cracked tensile specimen.

5.2 3-Dimensional runs

The 3-D finite element back-bend load-displacement curves are shown in Figure 5-11 for initial ligament lengths, l_0 = 4.75, 5.0, 5.25 and 6.0 mm. The l_0-values (in mm) which were measured from the fractographs are indicated within square brackets for the experimental data. The experimental curves are in excellent agreement with the finite element simulations, for the current set of GTN model parameters and mesh. The 3-D simulations are also in good agreement with the 2-D simulations, shown in Figure 5-5. Due to plane strain conditions, the 2-D runs give peak loads which are typically 10% higher at a given l_0. The plastic displacement, u^p, at peak load is lower in plane strain than in 3-D.

The 3-D finite element open-bend load-displacement curves are shown in Figure 5-12 for initial ligament lengths, l_0 = 5.5 and 6.0 mm. The calculated results agree broadly with the experimental curves, while not matching them exactly. One possible reason for this is use the GTN model, with a fixed set of parameters modeling void growth and coalescence under two dramatically different levels of triaxiality and resulting strains to failure. The GTN model was originally devised [17] for predominantly spherical void growth corresponding to a high-triaxiality environment, and does not account for prominent void shape changes encountered in large deformation under low-triaxiality. The GTN parameters fit for the low-triaxiality back-bend loading, in which large strains are required to generate a given void volume fraction of (non-spherical) voids, would not necessarily match with the parameters that one would use for the high-triaxiality open-bend loading, which fails locally at smaller strains, and with more equi-axed cavities. Recent work has extended the GTN model to incorporate void shape effects, as was considered by Pardoen, et al. [25], and Gologanu, et al [26]. Other models originating from the void growth analysis of McClintock

[27] have also considered growth of non-spherical voids, such as the Rousselier model [28].

Experimental and calculated fracture surface views for the back-bend case are shown in Figure 5-13. Figure 5-13(a) shows the experimental fractograph of a back-bend specimen loaded to 40% load-drop, and Figure 5-13(b) shows the 3-D finite element simulation fracture surface view, for a specimen with $l_0 = 5.0$ mm, loaded to 37% load-drop. The tunneled crack shape shows appreciable curvature over most of its length, and some of this effect is captured in the simulation. Corresponding views for the open-bend case are shown in Figure 5-14. Figure 5-14(a) shows the experimental fractograph of an open-bend specimen loaded to 40% load-drop, and Figure 5-14(b) shows a simulation fracture surface view for a specimen with $l_0 = 6.0$ mm, loaded to 36% load-drop. In open-bending, the tunneling is less pronounced, and crack-length variation is concentrated near the low-triaxiality traction-free surface. The finite element simulation captures this effect, as seen in Figure 5-14(b).

Similar to the 2-D simulations, the mid-plane 3-D crack profiles for the back-bend and open-bend tests give a $CTOD_i$ of ~ 0.4 mm for the back-bend as compared to ~ 0.2 mm for the open-bend. The 3-D simulations give a larger $CTOA$ of $\sim 30^\circ$ in the back-bend case, compared to a $CTOA$ of $\sim 15^\circ$ for the open-bend.

All the finite element runs discussed used the fixed set of GTN parameters shown in Table 3.2, which were chosen by matching the experimental back-bend curves to 3-D finite elements runs. The chosen parameters are within the range of values for typical steels [24], [29]. A fixed element thickness size, $t_{el} = 0.12$ mm, was used in the interface layer of elements ahead of the crack-tip which incorporated the GTN model with element failure and deletion. The void nucleation parameters were chosen based on this element thickness size in the 3-D simulations. If this element size is reduced, at fixed GTN parameters, the computed load-displacement changes, giving a lower $CTOD_i$ and no change in $CTOA$. Thus, chosen values of the material model parameters have to be adjusted with variations in element size in order to match the experimental load-displacement data.

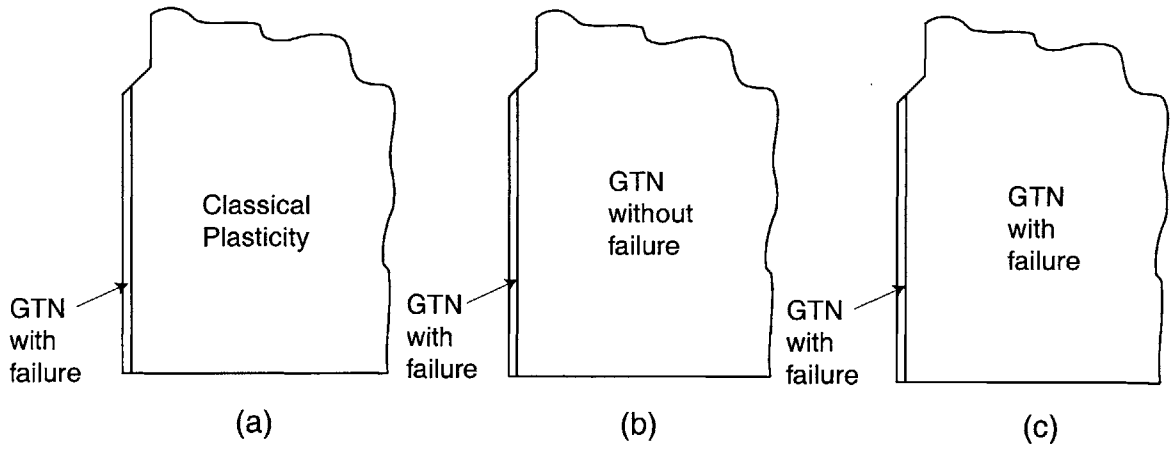

Figure 5-1: GTN model distributions in finite element mesh. (a) With the GTN model restricted to single layer of interface elements next to the specimen mid-plane. (b) With the GTN model assigned throughout the mesh; single layer of interface elements next to the specimen mid-plane were allowed element deletion. (c) With the GTN model allowing element deletion throughout the mesh.

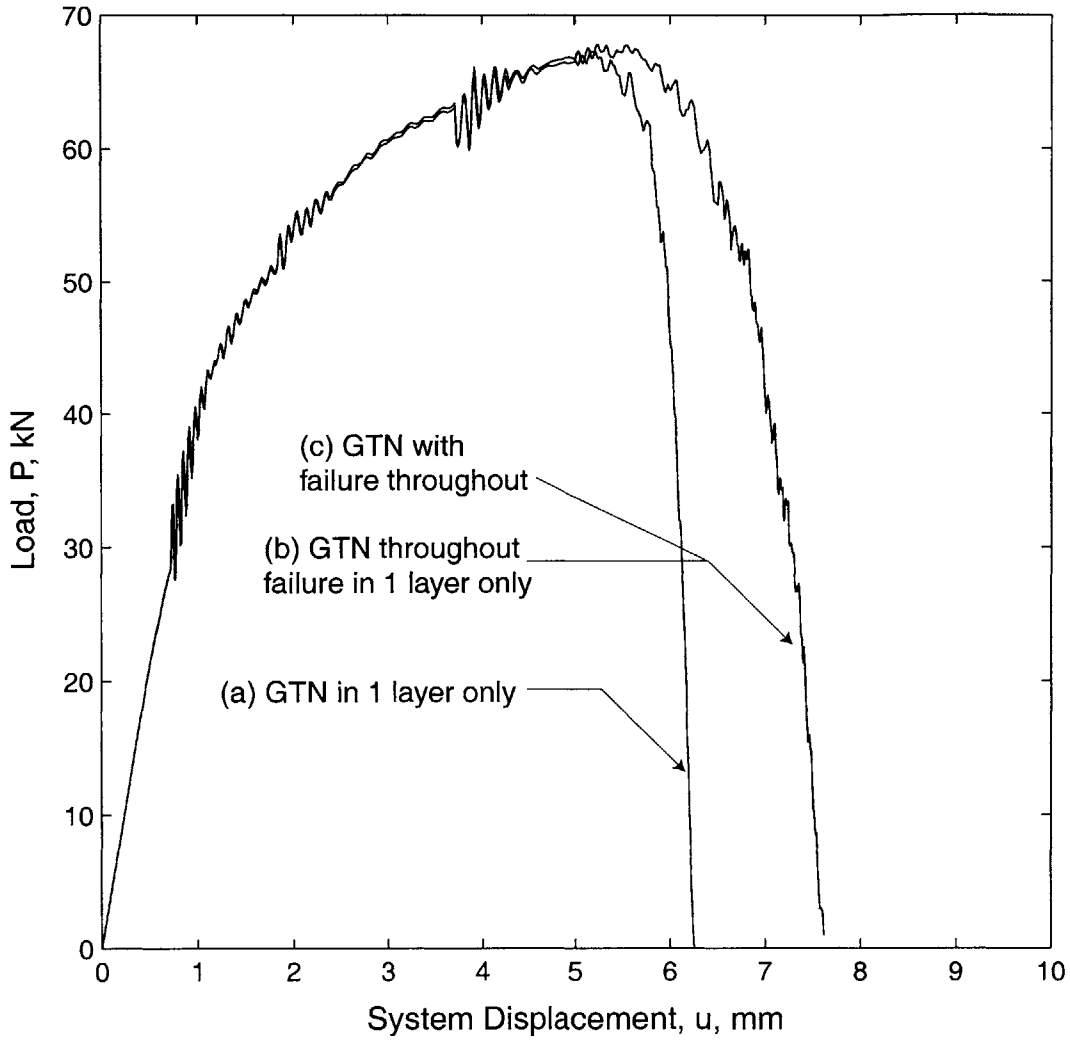

Figure 5-2: Back-bend load-displacement curves for 2-D plane strain finite element simulations with three different GTN model distributions (a), (b) and (c) as defined in Figure 5-1; $l_0 = 6.0$ mm.

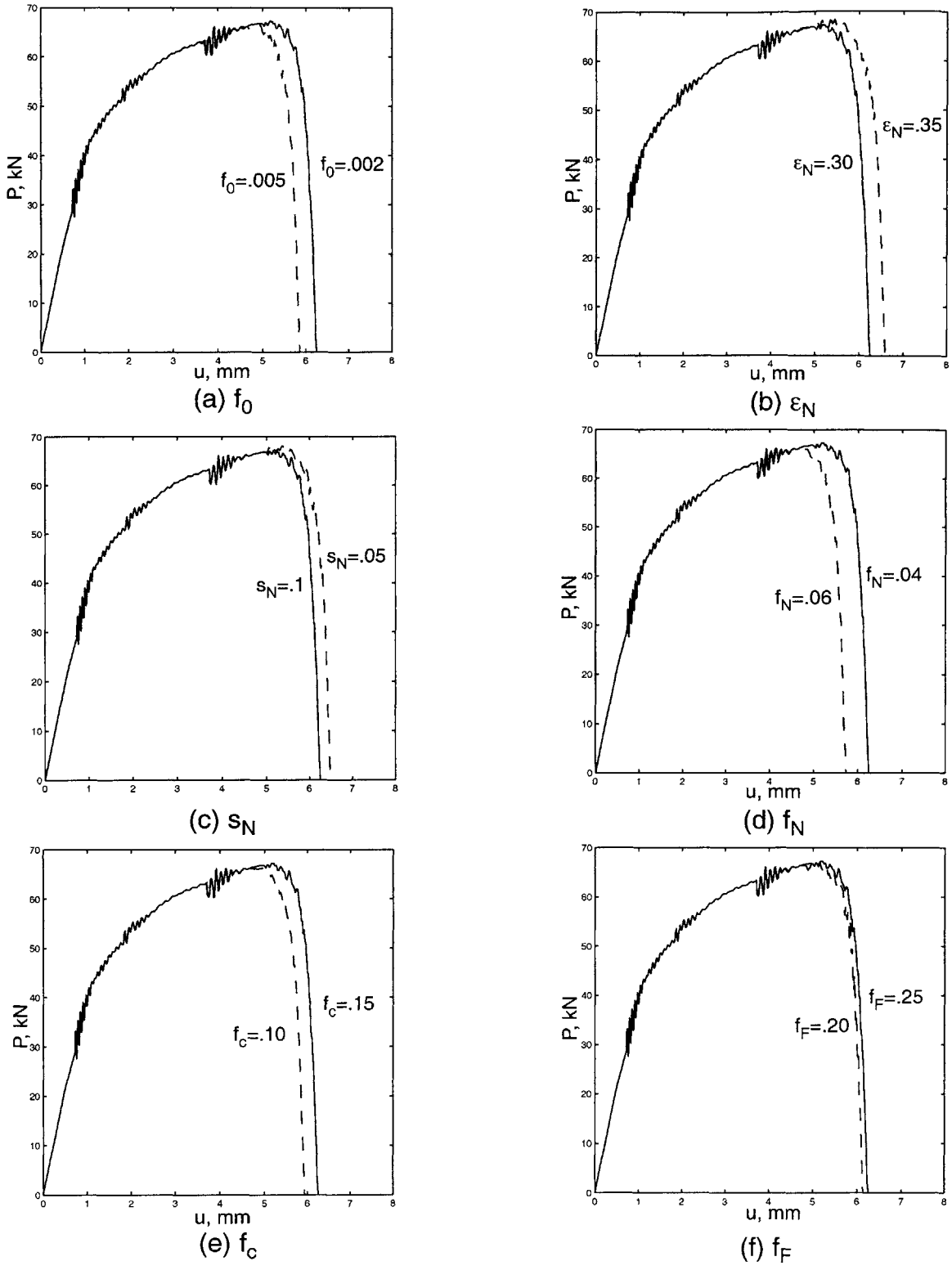

Figure 5-3: Back-bend load-displacement curves showing effect of changing GTN model parameters, f_0, ϵ_N, s_N, f_N, f_c and f_F. With the GTN model restricted to single layer of interface elements next to the specimen mid-plane as in Figure 5-1(a); $l_0 = 6.0$ mm.

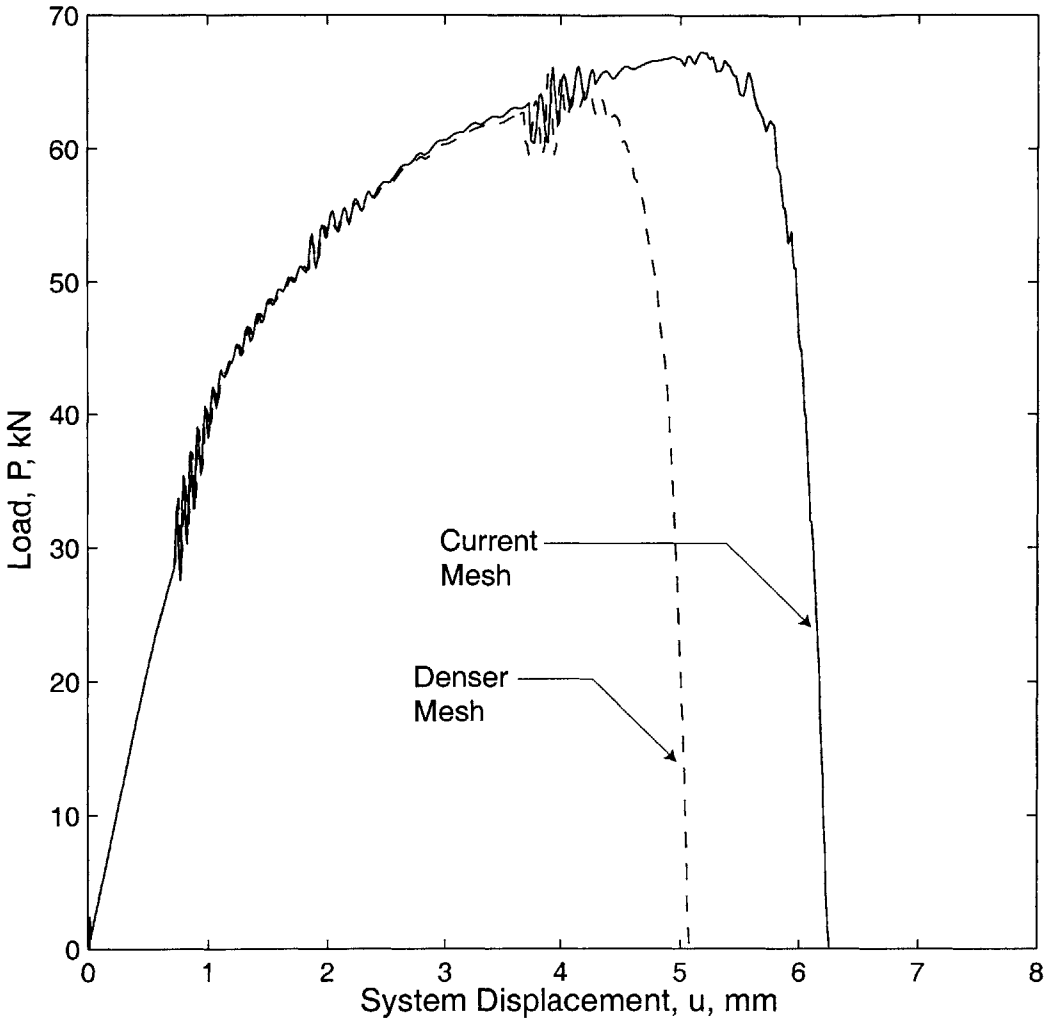

Figure 5-4: Back-bend load-displacement curves showing effect of changing mesh size. (a) Current mesh with l_{el} =.24 mm. (b) Denser mesh with l_{el} =.12 mm. With the GTN model restricted to single layer of interface elements next to the specimen mid-plane as in Figure 5-1(a); $l_0 = 6.0$ mm.

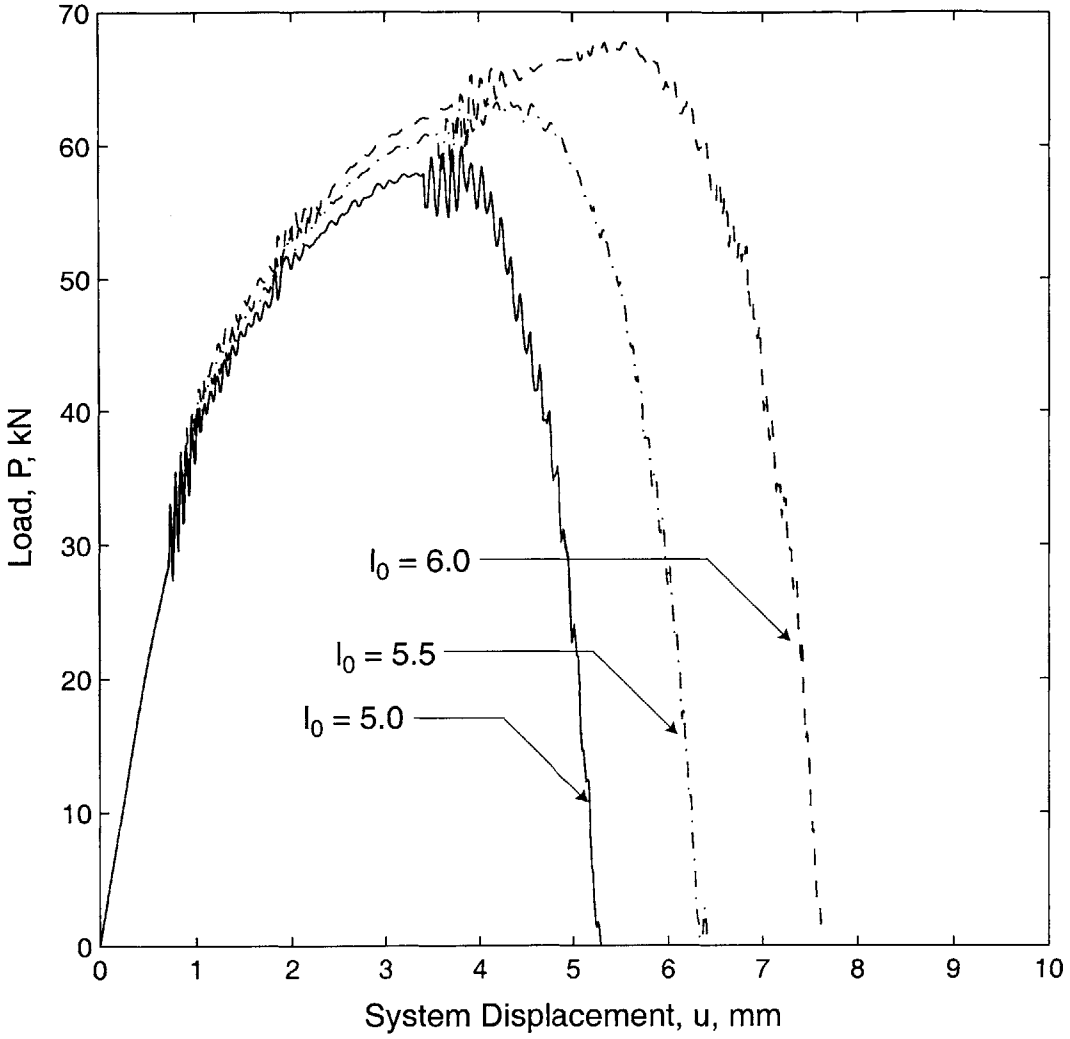

Figure 5-5: Back-bend load-displacement curves for 2-D plane strain finite element runs with different initial ligament lengths, l_0, in mm.

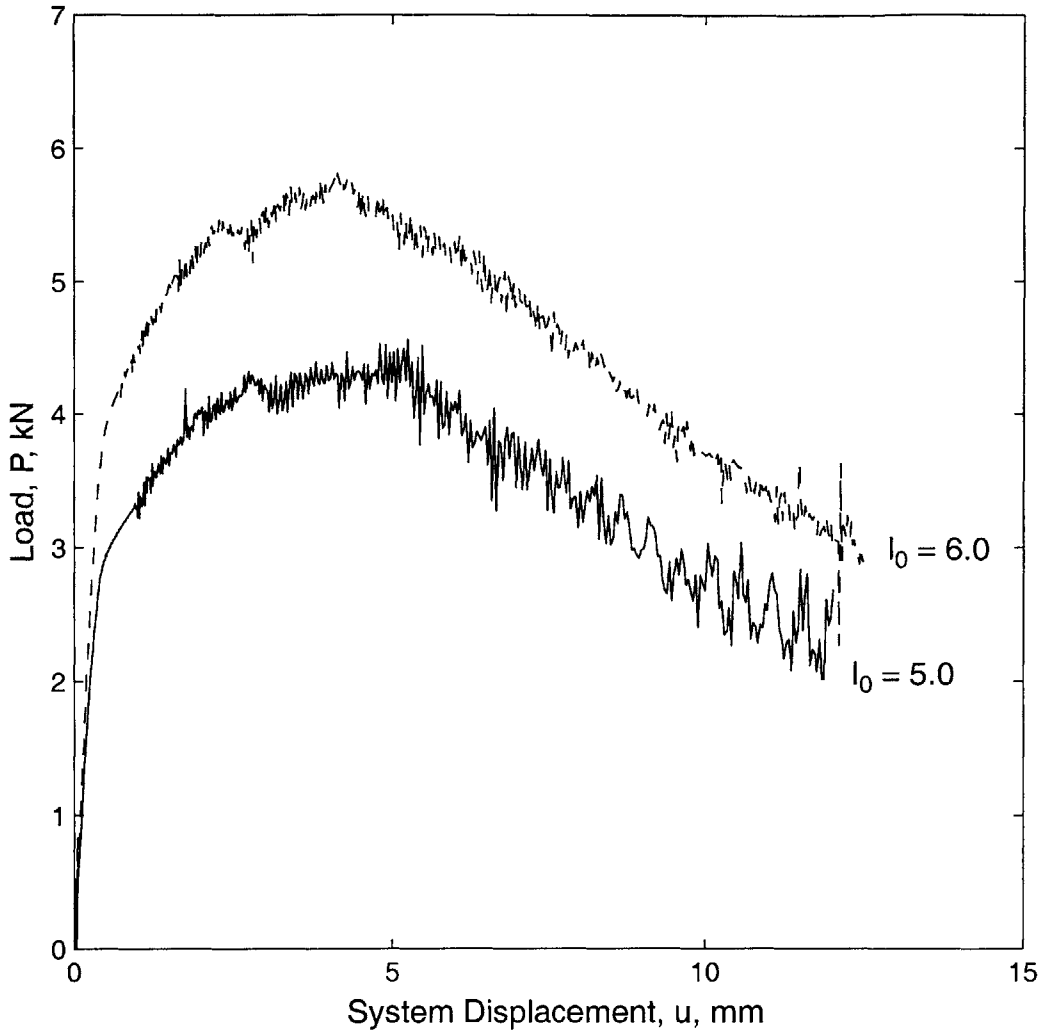

Figure 5-6: Open-bend load-displacement curves for 2-D plane strain finite element runs with different initial ligament lengths, l_0, in mm.

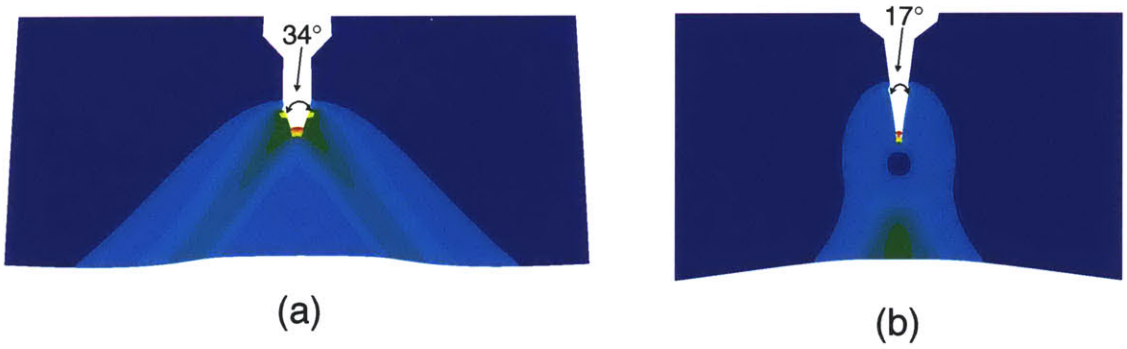

Figure 5-7: Crack profiles from 2-D plane strain finite element runs. (a) Back-bend, $\Delta l/l_0 = -0.25$, $l_0 = 6.0$ mm. (b) Open-bend, $\Delta l/l_0 = -0.25$, $l_0 = 6.0$ mm. Contour plots show equivalent plastic strains.

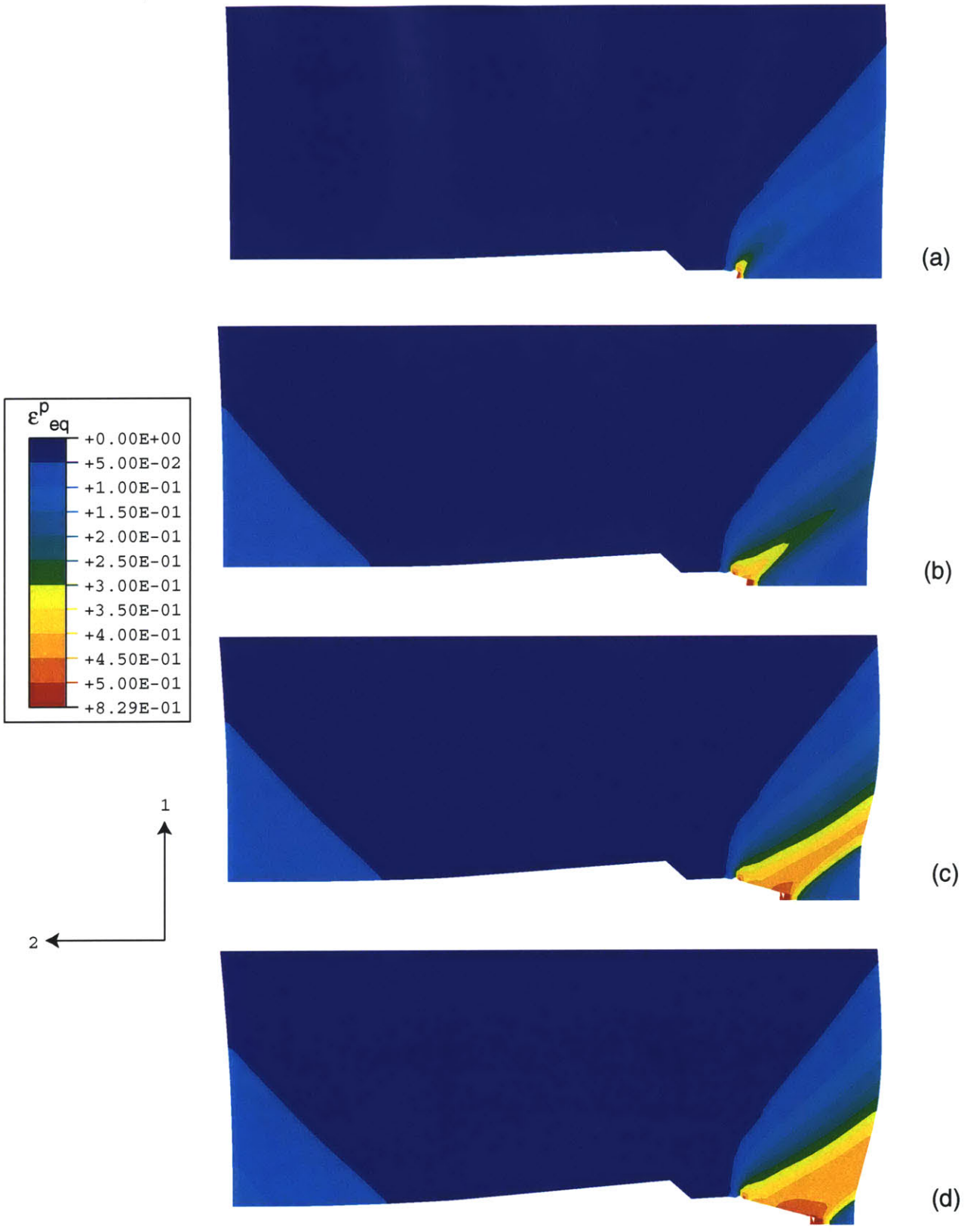

Figure 5-8: Equivalent plastic strain contour plots of one-half specimens near symmetry line for plane strain back-bending simulations; $l_0 = 6.0$ mm. (a) $\Delta l/l_0 = 0$. (b) $\Delta l/l_0 = -0.24$. (c) $\Delta l/l_0 = -0.52$. (d) $\Delta l/l_0 = -0.75$.

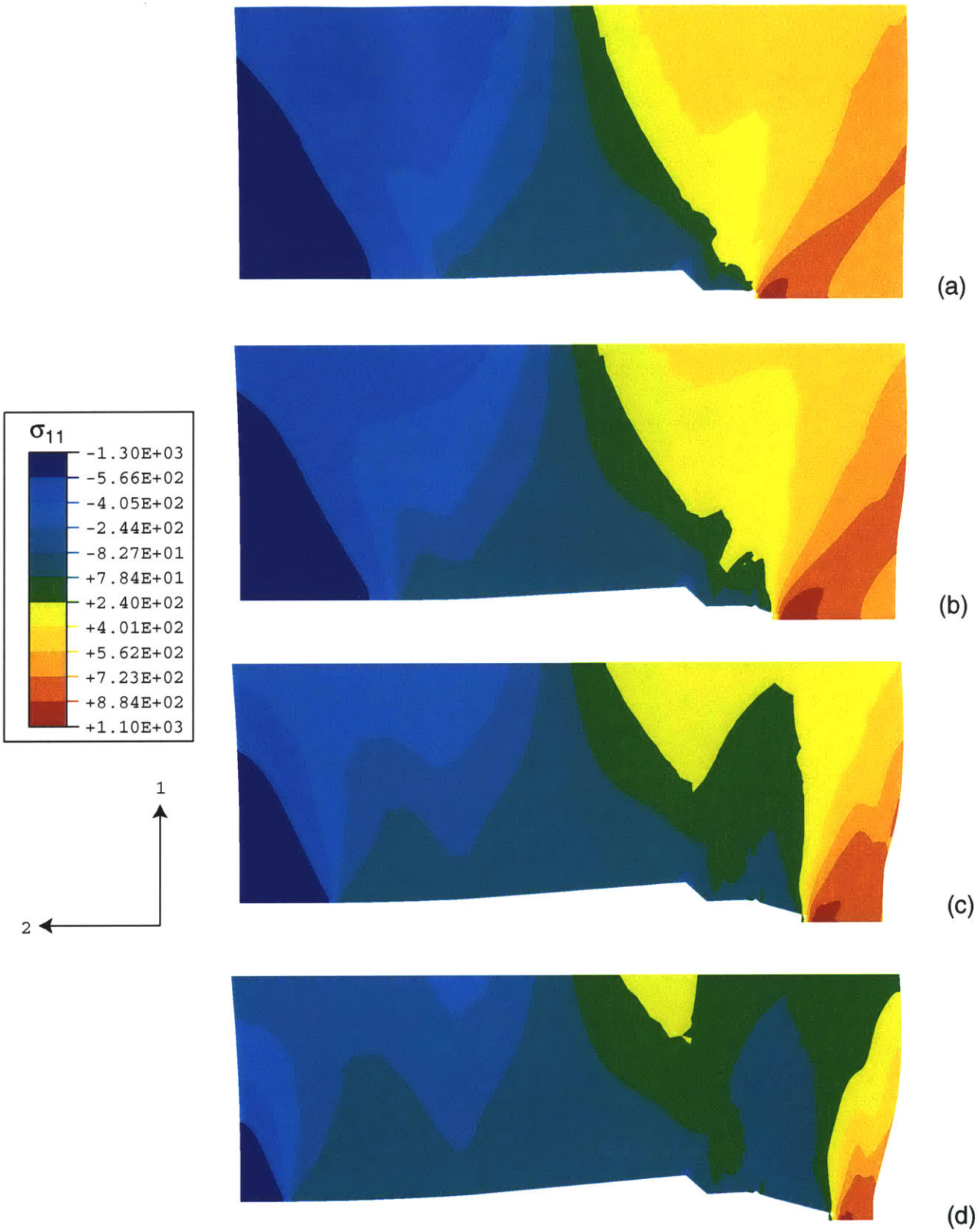

Figure 5-9: Normal stress contour plots of one-half specimens near symmetry line for plane strain back-bending simulations; $l_0 = 6.0$ mm. (a) $\Delta l/l_0 = 0$. (b) $\Delta l/l_0 = -0.24$. (c) $\Delta l/l_0 = -0.52$. (d) $\Delta l/l_0 = -0.75$.

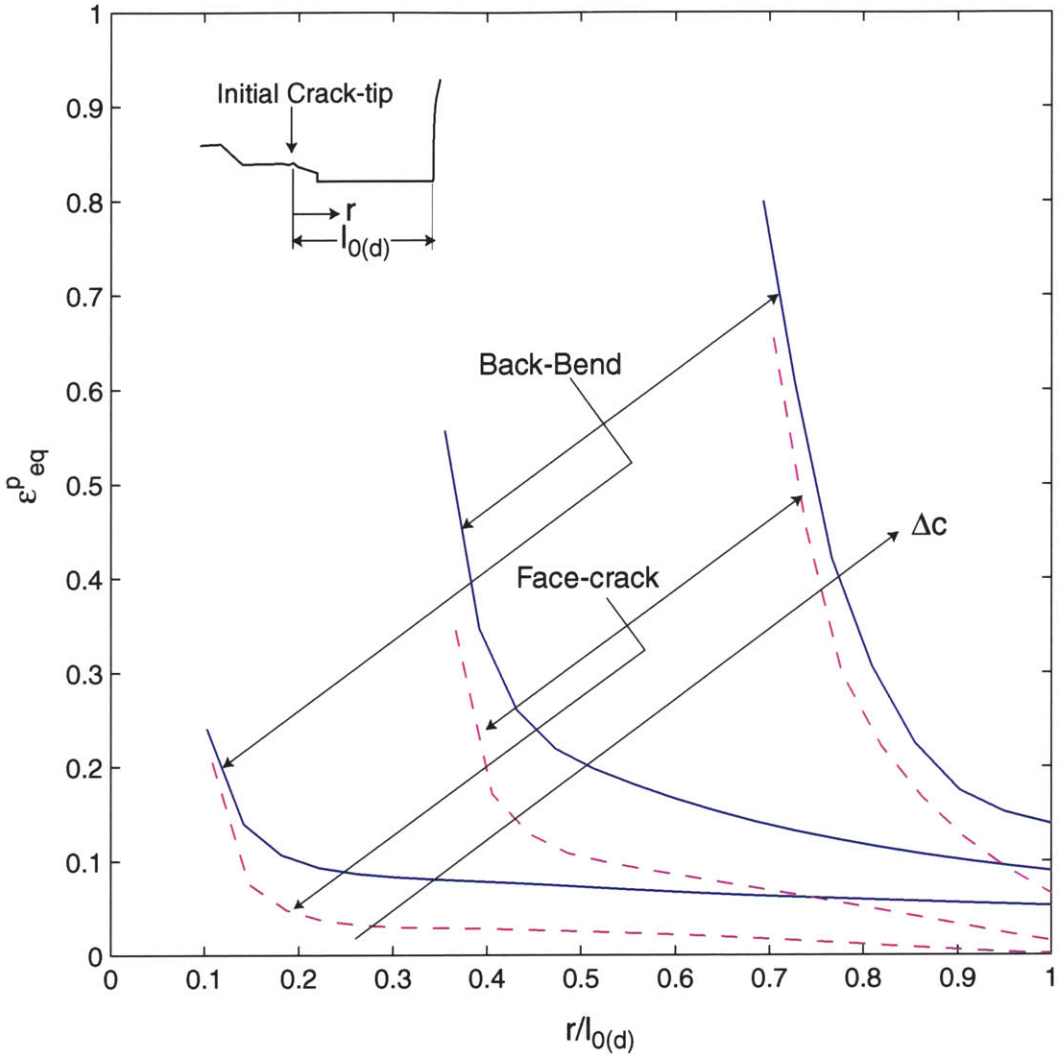

Figure 5-10: Equivalent plastic strain plots for 2-D plane strain finite element runs at increasing levels of crack growth, Δc; $l_0 = 6.0$ mm. Distance r is measured from the initial crack-tip and is normalized with the current (deformed) length of the initial ligament, $l_{0(d)}$.

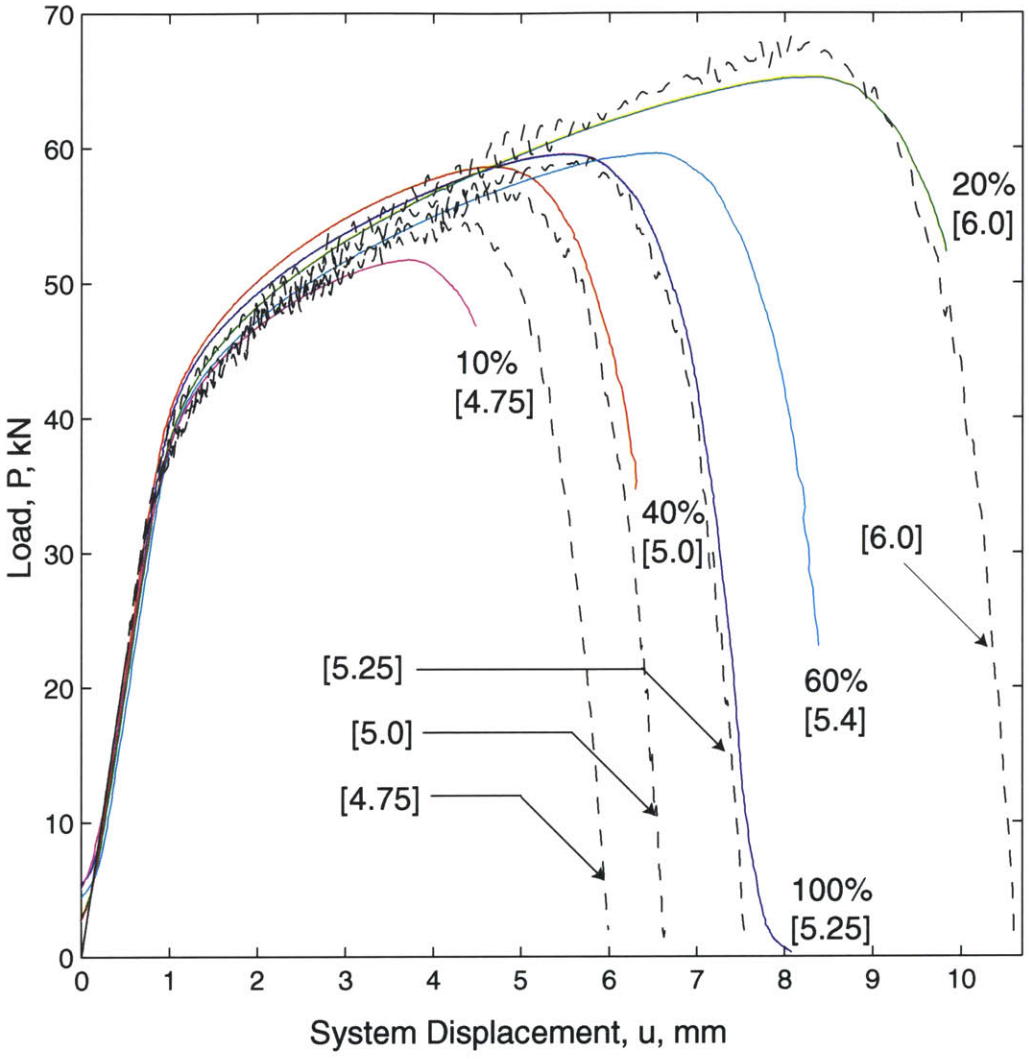

Figure 5-11: Back-bend load-displacement curves: 3-D finite element results (dashed) compared to Experimental (solid). Percentages on the experimental curves are post-peak load-drops. Values in square brackets are the initial ligament length, l_0, in mm.

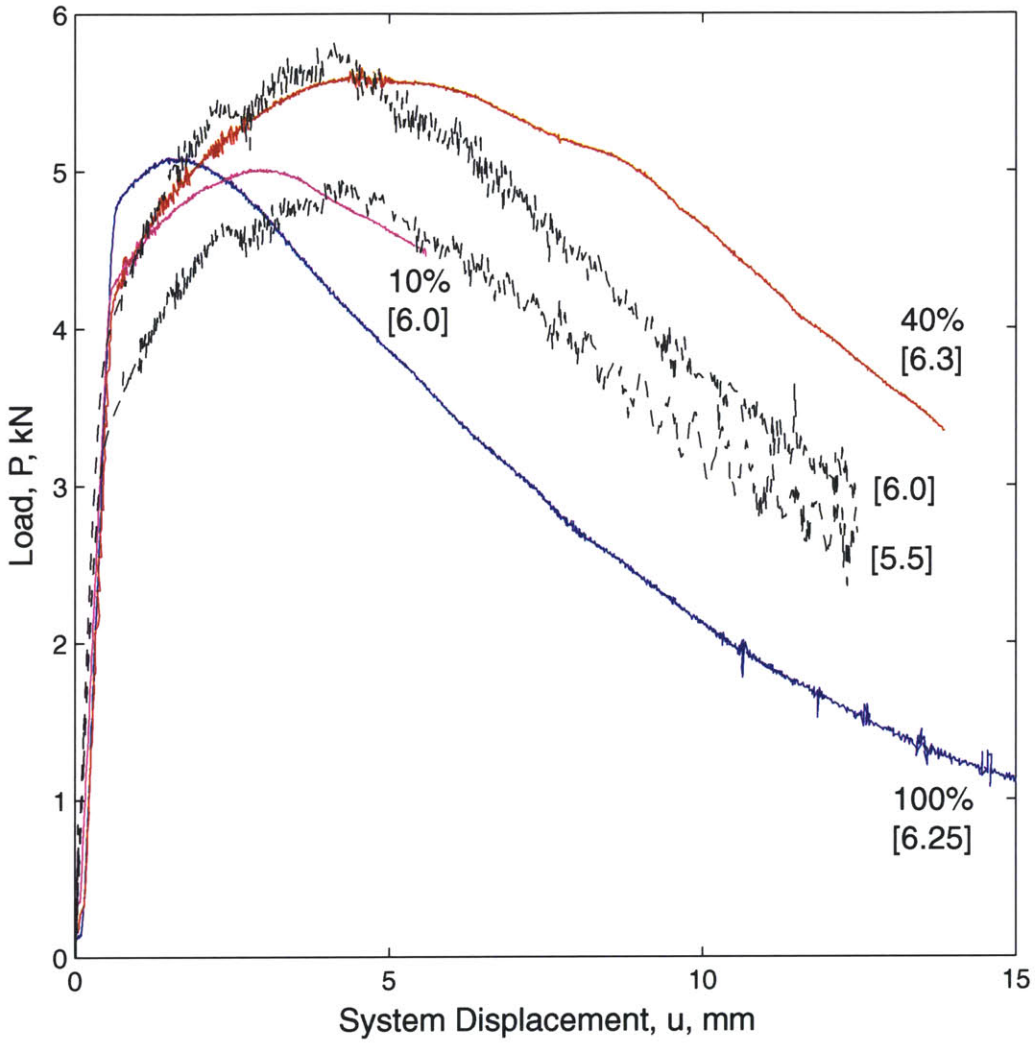

Figure 5-12: Open-bend load-displacement: 3-D finite element results (dashed) compared to Experimental (solid). Percentages on the experimental curves are post-peak load-drops. Values in square brackets are the initial ligament length, l_0, in mm.

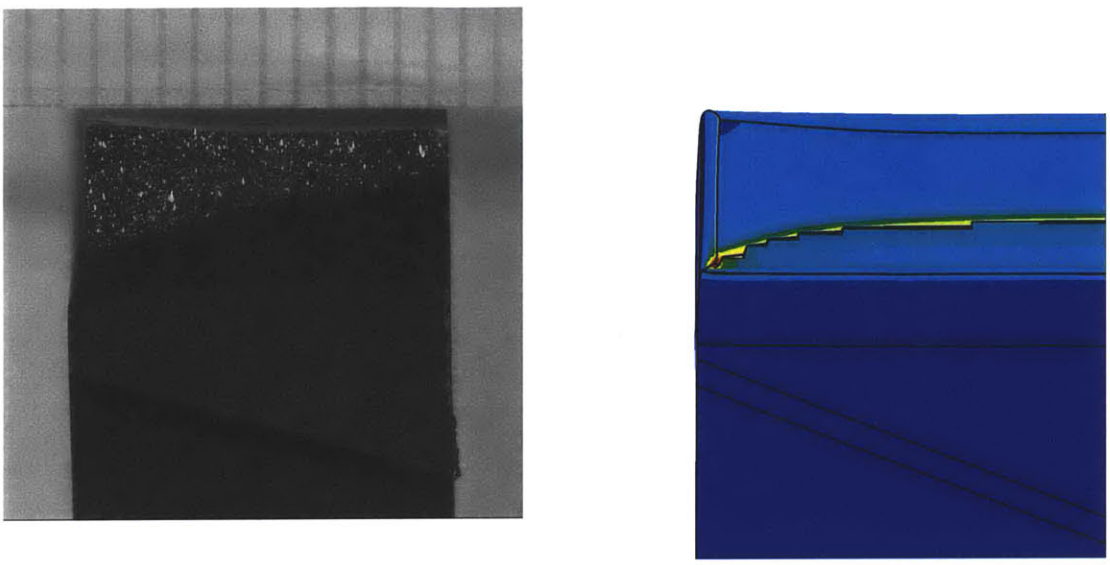

Figure 5-13: Fracture surface profiles for back-bend loading. (a) Experimental at 40% post-peak load-drop. (b) 3-D finite element simulation at 37% post-peak load-drop ($l_0 = 5.0$ mm).

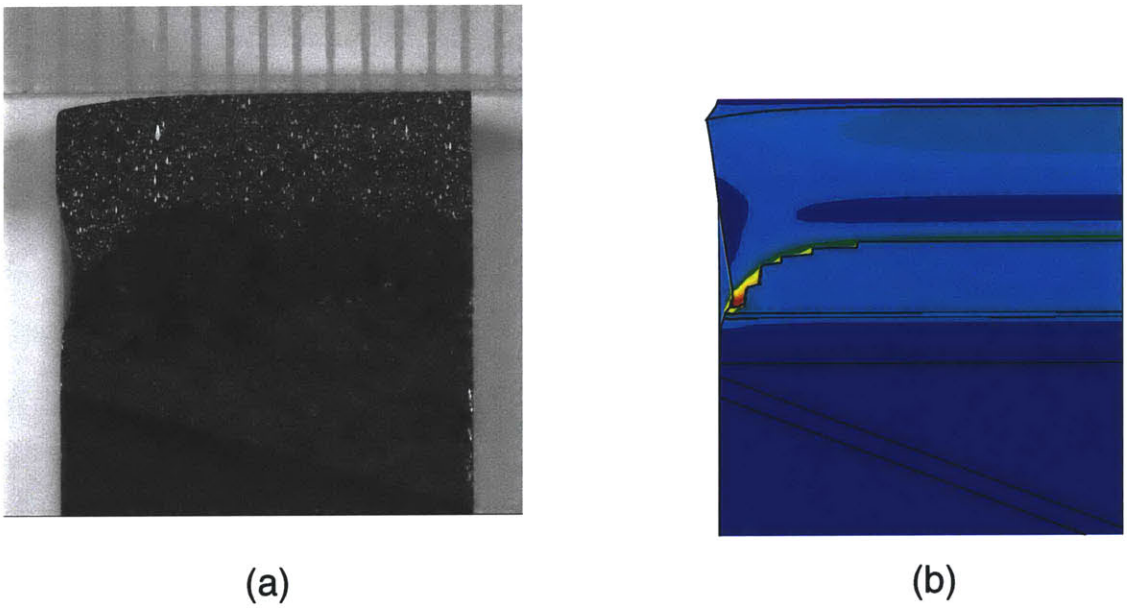

Figure 5-14: Fracture surface profiles for open-bend loading. (a) Experimental at 40% post-peak load-drop. (b) 3-D finite element simulation at 36% post-peak load-drop ($l_0 = 6.0$ mm).

	Back-bend			
	Experimental		Finite Element	
	P-u [4.1]	Topography	2-D	3-D
$CTOD_i$ (mm)	1.2-2.8	0.4	0.4	0.4
	P-u [2.4] & [4.2]	Topography	2-D	3-D
$CTOA$ (°)	30-23	35-20	34	30
	Open-bend			
	Experimental		Finite Element	
	P-u [4.1]	Topography	2-D	3-D
$CTOD_i$ (mm)	0.07-0.27	0.1-0.2	0.2	0.2
	P-u [2.4] & [4.2]	Topography	2-D	3-D
$CTOA$ (°)	9-11	13-17	17	15

Table 5.1: Summary of $CTOD_i$ and $CTOA$ values as obtained from experimental load-displacement (P-u) curves and topography, and calculated finite element results. Numbers in brackets refer to equation numbers used in the calculations.

Chapter 6

Further Discussion of Finite Element Analysis Results

6.1 Study of Stationary Crack using FEA

The back-bend loading was simulated without element deletion in ABAQUS/Standard [24], to study the stationary crack and evaluate the J-Integral. In all analyses considered, the NLGEOM parameter was used to include large-displacement effects. The plane strain 2-D mesh of Figure 3-5 was used with the strain-hardening of Figure 3-4, along with a smaller element size, l_{el} =.06 mm, to better capture the near-crack-tip stresses and strains. The resulting normalized load-displacement and J-Integral plots are shown in Figure 6-1 for back-bending. The loads have been normalized with the limit load of Eq. 2.6 using $\sigma_{flow} = \sigma_{TS}$. Figure 6-2 is an enlargement of Figure 6-1 in the initial elastic portion, which shows a quadratic J vs. displacement curve in the elastic region, followed by an essentially linear portion corresponding to the plastic region. These plots can be compared to the plane strain load-displacement curves of the growing crack in Figure 5-5, to get an estimate of J at initiation. Comparing system displacements u and assuming initiation occurs at peak load, the J at initiation is $\sim$ 350 N/mm ($J_i E/l_0\ \sigma_y^2 = 95.7$) for back-bending. This J-value can be compared to that calculated using Eq. 2.10, given by SLFM2. From Table 5.1, $CTOD_i = 0.4$ mm for back-bending gives J at initiation of 258 N/mm ($J_i E/l_0\ \sigma_y^2 = 70.5$). Eq. 2.11

using $CTOA = 30°$ for back-bending gives $dJ/dc = 345$ N/mm^2.

In small-scale yielding (SSY), the stress intensity factor, K_I in terms of the J-Integral is given by,

$$K_I^2 = JE'. \tag{6.1}$$

Here, $E' = E/(1-\nu^2)$ is the plane strain tensile modulus. Figure 6-3(a) plots K_I-values obtained using Eq. 6.1 and the simulation J-values, here denoted as K_J, plotted vs. the normalized system displacement. Figure 6-3(b) shows normalized K_I-values, $Q_J = K_J/(\sigma_b\sqrt{\pi c})$, where $\sigma_b = 6M/Bt^2$ and $M = Ps/2$. Note that the normalized Q_J-value is constant at 0.179 for the initial portion of loading, as would be expected for an essentially linear elastic system.

The stress intensity factor, K_I, can also be calculated from the simplified elastic superposition, illustrated in Figure 6-4, using

$$K_I = K_{I_M} + K_{I_p}. \tag{6.2}$$

This relation is based on taking the pressure (traction) distribution on the slot-face, $p(x)$, in terms of a normal force per unit breadth, P_{eff}, acting on the slot-face at a distance, x_{eff}, from the back-face as follows:

$$P_{eff} = \int_0^{l_c} p(x)dx; \tag{6.3}$$

$$x_{eff} = \frac{1}{P_{eff}}\int_0^{l_c} xp(x)dx; \tag{6.4}$$

Here, l_c is the (solution-dependent) distance over which slot-face/shim contact takes place. In Eq. 6.2, K_{I_M} is the (intrinsically negative) stress intensity factor for a finite-width plate with a single edge crack under a closing bending moment M (as seen in Figure 6-4) and is given by [30]:

$$K_{I_M} = \frac{-6M}{Bt^2}\sqrt{\pi c}\, F_I(c/t), \tag{6.5}$$

where, $F_I(c/t)$ is the correction factor obtained from [30]. K_{I_p} is the stress intensity

factor for a finite-width plate with a single edge crack loaded at its crack surfaces with a pair of normal forces per unit breadth P_{eff} acting at x_{eff} (as seen in Figure 6-4) and is given by [31]:

$$K_{I_p} = \frac{P_{eff}}{\sqrt{\pi c}} G(c/t, x_{eff}/c), \tag{6.6}$$

where, $G(c/t, x/(c/t))$ is the Green's function (or weight function) given by [31] as:

$$G(c/t, x_{eff}/c) = \sqrt{\frac{1-(x_{eff}/c)}{2}} \sum_{i=1}^{5} \beta_i(c/t) \cdot \left(1 - \frac{x_{eff}}{c}\right)^{i-2}. \tag{6.7}$$

Here, $\beta_i(c/t)$ are correction factors. The finite element simulations are used to obtain the value of P_{eff}, the reaction force per unit breadth on the rigid shim surface. x_{eff} is obtained by equating the reaction moment on the rigid shim surface to that caused by P_{eff}, applied at a position x_{eff}, in order to determine the coordinate of the applied reaction force. Using simulation values of $M = Ps/2$, P_{eff} and x_{eff}, Eqs. 6.2 through 6.6 give K_I as plotted in Figure 6-5. These K_I values are consistent with those calculated from the J-Integral. A somewhat more accurate superposition calculation could be performed by weighting the infinitesimal traction forces, $p(x)dx$, with the position-dependent weight function, to obtain

$$dK_{Ip} = \frac{p(x)dx}{\sqrt{\pi c}} G(c/t, x/c), \tag{6.8}$$

and then integrating.

Figure 6-6 shows the near-tip crack opening stress at several levels of loading, from contained yielding to fully-plastic levels. Opening stress is normalized by σ_y, and distance ahead of the tip is normalized by J/σ_y. In order to plot the near-crack-tip stresses, a dense circular mesh focused onto the crack-tip was used, as the previously used mesh proved to be too coarse. The plot shows how the local fields evolve from high-triaxiality, contained yielding (curves corresponding to $u/s = 0.008$, 0.010 and 0.012) into low-triaxiality, fully-plastic fields (curve corresponding to $u/s = 0.020$). This then motivates the size-scale study (discussed in Section 6.2, below) in that locally "critical" conditions in a larger, geometrically-similar specimen, might occur

at contained yielding and high-triaxiality, rather than at a fully-plastic, low-triaxiality state.

Figure 6-7 shows the plastic zone sizes, at four levels of loading during contained yielding. In (a) the plastic zones are spatially normalized by J/σ_y, while (b) plots the un-normalized coordinates. Contours plots shows the equivalent plastic strains. Figure 6-8 plots the plastic zone radius r_p vs. normalized displacement.

The load-displacement and J-Integral plots for the stationary crack simulation of open-bending are shown in Figure 6-9. The plot gives a J at initiation of $\sim$ 250 N/mm ($J_i E/l_0\ \sigma_y^2 = 68.3$) for open-bending (when compared to the plane strain load-displacement curves of the growing crack in Figure 5-6). The J at initiation can be calculated using Eq. 2.10, with $CTOD_i = 0.2$ mm from Table 5.1, and is 241 N/mm ($J_i E/l_0\ \sigma_y^2 = 65.9$) for open-bending. Eq. 2.11 using using $CTOA = 15°$ for open-bending gives $dJ/dc = 289$ N/mm^2.

6.2 Scale Effects

The scale effect in back-bending simulations was studied in plane strain by simulating a specimen four times as large as the one already considered, with $t = 101.6$ mm, $s = 254$ mm and $l_0 = 24$ mm, while keeping the same element size l_{el} =0.24 mm. In Figure 6-10(a) the normalized load-displacement curve for this larger specimen is compared to that of the smaller ($t = 25.4$ mm; $l_0 = 6.0$ mm) specimen of Figure 3-3. The loads have been normalized with the limit load of Eq. 2.6 using $\sigma_{flow} = \sigma_{TS}$. In the size-effect study, the machine compliance was not included, and thus the loads are plotted vs. the normalized specimen displacement, u_{spec}/s. The plot shows the larger specimen has an earlier load drop-off (corresponding to lower $CTOD_i$) and has a similar slope (corresponding to same $CTOA$) during the initial crack growth, before the crack tends to run along the 45° shear band. When the simulation was re-run using the GTN model with element deletion throughout the mesh (as per Figure 5-1(c)), the crack ran along the 45° shear band after a few millimeters of symmetric cracking, as illustrated in Figure 6-11.

To compare the load-displacement curves of the two specimen sizes for (enforced) similar symmetric straight-ahead cracking, the GTN model restricted to a single layer of interface elements (as per Figure 5-1(a)) was used. The resulting load-displacement curves in Figure 6-10(b), show that the larger specimen has an earlier load drop-off and a downward slope similar to the smaller specimen.

The deformed crack profiles at initiation (of the simulations corresponding to Figure 6-10(a)) give a $CTOD_i$ of $\sim$ 0.4 mm for the smaller specimen and $\sim$ 0.4 – 0.5 mm for the larger specimen. Figures 6-12 and 6-13 show the equivalent plastic strain contour plots for the two specimens sizes at equivalent amounts of cracking, Δc =2 mm and Δc =3.5 mm, respectively. The deformed shapes show a $CTOA$ of $\sim 30°$ for the smaller specimen compared to a $CTOA$ decreasing to $\sim 30°$ from close to 40° for the larger specimen (as inferred from the curvature in the deformed shape of the crack-growth in Figure 6-11(b)).

Figure 6-14 plots the crack opening stresses for the two specimens vs. distance from the crack-tip, both after crack extensions, Δc =2 mm. The plot shows a high-triaxiality (contained-yielding) field for the larger specimen compared to a low-triaxiality (fully-plastic) field for the smaller specimen.

6.3 Non-Hardening Simulations

The back-bending plane strain simulations of Chapter 5 were repeated with the non-hardening idealization. With the GTN model distribution of Figure 5-1(b) adopted for the strain-hardening runs, the elements sheared along the 45° shear band as seen in Figure 6-15(a), and there was no crack growth along the symmetry line. When run with the GTN model distribution of Figure 5-1(c) allowing element deletion throughout the mesh, the elements failed along the 45° shear band as seen in Figure 6-15(b). In order to allow only symmetric straight-ahead cracking, the GTN model was restricted to single layer of interface elements next to the specimen mid-plane, as per Figure 5-1(a). The equivalent plastic strain contour plots for this run is plotted in Figure 6-15(c). The load-displacement curves for the three GTN model distributions

are shown in Figure 6-16. The loads have been normalized with the limit load of Eq. 2.6 using $\sigma_{flow} = \sigma_y$.

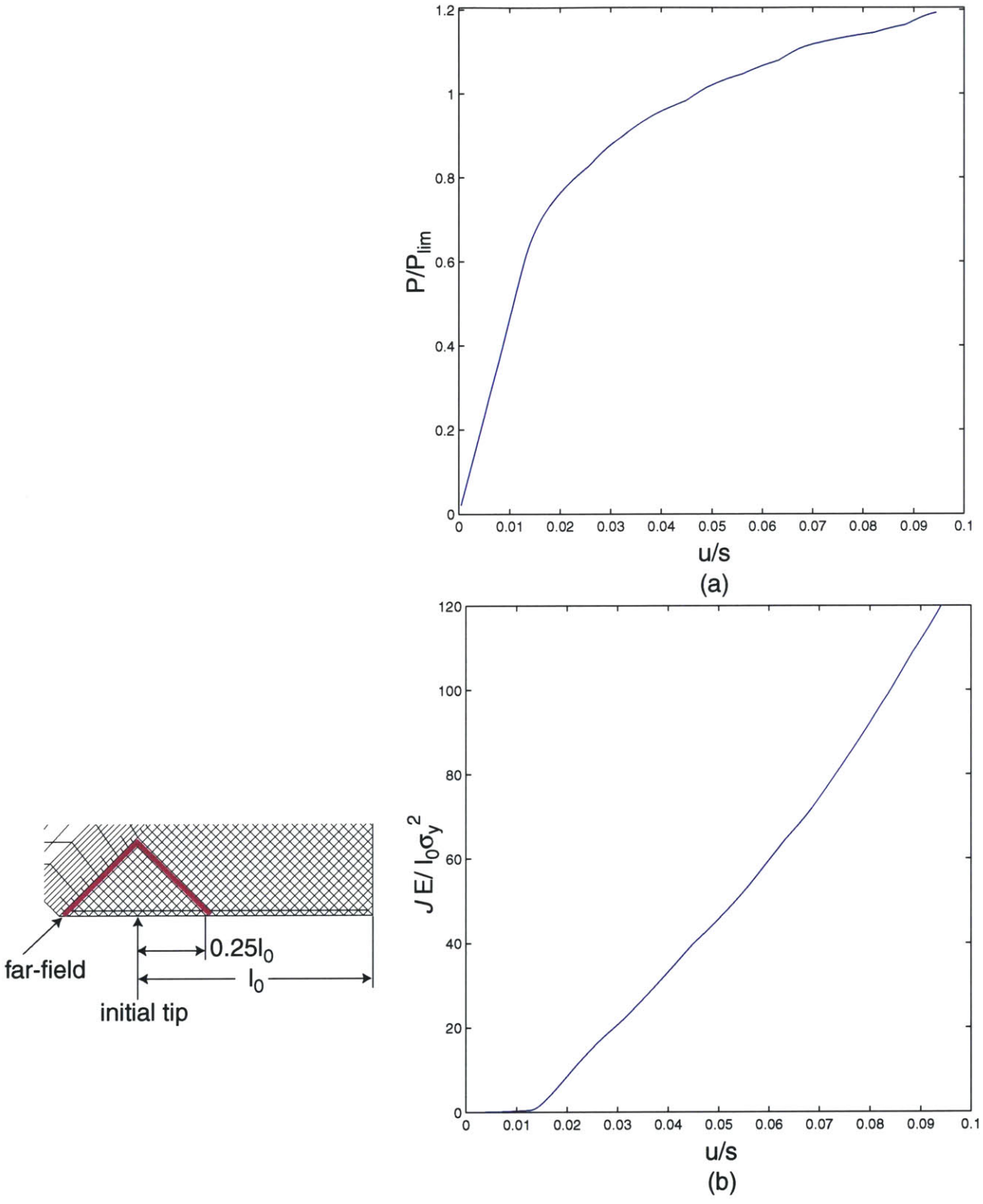

Figure 6-1: Back-bend plane strain finite element simulations of stationary cracks, $l_0 = 6.0$ mm. (a) Normalized load-displacement curve. (b) Normalized J-Integral plot evaluated at far-field.

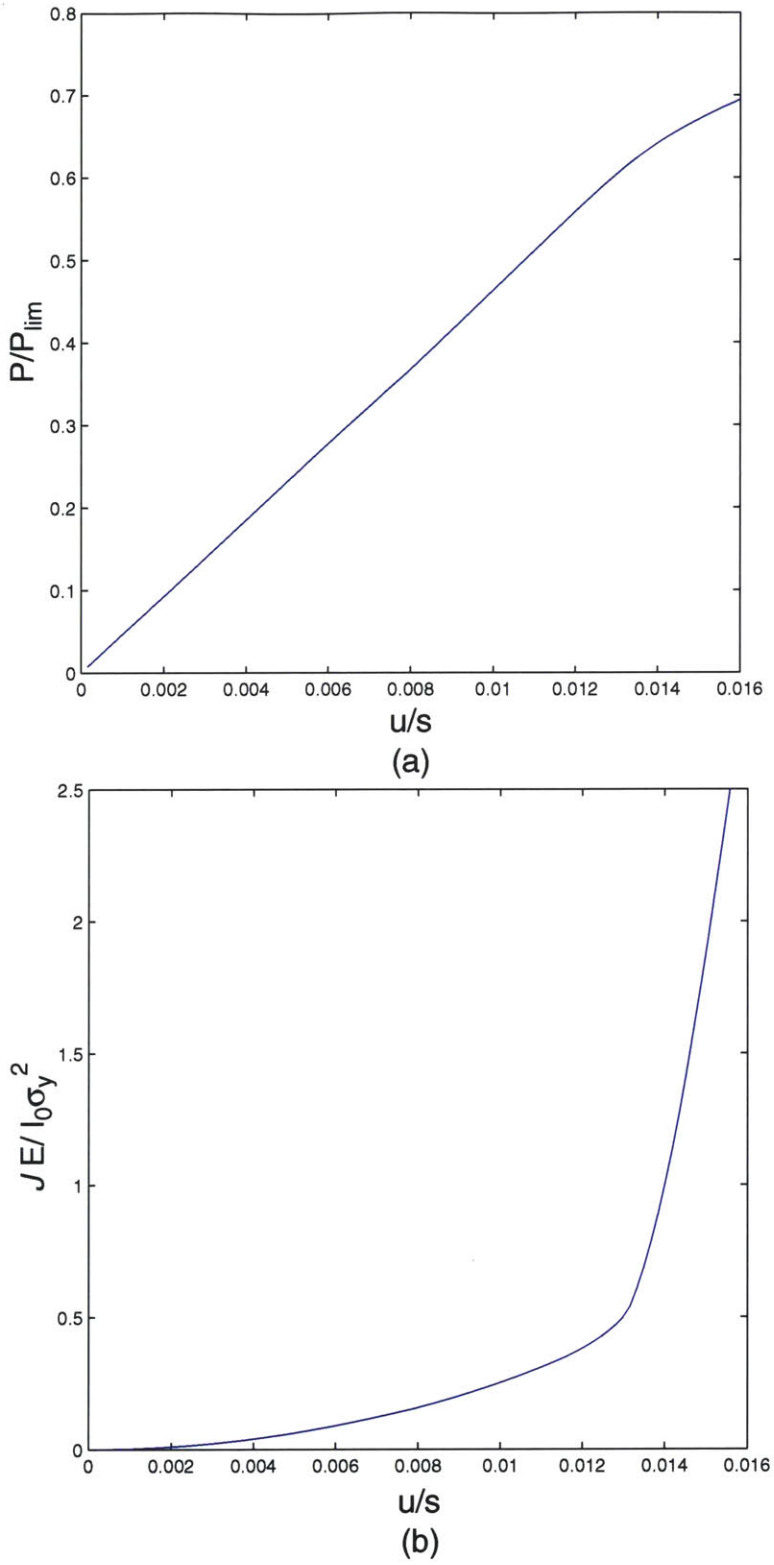

Figure 6-2: Enlargement of Figure 6-1 in the initial elastic portion. (a) Normalized load-displacement curve. (b) Normalized J-Integral plot.

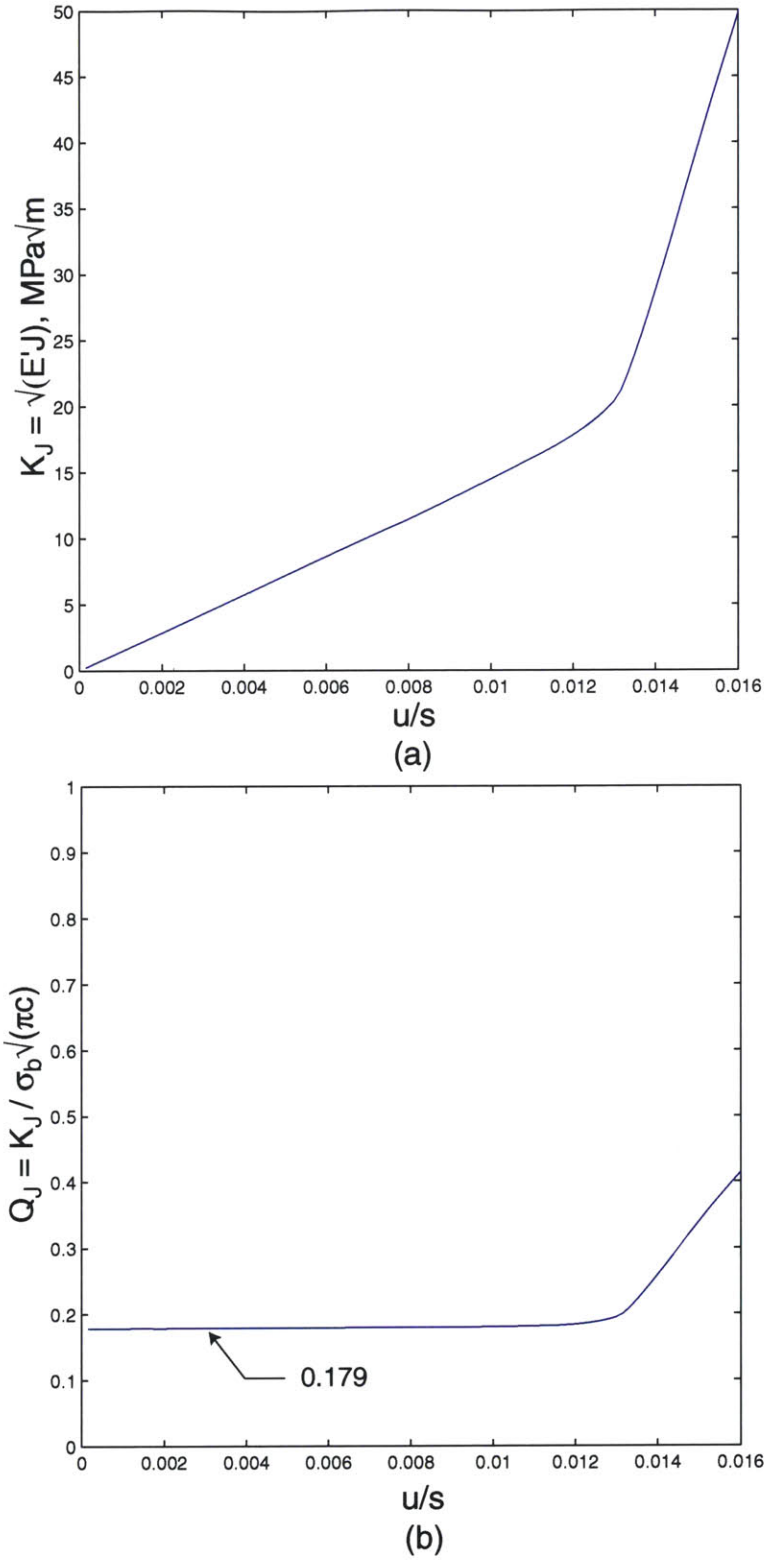

Figure 6-3: (a) Stress intensity factor K_J, calculated from the J-Integral, vs. normalized displacement. (b) Normalized stress intensity factor, $Q_J = K_J / (\sigma_b\sqrt{\pi c})$, vs. normalized displacement. For back-bend loading; $l_0 = 6.0$ mm.

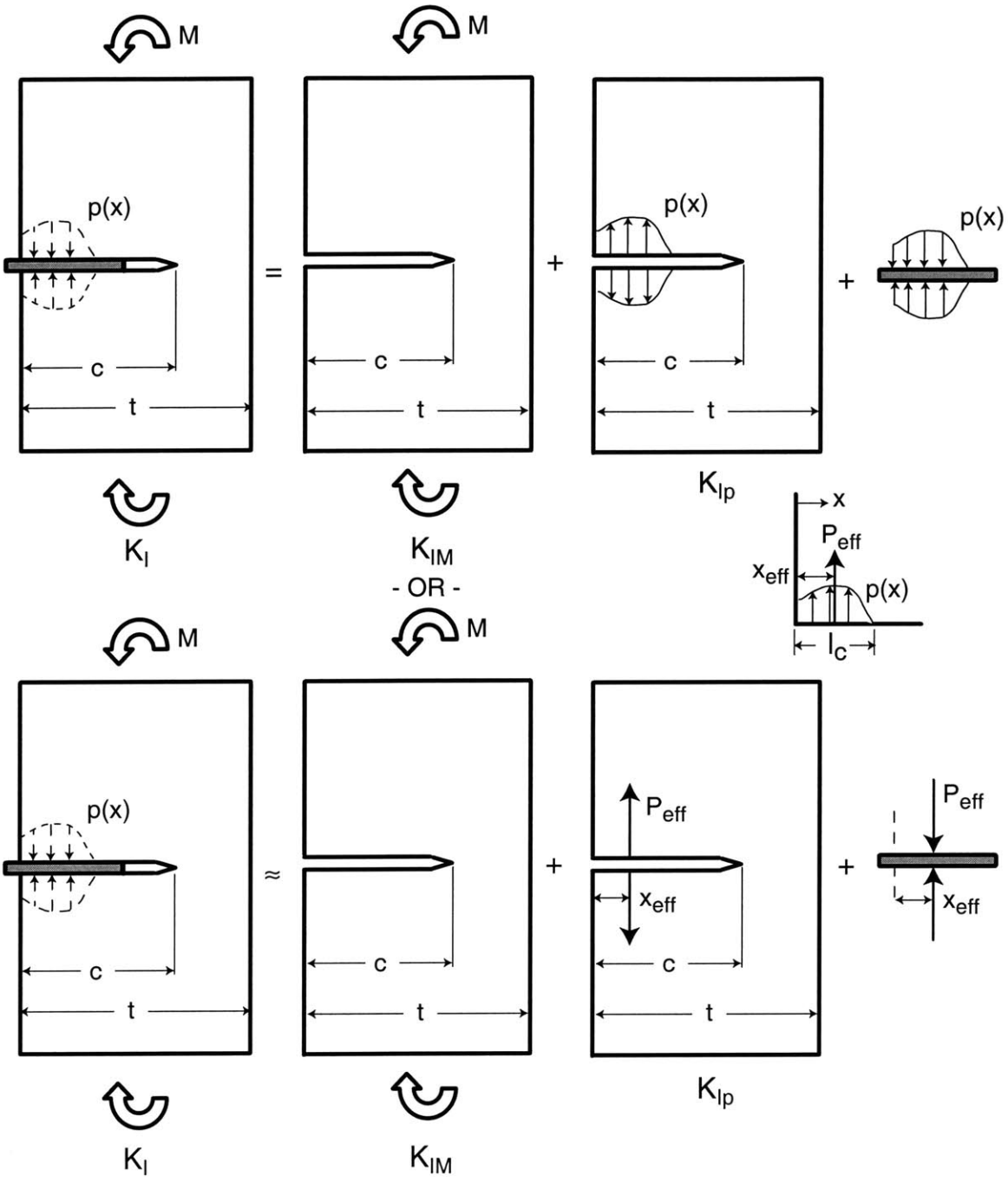

Figure 6-4: Calculation of K_I from elastic superposition: $K_I = K_{I_M} + K_{I_p}$.

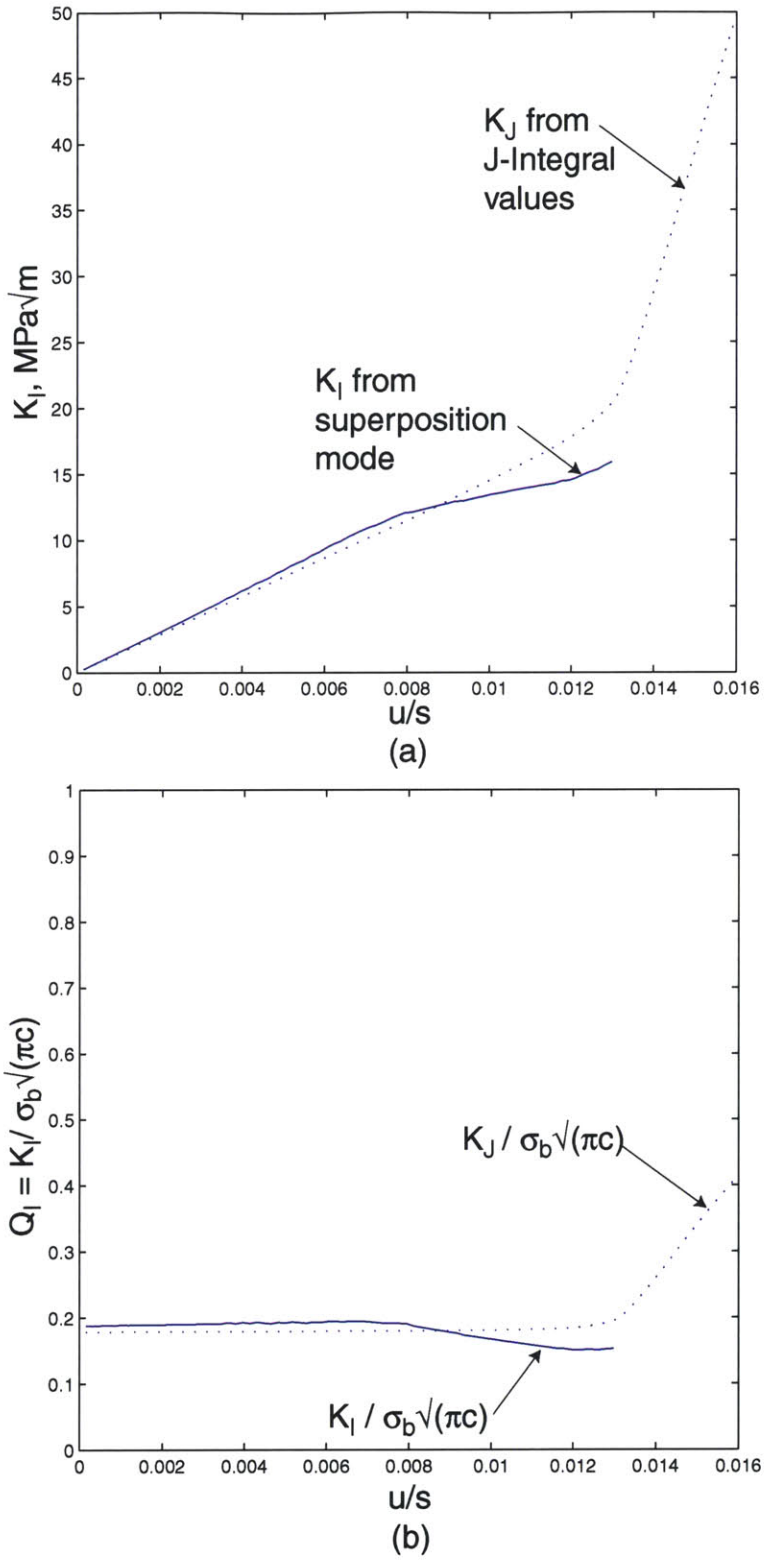

Figure 6-5: (a) Stress intensity factor K_I, calculated using Eq. 6.2, vs. normalized displacement. (b) Normalized stress intensity factor, $Q = K_I/\left(\sigma_b\sqrt{\pi c}\right)$, vs. normalized displacement. Dashed lines show K_J calculated from the J-Integral. For back-bend loading; $l_0 = 6.0$ mm.

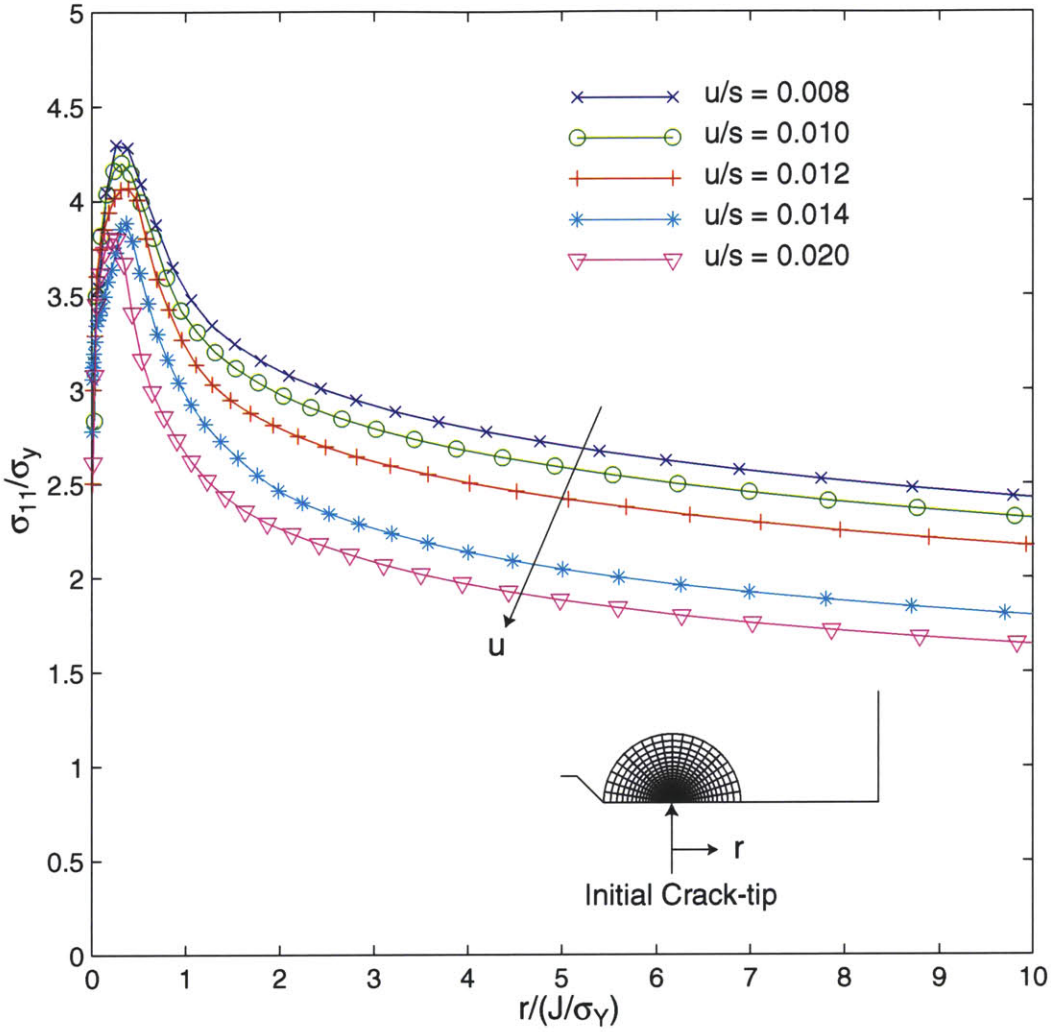

Figure 6-6: Normalized crack opening stress vs. normalized distance ahead of the tip, for plane strain back-bend simulations of stationary cracks. At increasing levels of applied load from contained yielding to fully plastic levels, $u/s = 0.008$, 0.01, 0.012, 0.014 and 0.02; $l_0 = 6.0$ mm.

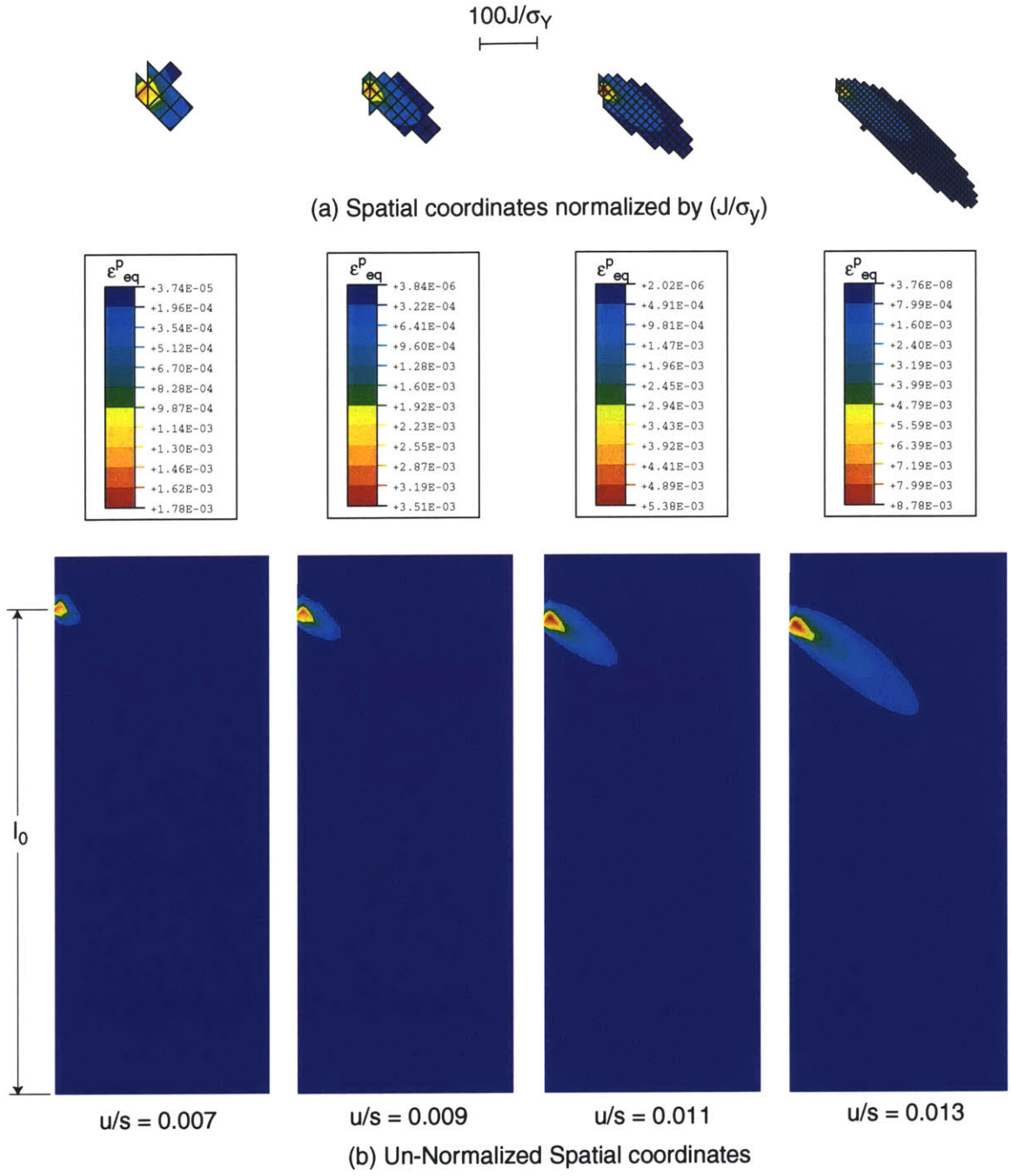

Figure 6-7: Plastic zone sizes for plane strain back-bend simulations of stationary cracks during contained yielding. At increasing levels of applied load, $u/s = 0.007$, 0.009, 0.011 and 0.013; $l_0 = 6.0$ mm. (a) Spatial coordinates normalized by J/σ_y. (b) Un-normalized spatial coordinates.

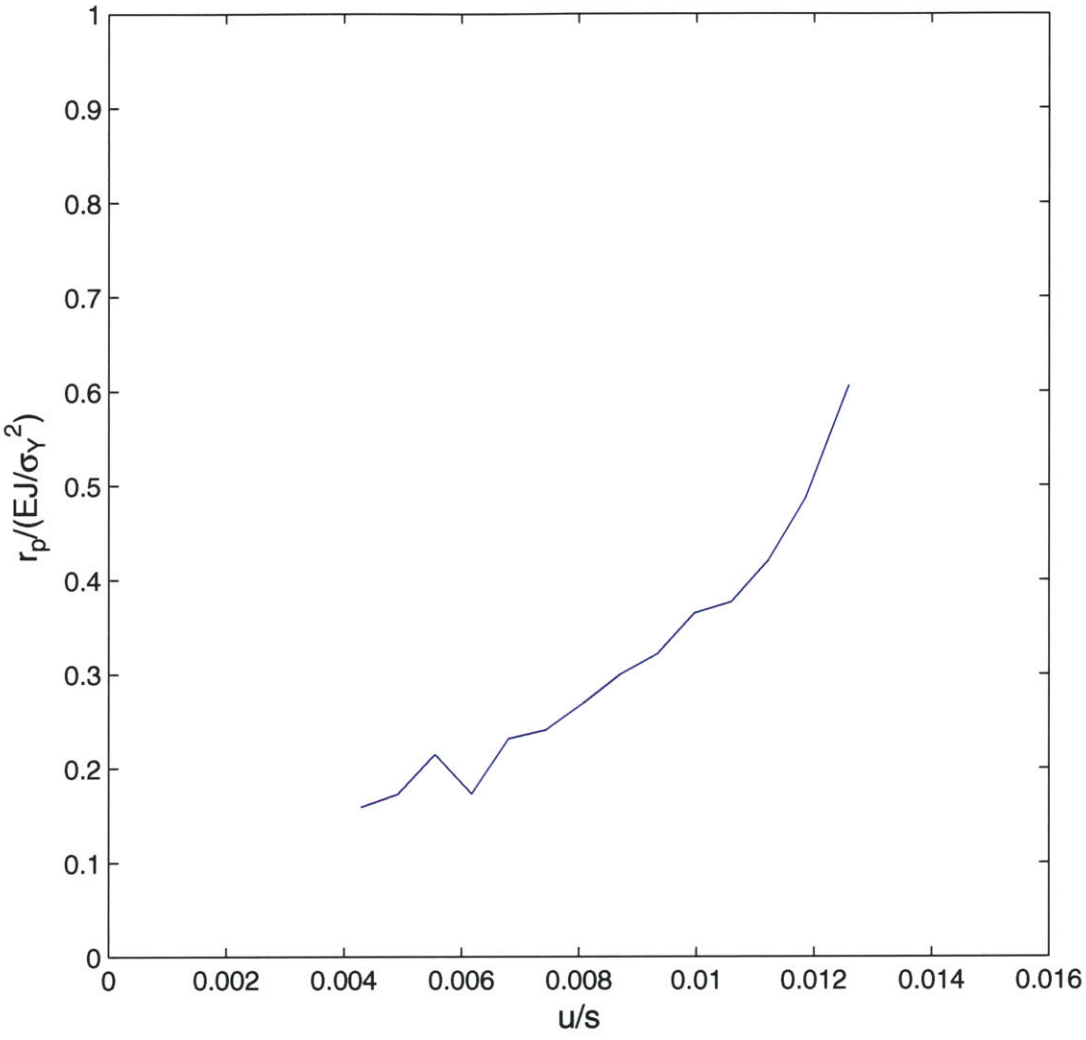

Figure 6-8: Normalized plastic zone radius, r_p, vs. normalized displacement for plane strain back-bend simulations of stationary cracks during contained yielding; l_0 = 6.0 mm.

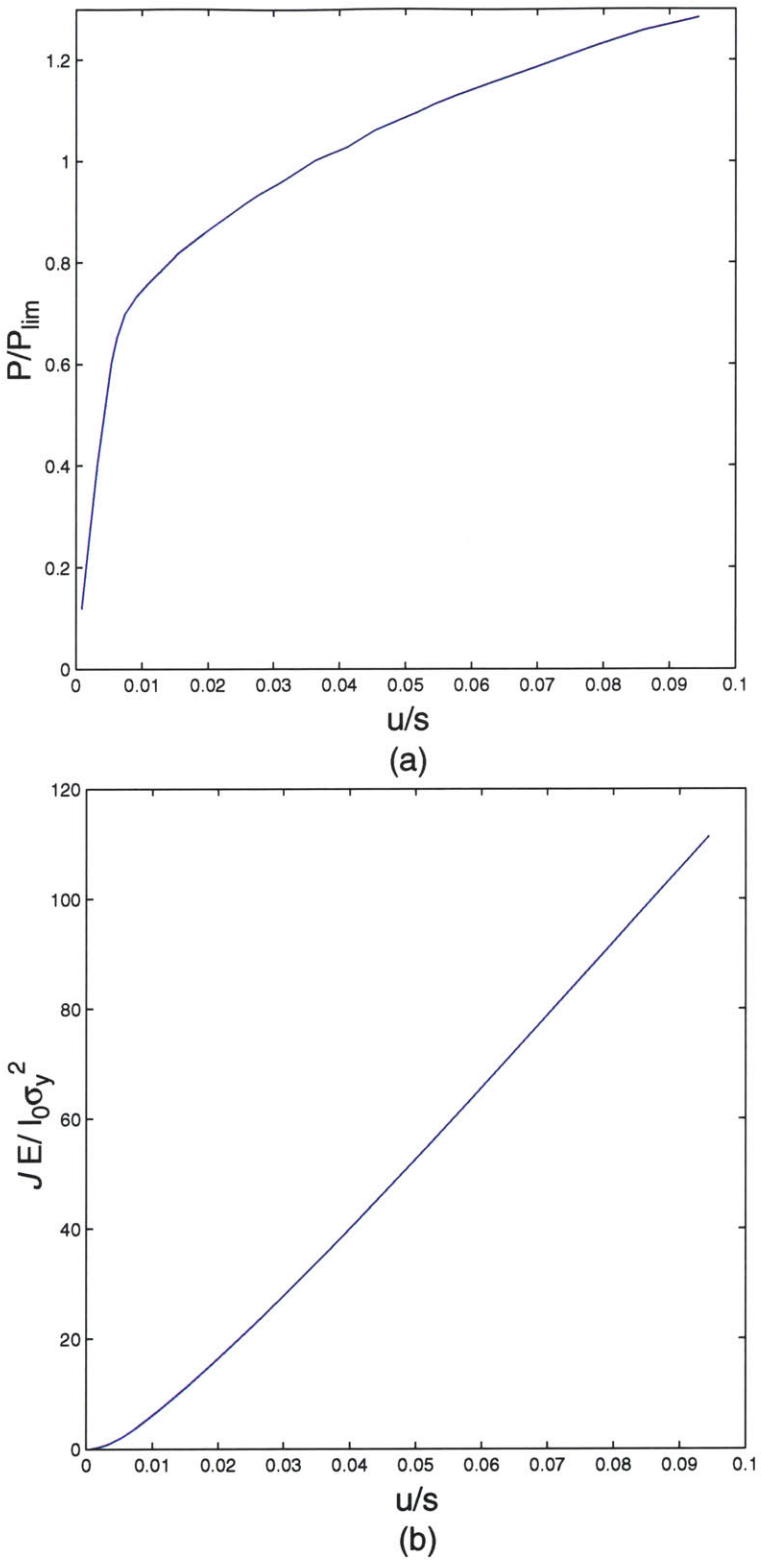

Figure 6-9: Open-bend plane strain finite element simulations of stationary cracks, $l_0 = 6.0$ mm. (a) Normalized load-displacement curve. (b) Normalized J-Integral plot.

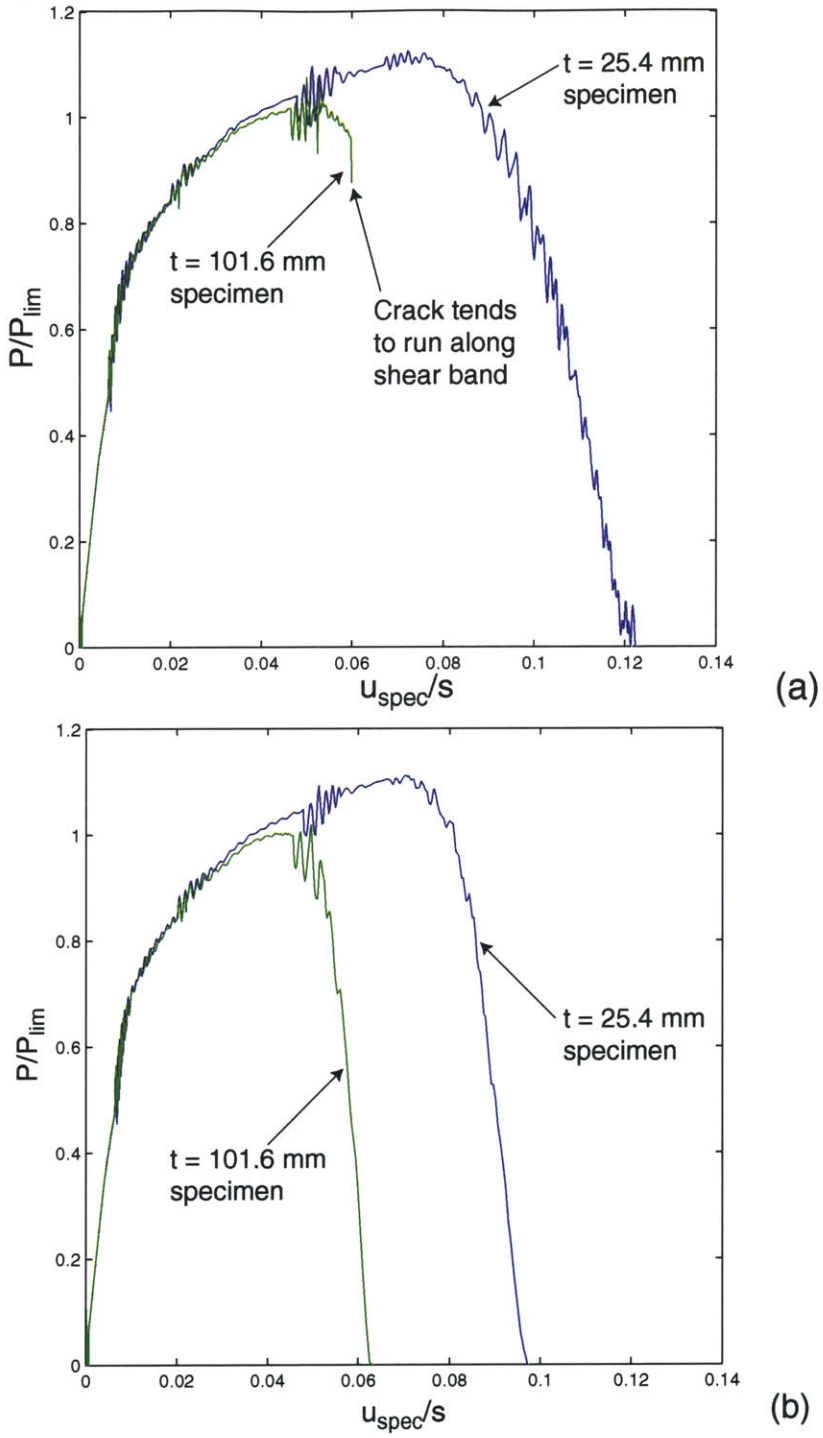

Figure 6-10: Back-bend normalized load-displacement curves for plane strain finite element runs. For two specimen sizes, $t = 25.4$ mm and $t = 101.6$ mm. (a) With the GTN model assigned throughout the mesh; single layer of interface elements next to the specimen mid-plane were allowed element deletion. (b) With the GTN model restricted to single layer of interface elements next to the specimen mid-plane.

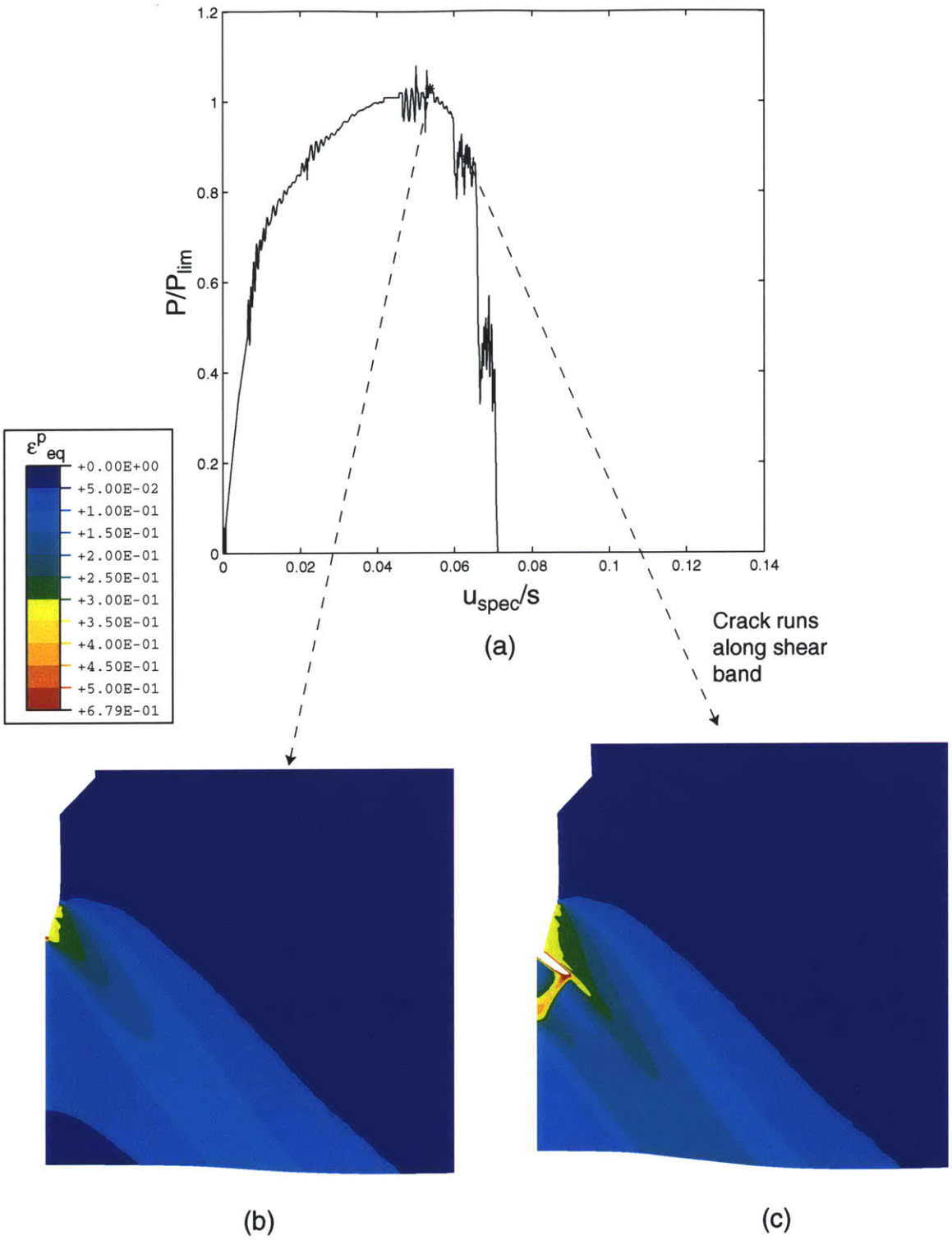

Figure 6-11: (a) Back-bend normalized load-displacement curve for larger specimen, $t = 101.6$ mm, with the GTN model allowing element deletion throughout the mesh. Contour plots show the deformed mesh at two stages: (b) at a few millimeter crack growth and (c) when the crack runs along the shear band.

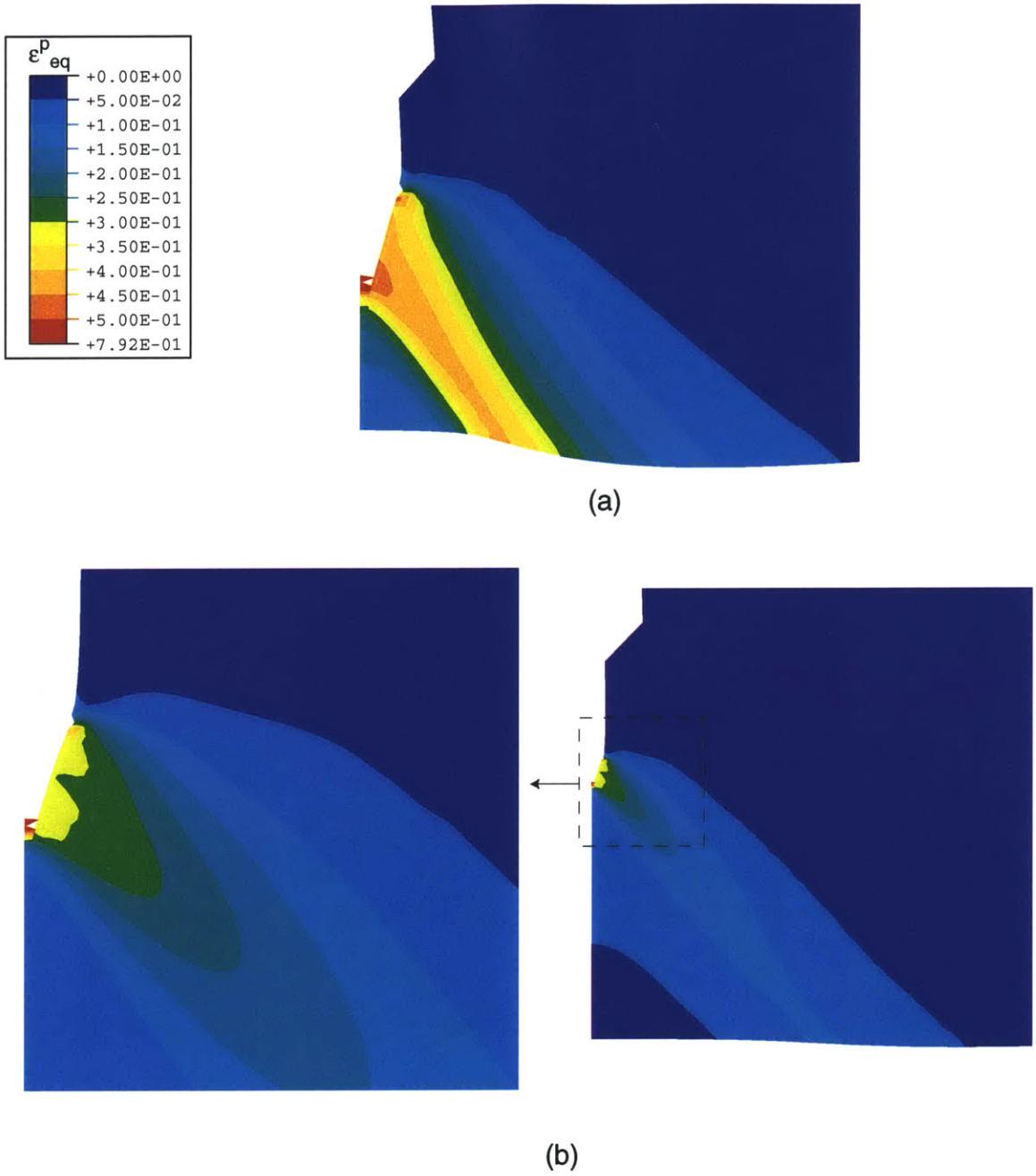

Figure 6-12: Equivalent plastic strain contour plots of one-half specimens near symmetry line for plane strain back-bending simulations. For two specimen sizes at equivalent cracking of $\Delta c = 2$ mm. (a) $t = 25.4$ mm specimen; $P/P_{lim} = 0.78$, $u_{spec}/s = 0.101$. (b) $t = 101.6$ mm specimen, $P/P_{lim} = 1.03$, $u_{spec}/s = 0.050$.

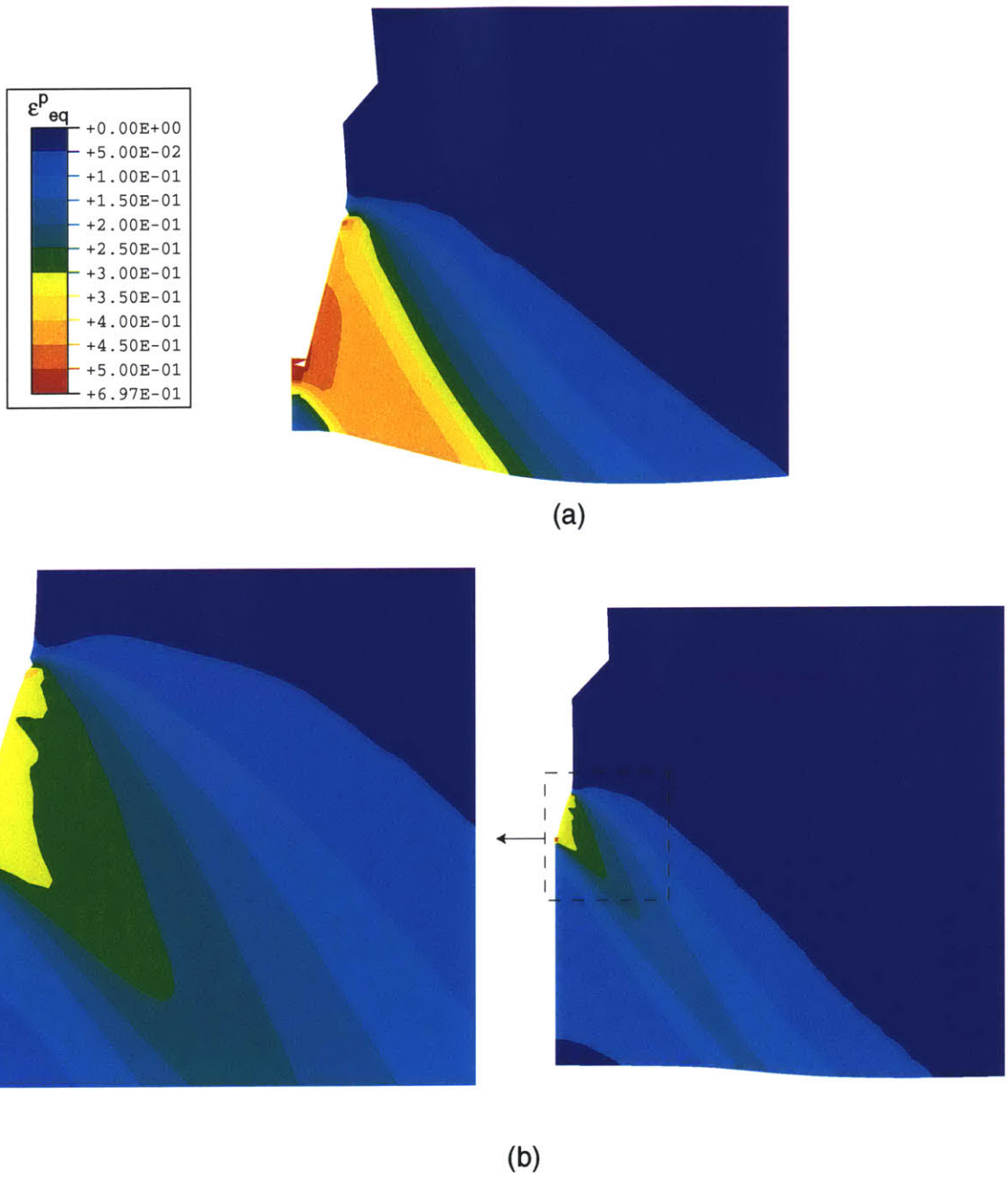

Figure 6-13: Equivalent plastic strain contour plots of one-half specimens near symmetry line for plane strain back-bending simulations. For two specimen sizes at equivalent cracking of $\Delta c = 3.5$ mm. (a) $t = 25.4$ mm specimen; $P/P_{lim} = 0.34$, $u_{spec}/s = 0.113$. (b) $t = 101.6$ mm specimen; $P/P_{lim} = 0.99$, $u_{spec}/s = .057$.

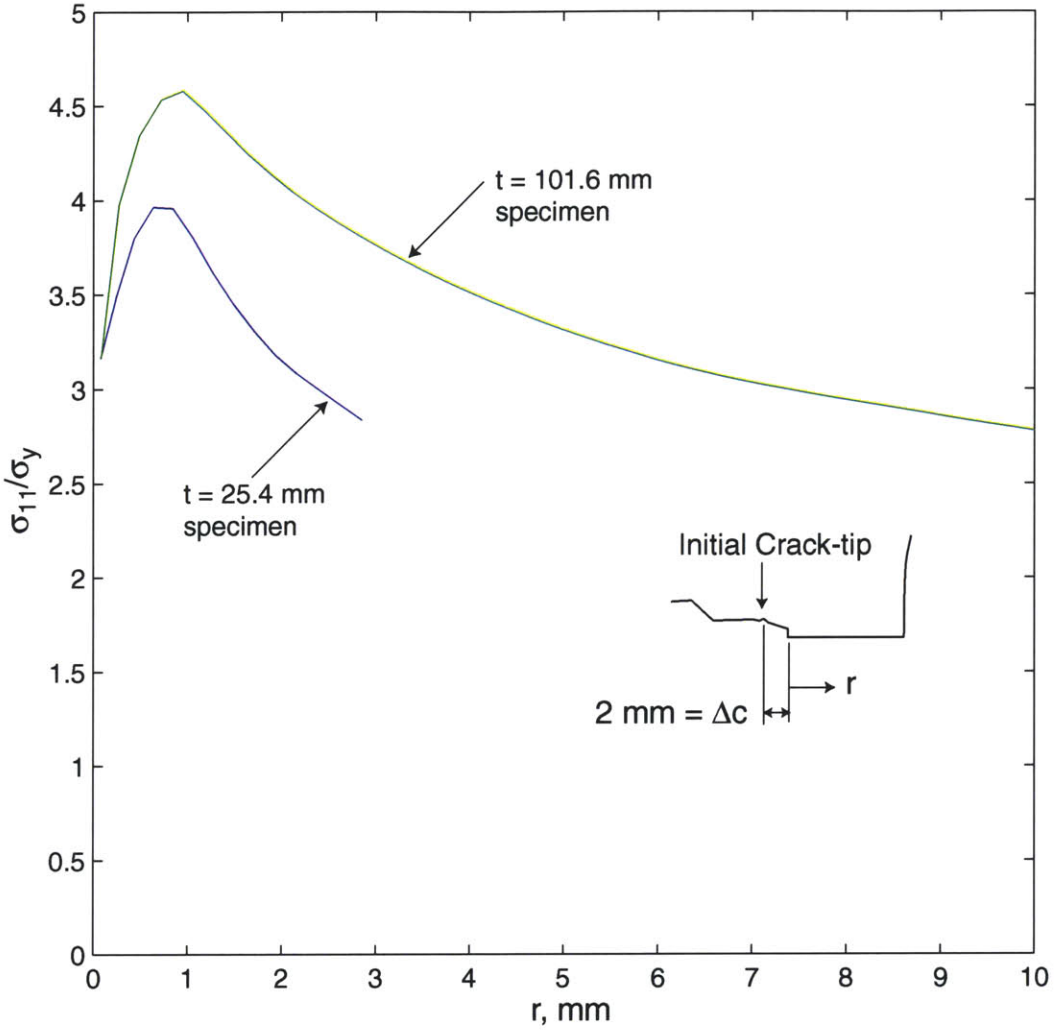

Figure 6-14: Normalized crack opening stress vs. distance ahead of the tip. For two specimen sizes, $t = 25.4$ mm and $t = 101.6$ mm, at equivalent cracking of $\Delta c = 2$ mm.

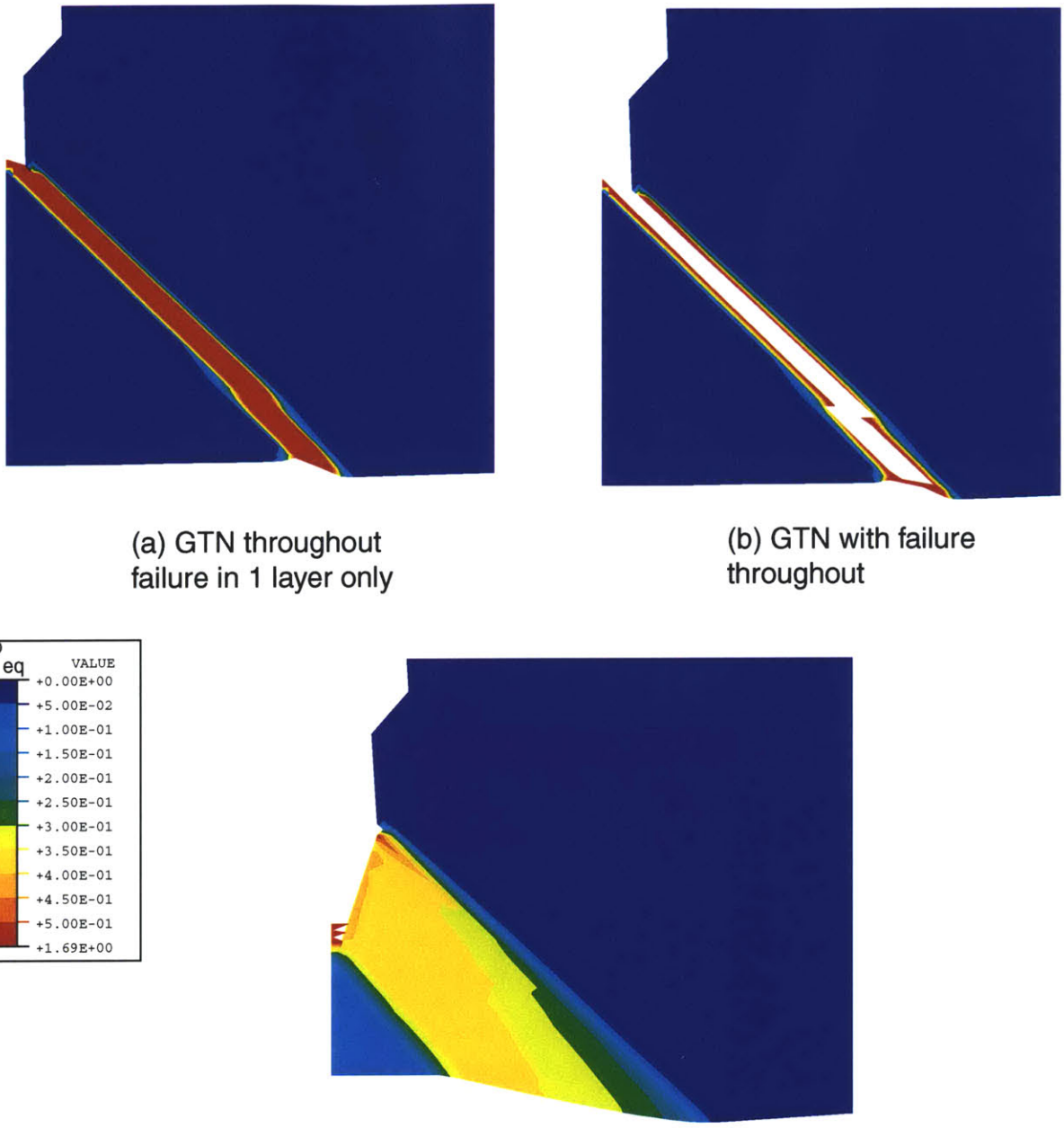

Figure 6-15: Equivalent plastic strain contour plots of one-half specimens near symmetry line for plane strain non-hardening back-bending simulations; $l_0 = 6.0$ mm. (a) With the GTN model assigned throughout the mesh; single layer of interface elements next to the specimen mid-plane were allowed element deletion. (b) With the GTN model allowing element deletion throughout the mesh. (c) With the GTN model restricted to single layer of interface elements next to the specimen mid-plane; $\Delta l/l_0 = -0.55$.

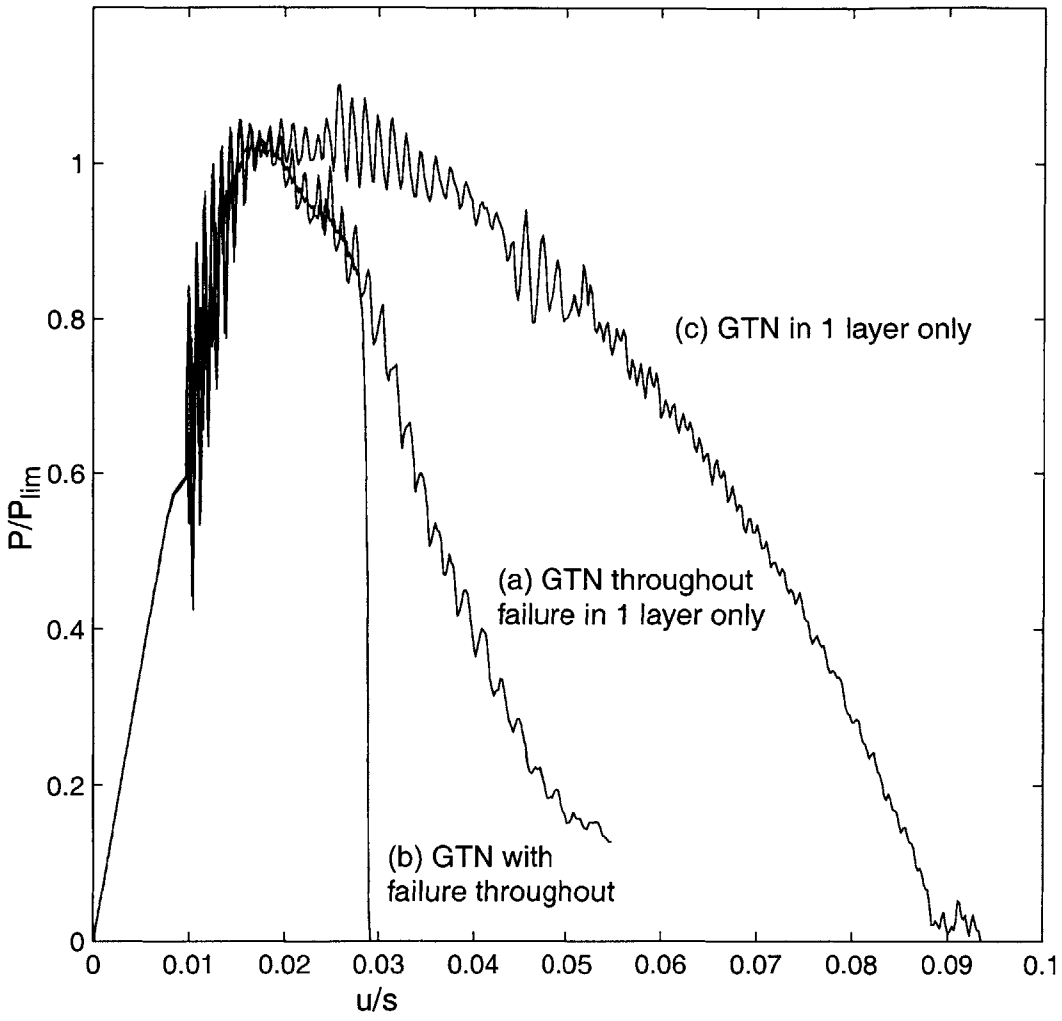

Figure 6-16: Back-bend normalized load-displacement curves for 2-D plane strain, non-hardening finite element runs; $l_0 = 6.0$ mm. (a) With the GTN model assigned throughout the mesh; single layer of interface elements next to the specimen mid-plane were allowed element deletion. (b) With the GTN model allowing element deletion throughout the mesh. (c) With the GTN model restricted to single layer of interface elements next to the specimen mid-plane.

Chapter 7

Conclusions

The back-bend specimen gives a low-triaxiality, plane strain test on the remaining fully-plastic tensile ligament, while requiring a fraction of the load of direct tension. It provides a novel way to model low-triaxiality cracking behavior as seen in a through-thickness penetration of a long surface-crack along a pressure vessel wall. The back-bend test also allows testing of bigger specimens with a given machine capacity, although drastically increasing the moment arm, s, would greatly increase specimen compliance, tending to cause post-peak system instability. The current back-bend test employed 4-point bending, and while 3-point bending would allow decreasing the loads further, the effect of the hydrostatic stress on the slot-face contact leads to a more complicated solution.

Back-bend specimens ($\sigma_n/2k = 0.5$) of A572 Gr.50 structural steel were tested in slow bending at room temperature, and compared to the more familiar high-triaxiality deeply-cracked open-bend test ($\sigma_n/2k = 1.543$), of identical geometry. The experimental load-displacement curves and topographs were analyzed using SLFM2 to obtain the $CTOD_i$ and $CTOA$ for crack initiation and growth. Finite element analyses were done in both plane strain and 3-D and the $CTOD_i$ and $CTOA$ determined.

The results, summarized in Table 5.1, show that $CTOD_i$ in back-bending as calculated from topography and finite element analysis is twice that of open-bending. The $CTOA$-values calculated from load-displacement curves, topographs and finite element analysis are initially $\sim 30°$ in back-bending but only half that in open-bending.

This large difference in $CTOA$ with triaxiality is consistent with results of Hancock, et al. [15]; however in their (much cleaner) steel, $CTOD_i$ was essentially constant over a range of specimens of differing triaxiality. The experimental fractographs showed a fair amount of tunneling in the back-bend specimens; a revised specimen with side grooves might be useful, to control tunneling and non-uniform growth.

The limit load for back-bending showed a good correlation with the experimental values, when calculated using the tensile strength, σ_{TS}; for open-bending the best match was obtained using a reduced flow-strength measure, $\sigma_{flow} = (\sigma_y + \sigma_{TS})/2$. The flow strengths calculated from limit load relations for back-bending and open-bending correlated well. SLFM2 provided an easy means to calculate the $CTOD_i$ from the load-displacement curves, but there is some uncertainty in the assumption that peak load is coincidental with initiation. "Initiation" is perhaps intrinsically problematic in the presence of pervasive occurrences of delaminations. In any event, perhaps insertion of a sequence of "small" unloading steps within an (otherwise) monotonic loading could provide unloading compliance data to sharpen estimates of u^p (and hence $CTOD_i$) at initiation.

Finite element analysis was done using special interface elements incorporating the GTN model along with element deletion. The GTN parameters and mesh size were chosen to match 3-D simulations with experimental results for the back-bend test. It was found that the GTN model limited to one layer of elements only, as was considered by Shih, et al. [21], did not provide the best correlation with experimental results. Therefore, the GTN model was used throughout the mesh, with element failure constrained to one layer only. The 3-D finite element load-displacement curves for the back-bend were in excellent agreement with the experimental results. While the 3-D finite element load-displacement curves for the open-bend agreed broadly with the experimental results, they did not match exactly, as the GTN parameters used were chosen for the low-triaxiality back-bend loading.

The back-bend finite element model was used to investigate issues of contained yielding during build-up of contact to fully-plastic levels. The results showed that the local fields evolve from high-triaxiality, contained yielding into low-triaxiality, fully-

plastic fields, with increasing applied load. This led to a study of size-scale effects in back-bend loading. The results showed higher-triaxiality fields in the larger specimen, as opposed to the low-triaxiality smaller specimen.

Appendix A

SLFM2 relations between far-field geometry and loading and $CTOD_i$ and $CTOA$

The relations between the far-field moments and displacements, and the crack-tip driving parameters θ_s, $\sigma_n/2k$ and u_s, and response functions $CTOD_i$ and $CTOA$ for the SLFM2 of 2.2, are given here for the back-bend and open-bend loadings of Figures 2-2(a) and (b).

A.1 Back-bend

The load-displacement curves of back-bend tests can be used to calculate the $CTOD_i$ and $CTOA$, assuming rigid-plastic, plane strain, non-hardening plasticity. For the geometry in Figure 2-1, the displacement across the slip line, u_s, the ratio of incremental micro-crack extension to the displacement increment across the slip line, $c_{,u}$, the incremental end-to-end half-rotation of the specimen, $d\theta^p$, and the incremental plastic specimen displacement, du^p, define

$$du_s = \sqrt{2}(t - 2l)d\theta^p; \tag{A.1}$$

$$du^p = sd\theta^p; \tag{A.2}$$

$$-dl = 2du_s \cos\theta_s + c_{,u} du_s. \tag{A.3}$$

The crack-tip opening displacement to begin crack growth, $CTOD_i$, can be written using Eqs. 2.2, A.1 and A.2 as

$$CTOD_i = 2(t - 2l_0)\frac{u^p_{(P_{max})}}{s}. \tag{A.4}$$

The bending moment, M, supported across the cracked section is

$$M = 2kBl(t - l), \tag{A.5}$$

By equilibrium M is also related to the system load, P, by $M = Ps/2$. Combining this relation and Eq. A.5 gives, in terms of the maximum moment M_{max} (assumed to occur at ligament l_0)

$$\frac{M}{M_{max}} = \frac{P}{P_{max}} = \frac{l(t-l)}{l_0(t-l_0)} = \frac{(l/t)(1-l/t)}{(l_0/t)(1-l_0/t)}. \tag{A.6}$$

In normalized form with $\lambda \equiv (l/t)$, $\lambda_0 \equiv (l_0/t)$, and $\mu \equiv M/M_{max} = P/P_{max}$,

$$\mu = \frac{\lambda(1-\lambda)}{\lambda_0(1-\lambda_0)}, \tag{A.7}$$

which gives

$$\lambda^2 - \lambda + \mu(\lambda_0 - \lambda_0^2) = 0. \tag{A.8}$$

Solving Eq. A.8, and for $\mu \leq 1$, using the minus sign to make $\lambda \leq \lambda_0$, gives

$$\lambda = \frac{1 - \sqrt{1 - 4\mu(\lambda_0 - \lambda_0^2)}}{2}. \tag{A.9}$$

Differentiating Eq. A.5 and dividing by M_{max} gives

$$\frac{dM}{M_{max}} = \frac{(t-2l)dl}{l_0(t-l_0)}. \tag{A.10}$$

Substituting Eqs. A.1, A.2, A.3 and using definitions of λ and λ_0, gives

$$\frac{dM}{M_{max}} = \frac{dP}{P_{max}} = -\left[\frac{1}{\lambda_0(1-\lambda_0)} - 4\mu\right](2\cos\theta_s + c_{,u})\sqrt{2}\,\frac{du^p}{s}. \tag{A.11}$$

Solving Eq. A.11 for $c_{,u}$ provides

$$c_{,u} = \left(\frac{-(dP/P_{max})\,/\,(du^p/s)}{\sqrt{2}\,(1/\left[\lambda_0(1-\lambda_0)\right] - 4\mu)}\right) - 2\cos\theta_s. \tag{A.12}$$

The back-bend $CTOA$ can be found from Eq. 2.4, with $c_{,u}$ evaluated from Eq. A.12 and $\theta_s = 45°$. dP/du^p is obtained from the post-peak slope dP/du of the load-displacement curve, corrected for specimen and machine compliance as follows. Differentiating Eq. 3.3 and dividing by dP gives:

$$\frac{du^p}{dP} = \frac{du}{dP} - (C_m + C_{spec}) - PC'_{spec}\frac{dc}{dP}. \tag{A.13}$$

The initial elastic portion of the load-displacement curve gives compliance as $(C_m + C_{spec}) = 0.025$ mm/kN. The crack compliance term is given as follows.

Crack compliance analysis

In Eq. A.13, the last term $PC'_{spec}(dc/dP)$ is determined as follows. Eq. A.6 for the load ratios,

$$\frac{P}{P_{max}} = \frac{l(t-l)}{l_0(t-l_0)} = \frac{(t-c)c}{(t-c_0)c_0}, \tag{A.14}$$

gives dc/dP as

$$\frac{dc}{dP} = \frac{1}{dP/dc} = \frac{(t-c_0)c_0}{P_{max}(t-2c)}. \tag{A.15}$$

Also, differentiating $PC_{spec} = u_{spec}$ gives,

$$PC'_{spec} = \frac{du_{spec}}{dc} \tag{A.16}$$

A finite element analysis can be used to obtain values of du_{spec}/dc under a constant load P_{const}, which would give values for C'_{spec} using Eq. A.16. This was done in ABAQUS/Standard using a multi-step elastic analysis of back-bending. The plane

strain finite element model of the half-specimen was loaded to $P_{const}/2 = 15$ kN, and nodes were released on the ligament, while keeping the load constant. The resulting plot of u_{spec} vs. c is shown in Figure A-1. From Eq. A.16, the slope of the plot gives $C'_{spec} = (du_{spec}/dc)/(P_{const}/2)$. Table A.1 lists the resulting values of the last term in Eq. A.13, $PC'_{spec}(dc/dP)$, at the three load levels evaluated in Figure 4-3. The numbers indicate that $PC'_{spec}(dc/dP)$ is an order of magnitude smaller than the other terms in Eq. A.13, (as seen in Table 4.2, $du/dP = -0.020$ mm/kN at $P/P_{max} = 0.57$, and $(C_m + C_{spec}) = 0.025$ mm/kN), and thus can be neglected.

Pre-straining analysis

For back-bending there is pre-straining in the ligament ahead of the crack growth. The pivot point is located at the last point of slot-face contact, a distance l_c away from the back face, as illustrated in Figure 2-2(a). The rotation rate of one-half of the specimen, $\dot{\theta}^p$, scales the velocities in the slip line field. Assuming non-hardening, which gives $l_c = l$ by equilibrium, velocity components on the rigid body side of the dominant slip lines in the crack growth direction x, and normal direction y, on one side of the symmetry plane, are

$$v_x = -\dot{\theta}^p y; \qquad v_y = \dot{\theta}^p \left(t - 2l + x\right). \tag{A.17}$$

In coordinates rotated by 45°, the velocity components, within the constant stress ligament, on the dominant slip lines in the slip line direction $\alpha = (x+y)/\sqrt{2}$, and in the normal direction $\beta = (y-x)/\sqrt{2}$, are

$$v_\alpha = \dot{\theta}^p \left[\beta - \frac{t-2l}{\sqrt{2}}\right]; \qquad v_\beta = \dot{\theta}^p \left[\alpha + \frac{t-2l}{\sqrt{2}}\right]. \tag{A.18}$$

The above relations give an expression for $\dot{\varepsilon}_{lig}$, the strain-rate ahead of the ligament, using the velocity at $y = 0$, as follows:

$$\dot{\varepsilon}_{xx} \equiv \dot{\varepsilon}_{lig} = \frac{dv_x(x, y=0)}{dx} \equiv -\dot{\theta}^p. \tag{A.19}$$

The equivalent plastic strain-rate follows as:

$$\dot{\varepsilon}^p_{eq} = \frac{2\dot{\theta}^p}{\sqrt{3}}. \tag{A.20}$$

A.2 Open-bend

The load-displacement curves of open-bend tests can also be used to calculate the $CTOD_i$ and $CTOA$, assuming a rigid-plastic, plane strain, non-hardening idealization. From the Green and Hundy slip line solution [14] for open-bend loading, the slip-line displacement, u_s, and the incremental end-to-end half-rotation, $d\theta^p$, are

$$du_s = l\left(\frac{R}{l}\right) d\theta^p; \tag{A.21}$$

$$d\theta^p = \frac{du^p}{s}. \tag{A.22}$$

Here $(R/l) = 0.388$, $\theta_s = 72°$, and from the SLFM2 response functions,

$$-dl = c_{,u} du_s; \qquad c_{,u} = \frac{-dl}{du_s}. \tag{A.23}$$

The crack-tip opening displacement to begin crack growth, $CTOD_i$, can be found from Eqs. 2.2, A.21 and A.22

$$CTOD_i = 2l_0\left(\frac{R}{l}\right)\frac{u^p_{(P_{max})}}{s}\sin\theta_s. \tag{A.24}$$

Combining Eqs. A.21, A.22 and A.23 provides

$$c_{,u} = \frac{-dl}{l\,(R/l)\,(du^p/s)}. \tag{A.25}$$

From the limit load as given by Eq. 4.3,

$$\frac{dl}{l} = \frac{dP}{2P}. \tag{A.26}$$

Substituting Eq. A.26 into A.25 gives

$$c_{,u} = \frac{-1}{2(R/l)} \frac{(dP/P)}{(du^p/s)}. \tag{A.27}$$

The open-bend $CTOA$ can be found from Eq. 2.4, with $c_{,u}$ evaluated from Eq. A.27, and $\theta_s = 72°$. In Eq. A.27, dP/du^p is obtained from the post-peak slope dP/du of the load-displacement curve, corrected for specimen and machine compliance using Eq. A.13. The initial elastic portion of the load-displacement curve gives $(C_m + C_{spec}) = 0.12$ mm/kN. The compliance due to cracking is given as follows.

Crack compliance

For a pure-bending specimen, the rotation due to crack, θ_c, at a given crack length c is given by [33] as

$$C_{spec}(c) = \frac{\theta_c(c)}{M} = \frac{24}{t^2 E' B} S(c/t). \tag{A.28}$$

Here

$$S(c/t) = \left(\frac{c/t}{1-c/t}\right)^2 \left\{5.93 - 19.69(c/t) + 37.14(c/t)^2 - 35.84(c/t)^3 + 13.12(c/t)^4\right\}. \tag{A.29}$$

Using Eqs. A.28 and A.15 for dc/dP, the last term in Eq. A.13, $PC'_{spec}(dc/dP)$, is an order of magnitude smaller than du/dP (as seen in Table 4.3, $du/dP = -3.43$ mm/kN at $P/P_{max} = 0.40$).

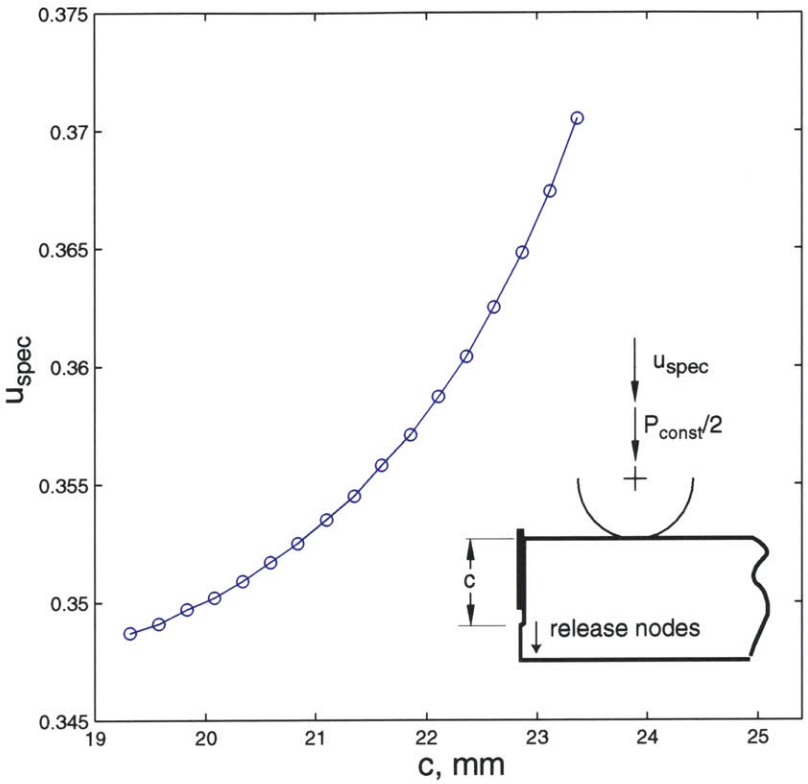

Figure A-1: Plot of u_{spec} vs. c as calculated from the elastic, plane strain analysis of back-bending, by releasing nodes in the ligament at a constant load level, P_{const}.

	$\mu = P/P_{max}$	$c(\mu)$ [2.6] (mm)	dc/dP [A.15] (mm/kN)	C'_{spec} $= (du_{spec}/dc)/(P_{const}/2)$ ((mm/kN)/mm)	$PC'_{spec}(dc/dP)$ [mm/kN]
Fig. 4-3(a)	0.82	21.3	-0.103	2.11×10^{-4}	-1.06×10^{-3}
Fig. 4-3(b)	0.57	22.7	-0.089	4.48×10^{-4}	-1.35×10^{-3}
Fig. 4-3(c)	0.42	23.5	-0.082	8.16×10^{-4}	-1.68×10^{-3}

Table A.1: Calculation of $PC'_{spec}(dc/dP)$, the last term in Eq. A.13, to obtain the $CTOA$ from experimental load-displacement results for back-bend tests. Numbers in brackets refer to equation numbers used in calculations. With $l_0 = 5.25$ mm, $c_0 = 20.15$ mm, and $P_{max} = 59.57$ kN.

Bibliography

[1] Ewing DJF. Calculations on the bending of rigid/plastic notched bars. Journal of the Mechanics and Physics of Solids 1968;16:205-213.

[2] Lee HY, Parks DM. Fully plastic analyses of plane-strain single-edge-cracked specimens subject to combined tension and bending. International Journal of Fracture. 1993;63(4):329-349.

[3] Bass MK. Fully-plastic open-bend and back-bend fracture specimens. SM Thesis, Massachusetts Institute of Technology, February 2000.

[4] Parks DM. Advances in characterization of elastic-plastic crack tip fields. Topics in Fracture and Fatigue (Ed. AS Argon, McClintock Festschrift) Springer-Verlag, 1992, pp.59-98.

[5] Hutchinson JW. Singular behavior at the end of a tensile crack in a hardening material. Journal of the Mechanics and Physics of Solids 1968;16:13-31.

[6] Rice JR, Rosengren GF. Plane strain deformation near a crack tip in a power law hardening material. Journal of the Mechanics and Physics of Solids 1968;16:1-12.

[7] Suresh S. Fatigue of Materials. Cambridge University Press, 40 West 20th St, New York, NY 1998.

[8] Dodds RH, Shih CF, Anderson TL. Continuum and Micromechanics Treatment of Constraint Fracture. International Journal of Fracture 1993;64:101-133.

[9] Sharma SM, Aravas N. Determination of higher-order terms in asymptotic elastoplastic crack tip solutions. Journal of the Mechanics and Physics of Solids 1991;39(8):1043-1072.

[10] Chao YJ, Zhu XK. $J - A_2$ characterization of crack-tip fields: extent of $J - A_2$ dominance and size requirements. International Journal of Fracture 1998;89(3):285-307.

[11] McClintock FA, Kim Y-J, Parks DM. A criterion for plane strain, fully plastic, quasi-steady crack growth. International Journal of Fracture 1995;72:197-221.

[12] McClintock FA. Slip line fracture mechanics: A new regime of fracture mechanics. Fatigue and Fracture Mechanics: 33rd Volume, ASTM STP 1417 (W.G. Reuter and R.S. Piascik, Eds.) ASTM, West Conshohocken, PA, 2002.

[13] McClintock FA. Plasticity Aspects of Fracture, Vol. 3, Fracture: An Advanced Treatise, H. Liebowitz, Ed., Academic Press, London, 1971. pp.47-225.

[14] Green AP, Hundy BB. The initial plastic yielding in notched bend test. Journal of the Mechanics and Physics of Solids 1956;4:128-144.

[15] Hancock JW, Reuter WG, Parks DM. Constraint and toughness parameterized by T. Constraint Effects in Fracture, ASTM STP 1171 (E.M. Hackett, K. H. Schwalbe, and R. H. Dodds, Eds.) ASTM, Philadelphia, PA, 1993 pp.21-40.

[16] Wilson AD. Effect of advanced steelmaking techniques on inclusions and mechanical properties of plate steels. Journal of Metals 1976;28(12):287-307.

[17] Gurson AL. Continuum theory of ductile rupture by void nucleation and growth-I. ASME Journal of Engineering Materials and Technology 1977;99:2-15.

[18] Tvergaard V. Influence of voids on shear band instabilities under plane strain condition. International Journal of Fracture Mechanics 1981;17:389-407.

[19] Tvergaard V. On localization in ductile materials containing voids. International Journal of Fracture Mechanics 1982;18:237-251.

[20] Needleman A, Tvergaard V. An analysis of ductile rupture in notched bars. Journal of the Mechanics and Physics of Solids 1984;32:461-490.

[21] Shih CF, Xia L, Hutchinson JW. A computational approach to ductile crack growth under large scale yielding conditions. Journal of the Mechanics and Physics of Solids 1995;43:389-413.

[22] Gullerud AS, Gao XS, Dodds RH, Haj-Ali R. Simulation of ductile crack growth using computational cells: numerical aspects. Engineering Fracture Mechanics 2000;66(1):65-92.

[23] Siegmund T, Brocks W. Prediction of the work of separation and implications to modeling. International Journal of Fracture 1999;99(1-2):97-116.

[24] ABAQUS, Version 5.8, Hibbitt, Karlsson & Sorensen Inc, Pawtucket, RI 02860, 1998.

[25] Pardoen T, Hutchinson JW. An extended model for void growth and coalescence. Journal of the Mechanics and Physics of Solids 2000;48:2467-2512.

[26] Gologanu M, Leblond JB, Perrin G, Devaux J. Recent extensions of Gurson's model for porous ductile metals. In: Suquet, P (Ed.) Continuum Micromechanics. Springer-Verlag, 1995, pp.61-130.

[27] McClintock FA. A criterion for ductile fracture by the growth of holes. Journal of Applied Mechanics 1968;(35):363-371.

[28] Rousselier G. Ductile fracture models and their potential in local approach of fracture. Nuclear Engineering and Design 1987;105(1):97-111.

[29] Ishikawa N, Parks DM, Kurihara M. Micromechanical modeling of ductile crack initiation behavior of two phase steels. ISIJ International 2001;41(1):76-85.

[30] Murakami Y. Stress intensity factors handbook. Pergamon Press, Oxford OX3 0BW, England 1987.

[31] Wu X-R, Carlsson AJ. Weight Functions and Stress Intensity Factor Solutions. Pergamon Press, Oxford OX3 0BW, England 1991.

[32] McClintock FA, Parks DM, Holmes JW, Bain KR. Drop in K_I due to load shift in Single-Edge-Notch tests with compliant drawbars. Engineering Fracture Mechanics 1984;20(1):159-167.

[33] Tada H, Paris PC, Irwin GR. The Stress Analysis of Cracks Handbook. The American Society of Mechanical Engineers, Three Park Avenue, New York, NY 2000.